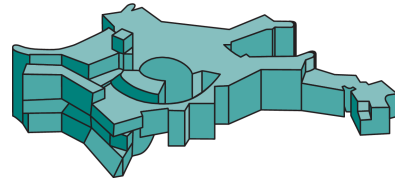Technische Universität München   Max-Planck-Institut für Astrophysik

Three-dimensional Models of Core-collapse Supernovae from Low-mass Progenitors

Georg Stockinger

Vollständiger Abdruck der von der Fakultät für Physik der Technischen Universität München zur Erlangung des akademischen Grades

Doktors der Naturwissenschaften (Dr. rer. nat.)

genehmigten Dissertation.

Vorsitzende/-r: Prof. Dr. Lothar Oberauer
Prüfer der Dissertation: 1.   apl. Prof. Dr. Hans-Thomas Janka
                            2.   Prof. Dr. Sherry Suyu

I would like to dedicate this Thesis to my friends who have had more impact on this thesis as they'd probably know ...

Acknowledgements

Abstract

We present full $4\pi-3D$, long-time simulations of core-collapse supernovae (CCSNe) resulting from low-mass progenitors, covering the evolution from bounce through shock revival until shock breakout. We consider two low-mass iron core progenitors of 9.6 $M_\odot$ and 9.0 $M_\odot$ with zero metallicity and solar metallicity, respectively, and one progenitor with an oxygen-neon-magnesium core, which explodes as an electron-capture supernova (ECSN). In the ECSN case, mixing of nickel is inefficient because of a relatively spherical beginning of the explosion, triggered by a steep density gradient outside of the degenerate core and the concomitant absence of secondary non-radial instabilities at composition-shell interfaces of the progenitor. The similarity between the core structure of the zero-metallicity progenitor and the ONeMg progenitor leads to similarities in their explosion properties. In both of these cases, we observe roughly equal amounts of nickel mixing in mass and velocity space and qualitatively similar ejecta morphology at late times, characterized by small deviations from spherical symmetry. In contrast, the solar-metallicity iron core progenitor explosion shows strong growth of Rayleigh-Taylor plumes in the entire helium core. The large initial asymmetries lead to more pronounced mixing. In this case the final morphology is remarkably similar to the remnant morphology seen in long-time simulations of massive progenitors. Interestingly, the shock deceleration in the extended hydrogen envelope of this model is so extreme that a fast nickel plume catches up with the shock and leads to shock deformation and an aspherical breakout of the shock at the stellar surface.

Contents

Chapter 1

Introduction

Supernova explosions are the great finale of the life of a massive star. The immense brightness of the explosion can outshine their host galaxy for a brief moment and, if close enough, can appear as "guest stars" in our night sky (Lundmark, 1921). Ever since Baade and Zwicky (1934) identified these events as the result of the collapse of the iron-core of a massive star, the exact mechanism that leads to such events is under investigation. They are not only the birthplaces of neutron stars and black holes but prove to be exclusive laboratories to probe extreme physics as it was firstly done with numerical simulations by Colgate and White (1966). Densities during the explosion reach nuclear saturation, magnetic fields may produce jet like explosions (Lopez et al., 2014; Halevi and Mösta, 2018) and neutrino interactions may strongly neutronize material, conditions necessary to produce neutron rich elements (Meyer et al., 1992; Arcones et al., 2007). Lightcurves and spectra are routinely used today to identify the yields and distributions of elements produced by these events. Not just since then have they been recognized as non-spherical events. A famous example represents Messier who mistook the Crab nebula as a comet (Messier, 1774).

1.1 Evolution to Collapse and Bounce

Stars are born from the collapse of gaseous hydrogen clouds. If gravity overcomes the pressure support by the gas, they collapse until central densities exceed the threshold for hydrogen burning (Kippenhahn et al., 2012), which marks the birth of the star. The pressure maintained by the energy released in the fusion of elements stabilizes the star against further contraction. As soon as most of the fuel is burnt to its ash at the center of the star, the star contracts until temperatures and densities are large enough to ignite

burning of the ash. This depletion of fuels and ignition of the ash repeats over the lifetime of the star, faster for more massive stars, giving the star its shell like structure. Dependent on the zero age main sequence (ZAMS) mass of the star, its metallicity (Z) and rotation, these shells are more or less extended in radius and mass and may exhibit strong density variations at their borders. In the case of blue supergiants (BSGs), for example, mass loss leads can lead to a significant reduction of the size of the hydrogen envelope. Stars with a ZAMS mass of around eight times the mass of our sun are called "massive stars".

In the case of massive stars in the ZAMS range considered in this thesis ($M \sim 8-10\,\mathrm{M_\odot}$), degeneracy effects, accompanied by temperature and composition inversions and off-center shell ignition (Woosley and Heger, 2015), complicate the evolution. Strongly dependent on these effects, the star eventually produces an iron-core at its center, evolves to a carbon-oxygen (CO) or oxygen-neon (ONe) white dwarfs or grows a highly degenerate oxygen-neon-magnesium (ONeMg) core. If the ZAMS mass of the star exceeds a certain threshold mass, the resulting core grows massive enough, to exceed the Chandrasekhar mass limit (Chandrasekhar, 1931). It thus becomes gravitationally unstable, with an effective adiabatic index $\gamma \leq 4/3$. Two processes trigger and accelerate the collapse of the cores.

Thermal energy is consumed by photo-dissociation of heavy nuclei into nucleons and α-particles, due to the increasing temperature. Also electron captures on heavy nuclei become more frequent as densities increase, carrying away energy and leptons by the emission of neutrinos, further reducing the pressure support by electron degeneracy. In the case of ONeMg cores, electron captures on ^{24}Mg via the reactions ^{24}Mg$(e^-, \nu_e)^{24}$Na and ^{24}Na$(e^-, \nu_e)^{24}$Ne destabilize the core (hence the name electron-capture supernova ECSN). Continuous e^--capture on ^{20}Ne further reduces the electron pressure but the resulting γ energy deposition through the decay of ^{20}O is enough to enable oxygen burning via the reaction ^{16}O $+$ ^{16}O (Miyaji et al., 1980; Nomoto, 1984).

Energy support by oxygen burning could, in certain cases, invert the collapse and produce a thermonuclear runaway (Jones et al., 2016). This depends sensitively on the central densities that are reached before the collapse and on certain nuclear transition rates (Kirsebom et al., 2019). Should the collapse proceed, however, its dynamics are independent from the nuclei involved. The inner core collapses adiabatically and homogenously, while the outer core falls in with supersonic velocities. When densities increase above $10^{12}\,\mathrm{g/cm^3}$, neutrinos become trapped as their diffusion timescale exceeds the free fall time scale. A sudden halt of the collapse is caused by nuclear forces repelling further compression at $\sim 2.7 \times 10^{14}\,\mathrm{g/cm^3}$. The core "bounces" and sends a shock wave against the infalling matter. As this shock wave rushes through the infalling matter, it loses energy by the

dissociation of heavy nuclei into nucleons summing up to about $8.8\,\mathrm{MeV}$ per nucleon (assuming the binding energy of $^{56}\mathrm{Fe}$) . Because of this, the shock stalls, turning into an standing accretion shock, while behind the shock the accreted matter settles on the newly born proto-neutron star (PNS) at the center.

1.2 Explosion of Massive Stars

In order to resuscitate the stalled shock, enough energy has to be deposited in the region between the PNS and the shock wave (also called forward shock). Based on the ideas of Colgate and White (1966), Bethe and Wilson (1985) proposed that the interaction of neutrinos with the high density matter provides enough energy to enable explosions. When the core collapses from $1000\,\mathrm{km}$ to several tens of kilometers, $\sim 10^{53}\,\mathrm{erg}$ of energy are converted into internal energy, an energy reservoir large enough to power the explosion. The PNS can only cool by emitting neutrinos. They diffuse outwards to their respective neutrino-sphere, where they begin to stream freely. Some of their energy is absorbed in the layers above the PNS mainly by charged-current reactions

$$\nu_\mathrm{e} + \mathrm{n} \to \mathrm{e}^- + \mathrm{p}, \tag{1.1}$$

$$\bar{\nu}_\mathrm{e} + \mathrm{p} \to \mathrm{e}^+ + \mathrm{n}. \tag{1.2}$$

Since the absorption, and thus energy gain of matter, and emission, and thus cooling of matter, follows a r^{-2} and a steep r^{-6} dependence, respectively (Burrows, 2013; Janka, 2012), there is a radius of equal heating and cooling. This radius, coined the "gain-radius", separates the lower cooling layer from the outer gain layer. If enough energy can be deposited in the gain layer, the shock can be revived.

Despite the arguments presented above, modern spherically symmetric simulations of the "delayed neutrino-heating" mechanism, including state-of-the-art neutrino physics, do not show explosions for solar metallicity[1] progenitors with ZAMS masses $M \geq 9\,\mathrm{M}_\odot$. One-dimensional (1D) simulations disregard the possibility of simultaneous accretion and expulsion of matter. Neutrino heating in the gain layer, however, creates a negative entropy gradient which should lead to convective motions. This issue has been tackled by the first axis-symmetric simulations in the late 80's and early 90's, see e.g. Herant et al. 1994; Burrows and Hayes 1995; Janka and Müller 1996. These studies showed that the gain layer is a region of violent convection, where fast, cold downdrafts can hit the neutron star

---

[1]The metallicity of a star relative to solar is defined as $[\mathrm{Fe/H}] = \log((X_\mathrm{Fe}/X_\mathrm{H})/(X_\mathrm{Fe}/X_\mathrm{H})_\odot)$, where X_i is the mass fraction of the species i.

surface and high entropy material rises in plumes. These plumes push the shock radius to larger radii producing (highly) asymmetric explosions, while the downflows provide fresh material into the gain region. The downflows increase the total heated mass and thereby the explosion energy. Although the chosen geometry and symmetry constraints have their downsides, these simulations pointed towards the need of multi-dimensional models.

As computationally resources grew over the last decades the pool of axis-symmetric, two dimensional (2D) models grew (see e.g. Kifonidis et al. 2003; Scheck et al. 2006, 2008; Fryer and Heger 2000; Radice et al. 2017). They focused on the explosion mechanism, hydrodynamical instabilities in the gain-layer and of the stalled shock, neutron star kicks and on nucleosynthesis in the neutrino heated matter. In the last decade the first fully three-dimensional (3D) simulations were conducted (see e.g. Hammer et al. 2010; Takiwaki et al. 2012; Tamborra et al. 2014; Melson et al. 2015a; Melson et al. 2015b; Summa et al. 2016; Müller et al. 2017; Müller et al. 2018; Vartanyan et al. 2018; Mösta et al. 2018; Glas et al. 2019 ; Burrows et al. 2019 and Melson et al. 2019 as a small excerpt of current research). Although there is a considerable spread in the "explodability" of the chosen progenitors among different groups, and thus different simulation techniques, the qualitative picture of violent motions in the gain layer and sloshing and oscillations of the shockwave that result in asymmetric distribution of elements, holds. These asymmetries are necessary in order to explain the observed natal kicks of neutron stars that can reach up to $v_{\text{NS}} \approx 1000$ km/s (Chatterjee et al., 2005). The fast metal rich clumps of ejecta in CasA or SN1987A are however hard to explain without connecting the first seconds after bounce with the time the shock leaves the progenitors star and exposes its interiors to observations.

1.3   Evolution After Shock-Revival

After the shock has been revived, it begins to expand through the stellar envelope. The expansion of the shock wave proceeds basically self-similar where the velocity of the shock depends on the gradient of the background density. Assuming a spherical shock wave, Sedov et al. (1961) found that the velocity of the shock increases/decreases if the density stratification is steeper/flatter than $\rho \sim r^{-3}$. Typically, stellar envelopes of RSGs have a density profile of $\rho \sim r^{-(2...4)}$ (Matzner and McKee, 1999) where different composition shells have different density profiles. Consequently, the supernova shock undergoes phases of deceleration and acceleration as it expands to the stellar surface. As it has been noted already by Chevalier and Klein (1978), the pressure waves which are sent back into the postshock matter during phases of deceleration create regions which are unstable to

hydrodynamic instabilities. Density and pressure gradients attain opposing signs behind the forward shock. Under these conditions, perturbations of the density may grow by the Rayleigh-Taylor (RT) instability (RT) (Rayleigh, 1882). Additionally, if layers of different densities are overrun by a deformed shock wave, the growth of the Richtmyer-Meshkov (RM) instability adds to the overall mixing during the explosion. These instabilities can potentially explain the observed structure of supernova remnants, whose morphology is far from the onion-like structure resulting from one-dimensional simulations. Another consequence of the varying shock velocity is the pile-up of matter behind the shock into a high-density shell which acts as a "wall" (Kifonidis et al., 2003) for the inner ejecta. Note that this matter travels at supersonic velocities, therefore information can only be mediated downstream via a non-linear wave (Kifonidis et al., 2003). Hence, a reverse shock forms at the bottom of this dense shell which later falls back onto the PNS, decelerating the inner material.

The first long-time studies in 2D were conducted by e.g. Müller et al. (1991) and Herant and Woosley (1994). These early simulations, started from spherically symmetric models at 300 seconds after the core bounce, already showed that mixing in the stellar envelope due to the RT instability can yield fast ^{56}Ni clumps in the ejecta, which are needed to explain the clumpiness and mixing found in photospheric emission (Utrobin et al., 2015, 2017) and spectral analyses of the nebular phase pf core-collapse events (Jerkstrand, 2017) as for example in SN1987A. (Kifonidis et al., 2003) performed high-resolution simulations in axis-symmetry from core bounce until shock breakout, showing that simulations covering the full evolution of the explosion are necessary to explain high ^{56}Ni velocities in SN1987A.

The first 3D long-time simulations from 3D initial data were conducted by Hammer et al. (2010), noting that mixing by the RT instability in 3D is more efficient than in 2D simulations due to the increased drag force a body experiences in the axis-symmetric case. Thus, in order to fully understand the mixing processes after the the onset of the explosion, 3D simulations are necessary. This task was undertaken by Wongwathanarat et al. (2015), who performed long-time simulations of explosions of progenitors for SN1987 with initial ZAMS masses from 15 - 20 M$_\odot$.

They showed that the final ejecta distribution carries imprints of the asphericities produced during the onset of the explosion ($t \sim 1\,\mathrm{s}$), which are further modified during later phases. Depending on the detailed progenitor structure, hydrodynamic instabilities arising at the composition interfaces, such as the RT and the RM instabilities, shapes the final spatial and velocity distribution of nucleosynthetic products. The resulting ejecta morphology exhibits inhomogenously mixed ejecta and strongly pronounced RT-fingers resembling also the geometry found in Cas A (Wongwathanarat et al., 2017; Grefenstette

et al., 2017) or observations of SN1987A (Utrobin et al., 2019). Due to the highly complex and stochastic behaviour of nonradial instabilities and turbulence during the onset of the explosion phase and the nonlinear evolution of the RT instability, a clear connection between the asymmetries, and thus the degree of mixing, and the progenitor structure has still to be worked out.

Motivated by the recent detection of NS-NS mergers by Ligo/VIRGO (GW170817, Abbott et al. 2017) Müller et al. (2018) investigated the long-time evolution of ultra-stripped progenitors. These progenitors, also called helium stars, evolve in a close binary system of massive stars in which one of the companions undergoes a SN and forms a neutron star. In the following evolution the secondary becomes an almost naked metal star due to mass transfer via the so-called Case BB Roche-lobe overflow to the neutron star, leaving only some $\lesssim 0.1\,\mathrm{M}_\odot$ of the hydrogen.

1.4 Aims of This Work

Despite the progress made by various three-dimensional studies of the evolution of the shock wave through the stellar envelope, they focused mainly on on progenitors in the range of $M_{\mathrm{ZAMS}} = 15 - 20\,\mathrm{M}_\odot$. Also the explosion itself is not triggered self-consistently, but with parametrized neutrino-transport or pistons several hundred seconds after the collapse. This is critical in certain ways. Around 20% of CCSNe originate from progenitors with initial masses of less than 12 solar masses assuming a standard Salpeter initial mass function (IMF) (Salpeter, 1955) with an upper limit for CCSNe of $20\,\mathrm{M}_\odot$. Their very complex evolution yields vastly different pre-collapse states in a narrow band of ZAMS masses. These low-mass progenitors, some of which end their life as ECSNe, have not been investigated by multi-dimensional long-time simulations before, although one of the most famous supernovae, SN1054 or "Crab", is thought to originate from a low-mass progenitor (Smith, 2013; Nomoto et al., 2014). Further, purely parametrized simulations lack the detailed neutrino-transport scheme of more advanced simulation setups. This may influence the time of the onset of explosion and thus the time available for convection to grow. In the piston driven explosions the growth of convection during the onset of the explosion is completely ignored.

In this Thesis we use, for the first time, multi-dimensional simulations beginning from collapse to shock breakout for three different low-mass progenitors. Two of these form an iron core at their center and one forms a degenerate ONeMg core. The iron-core models (z9.6 and s9.0) were simulated self-consistently by Melson et al. (2015a); Melson (2016) until the onset of explosion. The data of this simulation provides the initial condition for

our long-time simulation. The ONeMg-core progenitor is investigated here for the first time, covering the collapse, onset of the explosion and long-time evolution. We thus tackle the mentioned issues by aiming to answer the following questions

- What are the differences in the initiation of the explosion of low-mass Fe-core end ONeMg-core progenitors?

- What is the influence of each progenitor structure on the long-time evolution of the explosion? In particular, what is the influence on the formation of reverse shocks and the efficiency of mixing of neutrino-heated material?

- Are low-mass progenitors of CCSNe able to produce highly mixed ejecta in a similar fashion as their more massive counterparts as found in previous studies?

- How do the properties of the compact remnant change on long time-scales due to fallback of matter? Are there significant changes to the remnant's mass, kick or angular momentum?

In the following we will introduce the progenitors (Chapter 2) used for this study and describe the numerical methods and codes (Chapter 3). We will then investigate the post-bounce evolution of the progenitors until the forward shock is revived by neutrino heating (Chapter 4) which covers around one second of evolution. Finally, we investigate the propagation of the supernova shockwave through the stellar envelope and beyond and compare between the different progenitors in Chapter 5 before summarizing the results in Chapter 6.

Chapter 2

Progenitors

For this thesis we study an ECSN of a non-rotating 8.8 M$_\odot$ progenitor (e8.8) (Nomoto, 2017, private communication) and two non-rotating CCSNe resulting from low-mass iron core progenitors (z9.6, s9.0), provided by A. Heger (2015, private communication) (Woosley and Heger, 2015) and Sukhbold et al. (2016), respectively. The considered ECSN progenitor is explored here for the first time whereas the explosion of iron core progenitors was simulated in 3D with the VERTEX-PROMETHEUS code and are published in Melson et al. (2015b) and Melson et al. (2019).

2.1   ONeMg-core Progenitor

Model e8.8 is a solar-metallicity progenitor with a ZAMS mass of $M_{\mathrm{ZAMS}} = 8.8\,\mathrm{M_\odot}$ and was provided by Nomoto (2017, private communication). This progenitor has an ONeMg core that explodes as an ECSN. It has the typical very sharp density gradient outside of its $1.33\,\mathrm{M_\odot}$ ONeMg core ($\xi_{2.5} = 5.7 \times 10^{-6}$, $\xi_{1.5} = 8.0 \times 10^{-6}$) [1] which can be seen from the density (ρ) profile in Figure 2.2, where we also show the ρr^3-profiles, besides the electron fraction Y_{e} and temperature T as functions of enclosed mass and radius. The dash-dotted, dashed and dotted lines indicate the positions of the degenerate core/CO, CO/He and He/H composition interfaces, respectively. We define the locations of the composition interfaces, similar to Wongwathanarat et al. (2015), as those positions at the bottom of the respective layers of the star where the mass fractions X_{i} drop below half of their maximum values in the layer. The radial positions of the composition interfaces are summarized in Table 2.1. In the top panel of Figure 2.1 we present the composition of model e8.8,

---

[1]Because of its relevance for higher-mass progenitors we provide the compactness parameter (O'Connor and Ott, 2011) $\xi_M \equiv \frac{M/\mathrm{M_\odot}}{R(M_{\mathrm{bary}}=M)/10^3\,\mathrm{km}}$. Due to the steep density gradient outside of the core of the considered progenitors, its relevance in the present context is, however, questionable.

Table 2.1 Shell structure of the pre-collapse progenitor models.

Model	Interface	R_{shell} [cm]	M_{shell} [M$_\odot$]	$t^{\mathrm{3D}}_{\mathrm{sh,max}}$ [s]	E_{bind} [10^{49} erg]
e8.8	IG/ONeMg	2.57×10^7	0.45	-	
	ONeMg/C	8.48×10^7	1.33	0.19	$E_{\mathrm{bind}}(m > M_{\mathrm{map}}) = -5.99$
	C/He	1.09×10^8	1.34	0.20	
	He/H	1.21×10^8	1.34	0.21	
	Surface	8.43×10^{13}	5.83	4.1×10^5	
z9.6	IG/Si	1.10×10^8	1.30	0.09	
	Si/CO	1.45×10^8	1.36	0.11	$E_{\mathrm{bind}}(m > M_{\mathrm{map}}) = -5.82$
	CO/He	6.73×10^8	1.37	0.40	
	He/H	1.40×10^{12}	1.70	1.8×10^3	
	Surface	1.50×10^{13}	9.60	1.1×10^5	
s9.0	IG/Si	1.24×10^8	1.30	0.08	
	Si/CO	1.55×10^8	1.33	0.30	$E_{\mathrm{bind}}(m > M_{\mathrm{map}}) = -2.63$
	CO/He	1.34×10^9	1.40	1.30	
	He/H	1.22×10^{11}	1.57	124.0	
	Surface	2.86×10^{13}	8.75	1.8×10^5	

Notes: The radii of the composition interfaces, R$_{\mathrm{shell}}$, are defined as those positions at the bottom of the stellar layers (e.g. CO) where the mass fractions (e.g. C+O) drop below half of their maximum values in the respective layer first. We also show the mass M$_{\mathrm{shell}}$ contained within the corresponding radius and the post-bounce time when the outermost radius of the forward shock of our 3D models reaches the interface. E_{bind} is the binding (i.e. internal + kinetic + potential) energy outside of M_{map} which is the location of the final mass cut. For values see Table 4.2.

where we combine all elements with mass numbers greater than 28 into "iron-group" (IG) material or nuclei in nuclear statistical equilibrium (NSE). The ONeMg-core is surrounded by very thin carbon and helium shells ($M_{\mathrm{C}} \approx 8.1 \times 10^{-3}\,\mathrm{M_\odot}$, $M_{\mathrm{He}} \sim 2.1 \times 10^{-6}\,\mathrm{M_\odot}$) and a hydrogen (H+He) envelope ($M_{\mathrm{H}} \approx 4.49\,\mathrm{M_\odot}$).

A previous version of the progenitor (Nomoto, 1984, 1987, 2008), commonly termed e8.8 in the literature and e8.8$_{\mathrm{n}}$ in this publication, has been used in various studies, including nucleosynthesis (Wanajo et al., 2018) and PNS kicks (Gessner and Janka, 2018) and is a reference case for supernova simulations of ECSNe. The previously used progenitor e8.8$_{\mathrm{n}}$ has a more massive helium core with a mass of $\sim 1.375\,\mathrm{M_\odot}$, but a smaller hydrogen envelope (see Figure 2.2). The collapse and post-bounce evolution of the new progenitor are computed with Prometheus-HOTB as detailed in Section 3.2.3. We use Prometheus-HOTB for the simulation of model e8.8 for several reasons. Its pre-collapse structure

demands a very high resolution which, in 3D, is not feasible including a sophisticated neutrino-transport. Further, asymmetries in this model will grow in a similar fashion when using a parametrized in comparison to the full neutrino-transport approach due to the early onset of the explosion. It also enables us to account for uncertainties that still exist in the high-density regime of the PNS.
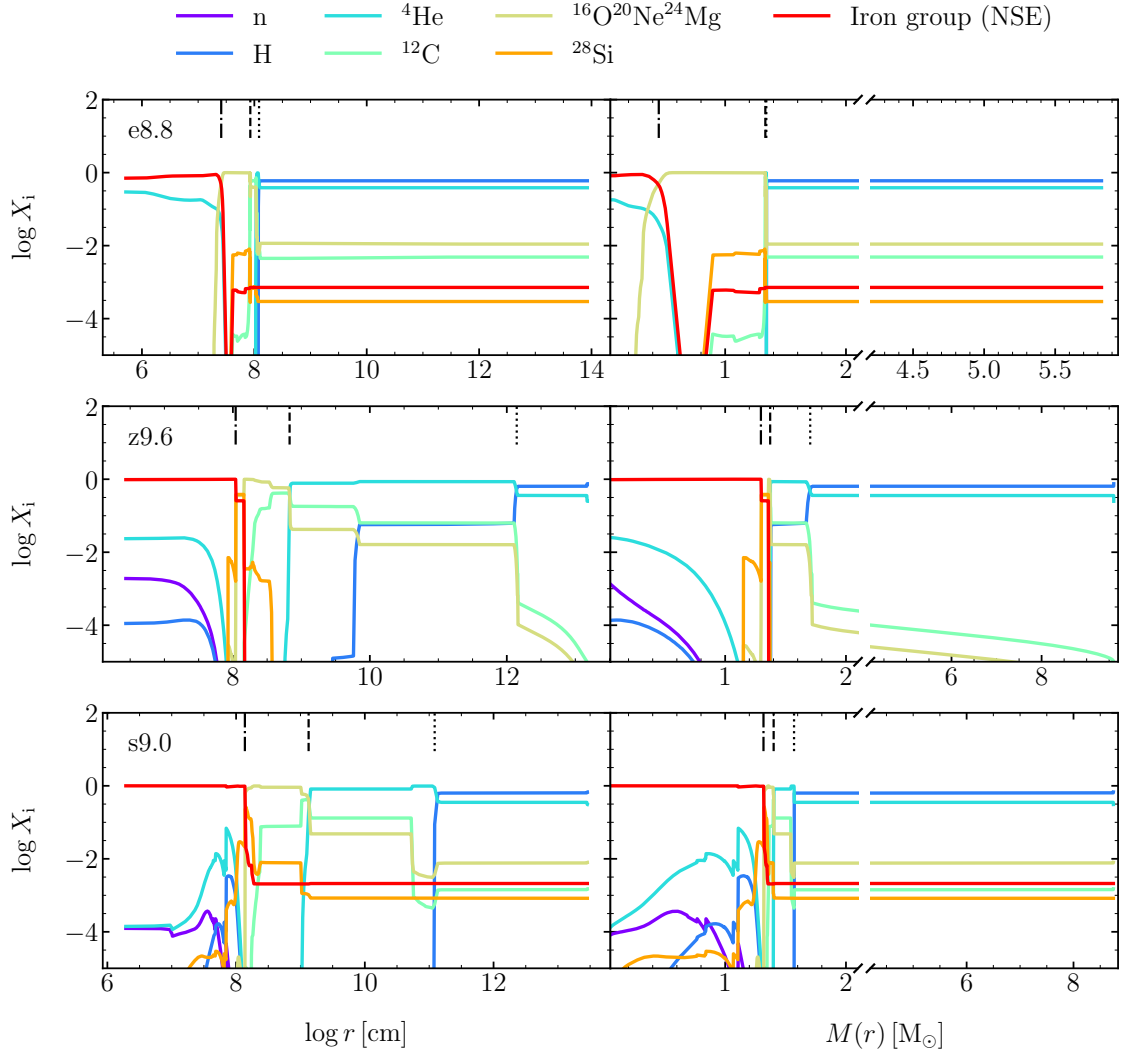
Fig. 2.1 Initial pre-collapse composition of models e8.8 (top), z9.6 (middle) and s9.0 (bottom) as a function of radius (left) and enclosed mass (right). We combine all elements with mass numbers greater than 28 into the "iron-group" (IG). The dash-dotted, dashed and dotted lines indicate the the outer boundaries of degenerate (iron or NSE), CO and He cores, respectively. The total masses of the shown elements are provided in Table 2.2

Table 2.2 Total masses of elements M_i of the pre-collapse progenitor models as shown in Figure 2.1

Species	$M_X\,[M_\odot]$		
	e8.8	z9.6	s9.0
H	2.68	5.10	5.10
^{4}He	1.78	3.11	2.68
^{12}C	2.71×10^{-2}	2.24×10^{-2}	3.35×10^{-2}
^{16}O^{20}Ne^{24}Mg	0.93	0.04	0.13
^{28}Si	3.98×10^{-3}	2.39×10^{-2}	1.30×10^{-2}
Iron-group	0.39	1.32	1.35

2.2 Fe-core Progenitors

As a second progenitor we employ a zero-metallicity $M_{\mathrm{ZAMS}} = 9.6\,M_\odot$ star, termed z9.6. It was first used by Janka et al. (2012) and is also considered in other studies such as Müller et al. (2013, 2018). This iron core progenitor is structurally similar to the ONeMg-core progenitor. It also shows a sharp decline of the density at the edge of its iron core enabling low-energy explosions in 1D (Melson et al., 2015a). Evolved as an extension to Heger and Woosley (2010), the pre-SN model develops an iron core of about 1.30 $M_\odot$. The iron core is surrounded by a $0.061\,M_\odot$ Si-layer, a $0.016\,M_\odot$ layer and has a helium layer of about 0.33 $M_\odot$ below a massive hydrogen envelope of ~ 8 $M_\odot$ ($\xi_{2.5} = 7.65 \times 10^{-5}$, $\xi_{1.5} = 2.37 \times 10^{-4}$). As the envelope is not enriched by metals, mass loss played only a negligible role during the star's evolution. This leaves the total mass of the star almost unchanged (see Table 2.1). Due to its structure it was one of the first iron core progenitors that exploded in fully self-consistent 3D simulations by Melson et al. (2015b) with Vertex-Prometheus. This result provides the initial state for our investigation

Moreover, we investigate a solar-metallicity $M_{\mathrm{ZAMS}} = 9.0\,M_\odot$ star, termed s9.0, of Sukhbold et al. (2016). Its 1.30 $M_\odot$ iron core is surrounded by a silicon shell of 0.03 $M_\odot$, a carbon-oxygen layer of 0.068 $M_\odot$ and a helium shell of 0.169 $M_\odot$ (see Table 2.1). The hydrogen envelope extends from 1.57 $M_\odot$ up to 8.75 $M_\odot$ ($\xi_{2.5} = 3.83 \times 10^{-5}$, $\xi_{1.5} = 5.25 \times 10^{-3}$). This progenitor was chosen to be representative for low-mass CCSNe by Jerkstrand et al. (2018), who focused on the late-time nebular spectra of the supernova, and by Glas et al. (2019) focusing on the neutrino emission during the explosion. The three-dimensional exploding model for our investigation is provided by Melson et al. (2019) and has also been modeled with Vertex-Prometheus.

Although the progenitors considered in this study have very similar ZAMS masses, their pre-collapse core structures differ strongly (see Figure 2.2). We stress the importance

of the ρr^3-profiles of the progenitors as they are decisive for the overall evolution of the explosion (Kifonidis et al., 2003; Wongwathanarat et al., 2015). The behavior of the ρr^3-profile yields important information of the propagation of the shock through the stellar structure because, according to Sedov et al. (1961), positive gradients of ρr^3 cause shock deceleration, whereas negative gradients cause the opposite. Additionally, variations of the shock velocity produce crossing pressure and density gradients behind the shock front near the composition-shell interfaces. Such conditions are essential for Rayleigh-Taylor instabilities as detailed in Section 5.2, assigning them a crucial role for explaining the high-velocity metal-rich ejecta and the radial mixing of heavy elements (Wongwathanarat et al., 2015).

The ONeMg-core progenitor exhibits an extremely sharp drop of the ρr^3-profile just outside the ONeMg core. It is this drop in density that enables fast explosions due to the according early rapid drop in mass accretion rate (Kitaura et al., 2006). Outside the core, the profile grows monotonically, as no more composition interfaces are encountered. The z9.6 progenitor also falls into the class of ECSN-like progenitors. Further, and similar to the electron capture model, the z9.6 shows a monotonic ρr^3 outside the CO core where only a small variation of the density can be seen at the He/H interface. The s9.0 model on the other hand shows strong variations in its ρr^3-profile. Shells with different compositions are clearly separated by a negative ρr^3-gradient just before the respective interface. Of particular interest are the CO/He and He/H interfaces. These will have an impact on the long-time evolution of the explosion as will be discussed in Section 5.2.

For this work we performed spherical-symmetric, axis-symmetric and fully three-dimensional simulations for the e8.8 model beginning from collapse of the core until shock-breakout (see Chapter 4 and Chapter 5, respectively). The long-time simulations of the iron core progenitors (z9.6 and s9.0) are started from initial data of full 3D-4π simulations computed with VERTEX-PROMETHEUS. In the following Chapter we will describe the numerical codes used for these simulations.
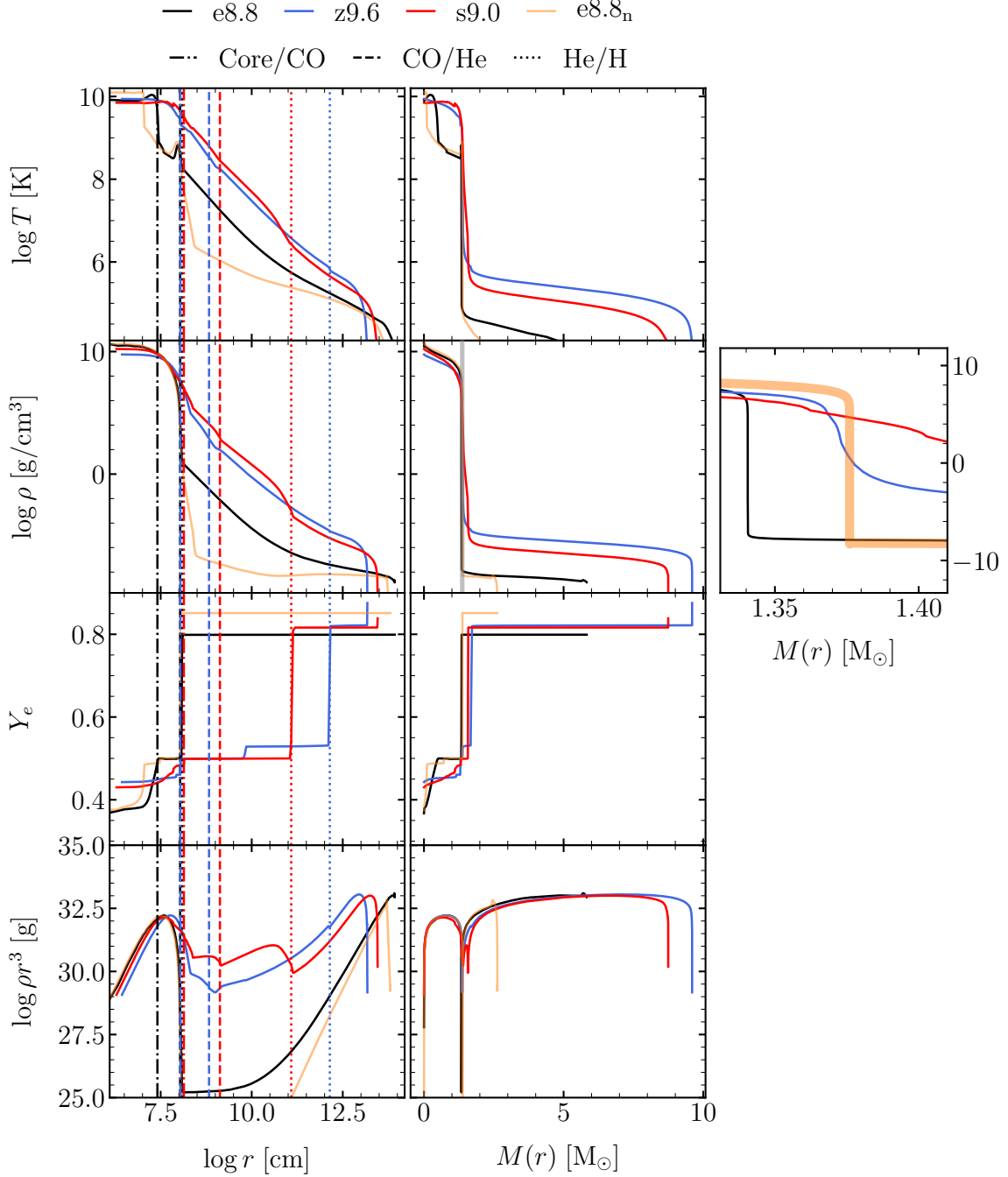
Fig. 2.2 Profiles of the temperature, density, electron fraction ($Y_{\rm e}$) and ρr^3 for the progenitor models as functions of radial coordinate (left panels) and mass coordinate (right panels). Indicated by dash-dotted, dashed and dotted lines are the outer boundaries of the degenerate (iron or NSE), CO and He cores, respectively. Note the huge differences in the density and ρr^3-profiles between the progenitors with iron and ONeMg cores in particular just outside the CO core. We show the difference in the core structure of our ONeMg core models as a zoom in the ρ vs $M(r)$ profiles in the rightmost panel.

Chapter 3

Numerical Methods

The results presented in this Thesis were obtained by using two different numerical codes, namely VERTEX-PROMETHEUS and PROMETHEUS-HOTB. As the names suggest, the hydrodynamic equations are solved with the Prometheus-Hydro module. Both numerical codes use an overlapping spherical grid in 3D simulations. The hydro module is then combined with different numerical treatments of the neutrino transport and nuclear-burning networks. VERTEX-PROMETHEUS uses a sophisticated energy-dependent neutrino-transport module (VERTEX). It is built for fully self-consistent simulations including the latest neutrino interactions. PROMETHEUS-HOTB uses a gray neutrino-transport scheme and excludes the innermost region of the neutron star from the computational domain. It relies on a one-zone model for the interior of the neutron star, a parametric "engine" to drive the explosion, making it computationally very efficient. Uncertainties in the equation of state of hot neutron stars and in the neutrino interactions at high densities are thus compiled into this engine. It is tuned by prescribing the contraction of the innermost zone and the neutrino fluxes at its boundary. Calibration of the parameters is done with the aid of self-consistent supernova simulations and the constraints from observations of CCSNe. The onset of the explosion of the iron-core progenitors were simulated with VERTEX-PROMETHEUS by Melson et al. (2015a) and Melson et al. (2019), whereas for the ECSN progenitor we use PROMETHEUS-HOTB. The long-time simulations are computed solely with PROMETHEUS-HOTB since it is better suited to follow the supernova shockwave to very large radii. In the following we will firstly describe the common treatment of hydrodynamics and gravity in both codes before describing the numerical and physical setup used in PROMETHEUS-HOTB in more detail. A short description of the VERTEX-PROMETHEUS code is given thereafter.

3.1 Hydrodynamics Module PROMETHEUS

The hydrodynamics solver PROMETHEUS acts as the backbone of the simulations with VERTEX-PROMETHEUS and PROMETHEUS-HOTB. Under the assumption that viscosity, temperature diffusion and other terms do not contribute on the timescales in which the supernova takes place, the character of the flow is described by the Euler equations. These formulate a coupled system of partial-differential equations (PDEs) of conservation laws, namely:

- Mass conservation

$$\frac{\partial \rho}{\partial t} + \nabla(\rho \mathbf{v}) = 0. \tag{3.1}$$

- Momentum Conservation

$$\frac{\partial \rho \mathbf{v}}{\partial t} + \nabla(\rho \mathbf{v}\mathbf{v}) = -\nabla P + \rho \boldsymbol{f}_{\mathrm{g}} \tag{3.2}$$

- Energy conservation

$$\frac{\partial \rho e_{\mathrm{tot}}}{\partial t} + \nabla(\rho e_{\mathrm{tot}} \mathbf{v}) = -\nabla P \mathbf{v} + \rho \mathbf{v} \boldsymbol{f}_{\mathrm{g}} + \rho Q_\nu + \rho Q_{\mathrm{nuc}} \tag{3.3}$$

Here $e_{\mathrm{tot}} = e_{\mathrm{int}} + 0.5|\mathbf{v}|^2$ is the total (kinetic plus thermal) specific energy density, ρ is the density, t the time, P the pressure, $\mathbf{v}$ the vector valued velocity, $\boldsymbol{f}_{\mathrm{g}}$ is the term accounting for gravity and Q_ν and Q_{nuc} are source terms accounting for the energy release or consumption due to neutrinos and nuclear reactions. In order to solve these equations PROMETHEUS, uses the exact Riemann-solver of Colella and Glaz (1985), where no shocks are present. Since higher order methods fail to accurately capture the propagation of shock waves, the HLLE solver by Einfeldt (1988) is used in the vicinity of shocks. Time integration is performed explicitly after solving the above equations in directional sweeps.

To include the effects of nuclear reactions and neutrino interactions, the source terms Q_ν and Q_{nuc}, as well as $\boldsymbol{f}_{\mathrm{g}}$ are applied in an operator split fashion (Strang, 1968).

3.1.1 Numerical Grid

For three-dimensional (3D) simulations PROMETHEUS-HOTB use the axis-free "Yin-Yang grid" based on the work of Kageyama and Sato (2004). VERTEX-PROMETHEUS uses the implementation of the grid as presented in Melson et al. (2015a), whereas the grid used in PROMETHEUS-HOTB follows the implementation by Wongwathanarat et al. (2010). Spherical polar three-dimensional grids suffer from numerical artifacts at the grid boundaries

in the θ- and ϕ- directions. The idea of the Yin-Yang grid is to split the grid into two overlapping subsets of the original spherical one. Locally (per grid patch) the angular coordinates are identical, completely independent and cover a range

$$\theta \in \left[\frac{\pi}{4}, \frac{3\pi}{4} \right] \tag{3.4}$$

$$\phi \in \left[-\frac{3\pi}{4}, \frac{3\pi}{4} \right] \tag{3.5}$$

but are rotated globally to cover the whole sphere. On both ends on the respective angular grid one usually adds four ghost-cells to ensure full overlap. The only connection between the separate sub-grids (Yin and Yang) during the solution of the hydrodynamic equations, is the exchange of data in these ghost-cells from one grid to the other via linear interpolation with appropriate weights to account for the different areas of overlap.

3.1.2   Gravity

Both codes employ a 3D gravitational potential with the general relativistic monopole correction of Marek et al. (2006), while higher multipoles are obtained from a solution of Poisson's equation as described in Müller and Steinmetz (1995). Marek et al. (2006) use the Tolman-Oppenheimer-Volkoff (TOV) potential

$$\Phi_{\mathrm{TOV}}(r) = -4\pi G \int_0^r \left[\frac{m_{\mathrm{TOV}}}{4\pi} + \frac{r'^3(P + p_\nu)}{c^2} \right] \frac{1}{\Gamma^2} \left(\frac{\rho c^2 + \rho\epsilon + P}{\rho c^2} \right) \frac{\mathrm{d}r'}{r'^2}, \tag{3.6}$$

where ϵ is the specific energy, G the gravitational constant, P the pressure, c the speed of light, p_ν the neutrino pressure, m_{TOV} the TOV-mass given by

$$m_{\mathrm{TOV}}(r) = 4\pi \int_0^r \left(\rho \frac{\rho\epsilon + E}{\rho c^2} + \frac{vF}{\Gamma c^2} \right) \Gamma r'^2 \mathrm{d}r'. \tag{3.7}$$

and the metric function Γ,

$$\Gamma = \sqrt{1 + \frac{v^2}{c^2} - \frac{2Gm_{\mathrm{TOV}}}{rc^2}}. \tag{3.8}$$

In the above equation v is the radial velocity of the material.

3.2 The Prometheus-HOTB Code

3.2.1 α-Network

At the late stages of the evolution of a massive star and especially during an explosive event, temperatures are large enough so that nuclear reactions become dynamically important. To account for the energy release by nuclear reactions and to give a rough estimate of the nucleosynthesic products of supernova explosions, PROMETHEUS-HOTB keeps track of free neutrons and protons and a 13 species α-network including ^{4}He, ^{12}C, ^{16}O, ^{20}Ne, ^{24}Mg, ^{28}Si, ^{32}S, ^{36}Ar, ^{40}Ca, ^{44}Ti, ^{48}Cr, ^{52}Fe, ^{56}Ni and an additional tracer nucleus Tr, which traces the production of neutron-rich nuclei and replaces ^{56}Ni in an environment with low electron fraction $Y_e < 0.49$. These nuclear species are treated as nonrelativistic Boltzmann gases. Nuclear reactions are followed when temperatures exceed $T \geq 10^8$ K up to T_{NSE} and densities are within $10^3\,\mathrm{g/cm^3} \leq \rho \leq 10^{11}\,\mathrm{g/cm^3}$. Above T_{NSE} we assume nuclear statistical equilibrium (see Section 3.2.2).

Species are evolved with the flow according to

$$\frac{\partial Y_i}{\partial t} + \nabla(\boldsymbol{v}\rho Y_i) = 0 \tag{3.9}$$

where Y_i is the number fraction of the respective species. To reduce numerical diffusion of the isotopes across shocks, the Consistent-Multifluid-Advection (CMA) scheme of Plewa and Müller (1999) is used.

The energy release or consumption by nuclear reactions is calculated as

$$\delta t Q_{\mathrm{nuc}} = n_{\mathrm{B}} \Delta \bar{m} c^2 = n_{\mathrm{B}} \sum_i (Y_{i,t} - Y_{i,t+\delta t}) B_i(Z, A), \tag{3.10}$$

where $\bar{m}$ is the mean baryon mass, n_{B} the total baryon number and $B_i(Z, A) = [(A - Z)m_{\mathrm{n}} + Z m_{\mathrm{p}} - m_i]c^2$ is the binding energy per nucleus i and m_{p}, m_{n} the proton and neutron mass.

After one hydrodynamic time step we solve the reaction equation

$$\frac{dY_i}{dt} = f(T, \rho, Y_e) = \dot{R}(T, \rho, Y_e), \tag{3.11}$$

where $\dot{R}$ is the matrix of reaction rates, by an implicit Euler method, using substeps of size Δt_{burn} in order to guarantee numerical stability. The time step Δt_{burn} for the integration is set such that the internal energy change due to burning is less than 5%. A particular disadvantage of the Euler method is that the necessary time step is not known a-priori.

If the estimated time step is too large, it has to be reset and the matrix inversion has to recomputed until the time step fulfills the energy criterion.

As noted by Timmes and Arnett (1999), more precise and faster evolution of the reaction network can be achieved by the Bader-Deuflhard semi-implicit midpoint method in conjunction with the GIFT sparse matrix solver (Gustavson et al., 1970).

The Bader-Deuflhard method discretizes Equation 3.11 by

$$Y_{n+1} - Y_n = 2\Delta t\, \mathbf{f}\Big(\frac{Y_{n+1} - Y_n}{2}\Big) \tag{3.12}$$

Linearizing the RHS yields

$$\Big[\mathbf{1} - \Delta t\frac{\partial \mathbf{f}}{\partial \mathbf{Y}}\Big] \cdot Y_{n+1} = \Big[\mathbf{1} + \Delta t\frac{\partial \mathbf{f}}{\partial \mathbf{Y}}\Big] \cdot Y_{n-1} + 2\Delta t\Big[\mathbf{f}(Y_n) - \Delta t\frac{\partial \mathbf{f}}{\partial \mathbf{Y}} \cdot Y_n\Big] \tag{3.13}$$

In conjunction with a first semi implicit Euler step and a smoothing step

$$\overline{Y} = 1/2\,(Y_{n+1} + Y_{n-1}) \tag{3.14}$$

the definition $\Delta_k = Y_{k+1} + Y_{k-1}$ and $\Delta t = H/m$ the algorithm, beginning with the first step, reads

$$\Delta_0 = \Big[\mathbf{1} - \Delta t\frac{\partial \mathbf{f}}{\partial \mathbf{Y}}\Big]^{-1} \cdot \Delta t\mathbf{f}(Y_0)Y_1 = Y_0 + \Delta_0 \tag{3.15}$$

Then for $k = 1, ..., m-1$ set,

$$\Delta_k = \Delta_{k-1} + 2\Big[\mathbf{1} - \Delta t\frac{\partial \mathbf{f}}{\partial \mathbf{Y}}\Big]^{-1} \cdot [\Delta t\mathbf{f}(Y_k) - \Delta_{k-1}]Y_{k+1} = Y_k + \Delta_k \tag{3.16}$$

and finally,

$$\Delta_m = \Big[\mathbf{1} - \Delta t\frac{\partial \mathbf{f}}{\partial \mathbf{Y}}\Big]^{-1} \cdot [\Delta t\mathbf{f}(Y_m) - \Delta_{m-1}]\overline{Y}_m = Y_m + \Delta_m \tag{3.17}$$

By employing the above steps with a series of $m = [2, 6, 10, 14, 22, 34, 50, ...]$ the overall cost of solving the nuclear reaction rates can be significantly reduced by up to 50% as can be seen in Figure 3.1.
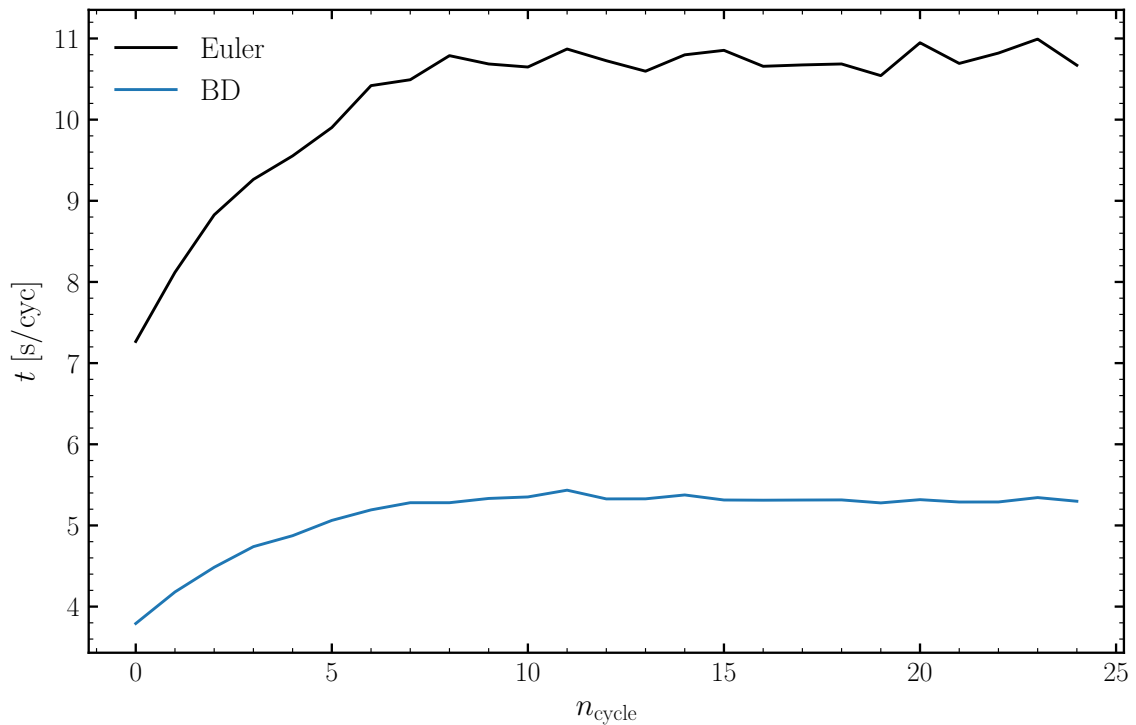
Fig. 3.1 Time per computational cycle in seconds vs computed steps with the Euler (black) method and Bader-Deuflhard (BD) method (blue). The e8.8 progenitor described in the next chapter was used in this full 4π test simulation. The Bader-Deuflhard method is about twice as fast.

As our α-network does not take the recombination of neutrons and protons to heavier nuclei into account, we allow them to recombine instantaneous into He4 when densities and temperatures fall below T_{NSE}. We add the mass fractions of neutrons and protons to the helium mass fraction and account for the energy release. This basically overestimates the energy release by the recombination of neutrons and protons and violates charge/mass conservation. In a newer version of the code we allow only paired free neutrons and protons to recombine to ^{4}He, thus also satisfying charge conservation.

Cooling of the newly born neutron star proceeds by the emission of neutrinos and thus lepton number. Consequently, the electron fraction in the surrounding matter can drop to values of ≈ 0.1 altering the nucleosynthesis significantly. In order to capture an "effective" neutronization of the expelled matter, which is not traceable with our symmetric α-network, we add a tracer nucleus "Tr" to our composition. It replaces ^{56}Ni when the electron fraction falls below 0.49 and thus helps estimating the error related to our α-Network.

3.2.2 Thermodynamic Regimes and the Equation of State

During the collapse and the subsequent phases of a supernova explosion, simulations need to cover densities and temperatures over several orders of magnitude. In order to accurately describe the thermodynamical states important in these phases, PROMETHEUS-HOTB employs several suitable equations of states (EoS).

High Density Equation of State

As the neutron star forms the central density easily exceeds ρ_{HD} (usually set to 10^{11} g/cm^3) by a few magnitudes. At such high densities nuclear forces which are not accounted for by the Helmholtz-EoS, become important. PROMETHEUS-HOTB uses the high density EoS of Lattimer and Swesty (1991) with an incompressibility modulus of bulk nuclear matter of $K = 220$ MeV. It is based on a liquid drop model and takes neutrons, protons and a representative heavy nucleus as the constituents of the high density matter. This heavy nucleus is assigned a non integer mean nuclear weight and charge. In PROMETHEUS-HOTB we assign the abundance of the heavy nucleus to the element with the closest nuclear weight. If matter is neutron rich ($Y_{\mathrm{e}} < 0.49$) and the nuclear weight exceeds $56\,\mathrm{u}$ the representative nucleus is traced by Tr.

Nuclear Statistical Equilibrium

At very high temperatures ($T \geq T_{\mathrm{NSE}}$) one can assume nuclear statistical equilibrium (NSE) to be fulfilled. At these temperatures, forward and reverse reactions are fast and energetic enough to balance each other. The composition of matter in this regime can be described analytically, using Maxwell-Boltzmann statistics, the chemical potential and binding energy of the nuclei. Above ρ_{HD} the high-density EoS provides the number of free neutrons, protons, α-particles and the mean mass number of a representative heavy nucleus. With this we set the composition to the nucleus closest to the mean mass number. At densities less than ρ_{HD} the given thermodynamic state is used to get the composition by interpolating a NSE-table (Ertl 2016, private communication) including neutrons, protons, the nuclei of the α-network and the racer nucleus Tr.

Low Densities and Temperatures

Below ρ_{HD} and $\mathrm{T_{NSE}}$ the thermodynamic relations are covered with the EoS of Timmes and Arnett (1999), also called "Helmholtz-EoS". It is an analytical equation of state based on the minimization of the free energy and uses a fifth order Hermite-polynomial interpolation of a table for the electron-positron gas. Below the table boundaries of the Helmholtz-EoS

($\rho_{\text{low}} = 10^{-10}$ g/cm^3, $T_{\text{low}} = 10^4$ K) the equation of state is simplified to include only the pressure contributions by a set of Boltzmann gases and by radiation. The pressure p and the specific internal energy e are then given by

$$p = \frac{1}{3}aT^4 + \frac{k_{\text{b}}}{\mu m_{\text{H}}}\rho T \tag{3.18}$$

$$e = \frac{aT^4}{\rho} + \frac{3k_{\text{b}}}{2\mu m_{\text{H}}}T, \tag{3.19}$$

where a, k_{b}, ρ, T, m_{H}, μ are the radiation constant, Boltzmann constant, density, temperature, atomic mass unit and mean molecular weight respectively. Note that full ionization is assumed in this approach and radiation pressure clearly dominates the shocked region.

The EoS routine calculates all thermodynamic quantities given a certain temperature, density, charge and mean molecular weight. As for most supernova codes temperature considered in the conservation laws, so that the internal energy is used as an input. The new thermodynamic state is calculated via a Newton-Raphson iteration given the internal energy.

3.2.3   Collapse and Post-Bounce Simulation in Prometheus-HOTB

Since the high density equation of state for hot neutron stars is still unknown and large uncertainties in the neutrino interaction rates still plague even the most sophisticated neutrino transport schemes, PROMETHEUS-HOTB compiles these uncertainties into its central engine. In the following we describe the approach PROMETHEUS-HOTB uses to simulate the collapse and the onset of explosion.

Deleptonization and Core Bounce

When the core of a massive star becomes unstable, it collapses and emits most of the released gravitational binding energy in neutrinos. Since the physics of this supersonic infall-phase is well understood and does not depend on details in the neutrino-transport, it is justified to use a simple deleptonization scheme. In PROMETHEUS-HOTB we use the scheme of Liebendorfer (2005) for different regimes of the infall region. When densities are above $\rho \approx 2 \times 10^{12}$ g/cm^3 the electron fraction Y_{e} can be described only as a function of ρ and thus can be followed by extracting $Y_{\text{e}}(\rho)$ profiles of first-principle simulations. When densities are below 2×10^{12} g/cm^3, we are in the semi-transparent regime. Here neutrinos thermalize on their way towards the surface, depositing a small amount of their energy in the matter. The thermalization process ceases when neutrinos reach their mean escape

energy E_ν^{esc} which is defined as the energy needed to fulfill $\mu_{\text{e}} - \mu_{\text{n}} + \mu_{\text{p}} - E_\nu^{\text{esc}} > 0$. Here μ_{e}, μ_{n}, μ_{p}, are the chemical potentials of electrons, neutrons and protons respectively. The deposited energy is accounted for by an entropy source term

$$\frac{\delta s}{\delta t} = -\frac{\delta Y_{\text{e}}}{\delta t} \frac{\mu_{\text{e}} - \mu_{\text{n}} + \mu_{\text{p}} - E_\nu^{\text{esc}}}{T},\tag{3.20}$$

where T is the matter temperature. When the neutrino mean energy falls below the escape energy, they are freely escaping the star.

Boundary Movement

During collapse we include the center of the pre-SN state up to a radius far outside the the gravitationally unstable region. When the central densities of the core pass 10^{13} g/cm^3 and central entropies are greater than 3, the core bounces. At this point in time we move the inner boundary to a radius $R_{\text{ib},0.5}$ where the enclosed baryonic mass equals $0.5\,\text{M}_\odot$. We impose hydrostatic equilibrium as our inner boundary condition as also described by Janka and Müller (1996). Neutrino luminosities at $R_{\text{ib},0.5}$ are set to a constant value of $L_{\text{ib}} = 10^{52}$ erg/s until the shock passes the 1.25 M$_\odot$ shell a few milliseconds later. This marks our next step in our simulation approach. The radius of our inner boundary is moved to the $M(R_{\text{ib}}) = 1.1\,\text{M}_\odot$. In order to account for the contraction of the PNS, R_{ib} follows

$$R_{\text{ib}}(t) = R_{\text{ib,final}} + \left(R_{\text{ib,ini}} - R_{\text{ib,final}}\right) e^{-t/t_0},\tag{3.21}$$

where $R_{\text{ib,ini}}$ and $R_{\text{ib,final}}$ are the initial and the final radius of the 1.1 M$_\odot$ shell and t_0 the timescale for the boundary movement.

Core Neutrino Luminosities

Similar to Ugliano et al. (2012), we describe the neutrino luminosities emerging from the excised inner part by an analytical estimate. The basis of this one-zone cooling model is the assumption that the core is in hydrostatic equilibrium and in pressure equilibrium between the core radius R_{c} (which is in general different to R_{ib}). Using this, one can use the Virial-theorem to describe to total neutrino luminosity at $R_{\text{c}}(t)$ as

$$L_{\nu,\text{tot}} = -\frac{2}{5}\frac{3\Gamma - 4}{3(\Gamma - 1)}\frac{GM_{\text{c}}^2 \dot{R}_{\text{c}}}{R_{\text{c}}^2} - \frac{3\Gamma - 4}{3(\Gamma - 1)}\frac{aGM_{\text{c}}m_{\text{acc}}\dot{R}_{\text{c}}}{R_{\text{c}}^2} - \frac{aGM_{\text{c}}\dot{m}_{\text{acc}}}{3(\Gamma - 1)R_{\text{c}}}\tag{3.22}$$

Here $\Gamma = 3$ is the adiabatic index of the core model, G is the Gravitational constant, M_{c} the core mass, a an efficiency parameter of the accretion luminosity and m_{acc} the mass

contained between R_c and the radius at which the density falls below $\rho_0 = 10^{10}$ g/cm^3. We define $\dot{m}_{acc} = 4\pi r_0^2 v_0 \rho_0$, where r_0 and v_0 is the radius at $\rho = \rho_0$. defined In the axis-symmetric and three-dimensional cases Δm_{acc} is determined from angle averaged quantities. The time evolution of the core radius follows a power-law

$$R_c(t) = R_{c,final} + (R_{c,ini} - R_{c,final})\Big(\frac{t + t_L}{t_L}\Big)^p, \tag{3.23}$$

where $t_L = 1$ s and $p < 0$. Initially $R_c = R_{ib}$ and $R_{c,final}$ is adjusted such that the inner core emits enough neutrinos to enable a successful explosions.

With these prescriptions the set of parameters ($R_{c,final}$, $R_{ib,final}$, a, p) is complete and can be calibrated to match observations or results from simulations with a more advanced neutrino transport scheme.

Note that due to PdV-Work and neutrino losses at the inner boundary, the m_{TOV} mass (see Section 3.1.2) evolves over time and has to be adjusted according to

$$m_{TOV}(R_{ib}, t) = m_{TOV}(R_{ib}, 0) - \int_0^t L_\nu^{ib} dt' - \int_0^t 4\pi R_{ib}^2(t') P_{ib}(t') \frac{dR_{ib}}{dt'}. \tag{3.24}$$

Grey Neutrino-Transport Scheme

Neutrinos play an important role in stellar physics and are the decisive ingredient during the explosion of a star. They represent the only efficient way of cooling the PNS during and after collapse. Although their cross-sections for interactions with matter are very small, the number density of neutrinos is large enough to heat up the surroundings of the neutron star considerably, help to unbind matter and thus enable explosions. The transport of neutrinos of every species is described by the Boltzmann equation

$$\frac{1}{c}\frac{\partial \mathcal{I}}{\partial t} + \hat{\boldsymbol{n}}\nabla \mathcal{I} = S(\mathcal{I}) \tag{3.25}$$

where $\mathcal{I} = \mathcal{I}(\boldsymbol{r}, \hat{\boldsymbol{n}}, \epsilon, t)$ is the specific intensity, $\hat{n}$ is the normal vector and S a source term. The specific intensity is defined, with the particle distribution function $f(\boldsymbol{r}, \boldsymbol{p}, t)$, as $\mathcal{I} = \frac{\epsilon^3}{h^3 c^3} f$ where ϵ is the mean neutrino energy, h is Planck's constant and c the speed of light. Due to the high dimensionality of the Boltzmann equation and its integro-differential character, it is computationally very expensive to solve. Because of this, PROMETHEUS-HOTB employs several simplifications to the transport equation. Assuming spherical symmetry Equation (3.25) simplifies to

$$\frac{1}{c}\frac{\partial I}{\partial t} + \mu\frac{\partial}{\partial r}I + \frac{1 - \mu^2}{r}\frac{\partial}{\partial \mu}I = S, \tag{3.26}$$

where θ and $\mu = \cos\theta$ is the angle between radiation propagation and radial direction. Integrating over the solid angle $d\Omega$ and energy yields

$$\frac{\partial}{\partial t}E + \frac{1}{r^2}\frac{\partial}{\partial r}(r^2 F) = Q^+ - Q^-. \tag{3.27}$$

Here S was split up into the emission term Q^+ and an absorption term $Q^- = \kappa_a cE$, where κ_a is the opacity. Further considering, that the flux-factor $f(r,t) = F(r,t)/cE(r,t)$ does not change over time and using the neutrino luminosity $L = 4\pi r^2 F = 4\pi r^2 fcE$, one arrives at

$$\frac{\partial}{\partial t}L + c_{\text{eff}}\frac{\partial}{\partial r}L = 4\pi r^2(Q^+ - Q^-), \tag{3.28}$$

where $c_{\text{eff}} = cf(r,t)$. With a given a flux-factor and under the assumption that the source terms Q^+ and $\tilde{\kappa} = \kappa_a/f = 4\pi r^2 Q^-/L$ are not changing over a distance $r(t) = r_0 - c_{\text{eff}}t$, one can solve Equation (3.28) analytically, giving

$$L(r,t) = L(r^*,t^*)e^{-\tilde{\kappa}c_{\text{eff}}(t-t^*)} + \frac{4\pi Q^+}{\tilde{\kappa}^3}\times$$
$$\left\{[1 - e^{-\tilde{\kappa}c_{\text{eff}}(t-t^*)}][1 + (\tilde{\kappa}r^* - 1)^2] + \tilde{\kappa}c_{\text{eff}}(t-t^*)[2\tilde{\kappa}r^* + \tilde{\kappa}c_{\text{eff}}(t-t^*) - 2]\right\}. \tag{3.29}$$

Further details about the choice of characteristics and interpolations onto $L(r^*,t^*)$ can be found in Scheck et al. (2006). In order to calculate the source terms in Equation (3.26) one needs to make an assumption about the energy spectrum of the neutrinos. We assume a time-independent Fermi-Dirac

$$\mathcal{F}_n(\eta) = \int_0^\infty \mathrm{d}x\, x^n f_{\text{FD}}(x,\eta) \tag{3.30}$$

shaped energy spectrum of neutrinos, where $f_{\text{FD}}(x,\eta) = \frac{1}{1-\exp(x-\eta)}$ and η is the degeneracy parameter dependent on the optical depth τ_ν

$$\eta_\nu = \eta_{\text{eq},\nu}(1 - e^{-\tau_\nu}) + \eta_{0,\nu}e^{-\tau_\nu}. \tag{3.31}$$

In the above equation $\eta_{\text{eq},\nu}$ is the equilibrium degeneracy parameter and $\eta_{0,\nu}$ is a value for the $\tau \to 0$ limit of η extracted from more advanced neutrino transport calculations. Using the above equations and an approximation for the flux factor $f_\nu(\tau_\nu)$[1] one can calculate the source terms caused by various interactions. Prometheus-HOTB includes inelastic charged-current processes

$$\nu_{\text{e}} + \text{n} \rightleftharpoons \text{p} + \text{e}^- \tag{3.32}$$

---

[1]For a detailed description the reader is referred to Scheck et al. (2006)

and

$$\bar{\nu}_e + p \rightleftharpoons n + e^+. \tag{3.33}$$

Thermal pair-production is accounted for via

$$e^+ + e^- \rightleftharpoons \bar{\nu}_i + \nu_i \text{ with } i = e, \mu, \tau \tag{3.34}$$

and elastics neutrino scattering off nuclei (A), neutrons (n), protons (p), electrons (e$^-$) and positrons (e$^+$)

$$\nu_i + x \rightleftharpoons \nu_i + x \text{ with } x = A, n, e^+, e^-, p \tag{3.35}$$

is also considered.

Correction to Neutrino-Nucleon Scattering

In most cases the treatment of neutrinos described in the previous section provides a good fit to the solution of the full Boltzmann-Transport Equation and is computationally very cheap. However, through the energy integration of the energy source terms which are necessary for calculating the neutrino fluxes, an inconsistency arises in the treatment of the neutrino-nucleon scattering. Scheck et al. (2006) uses the scattering term calculated by Tubbs (1979)

$$\begin{aligned}
Q_{\nu N} = &\frac{1}{4} \frac{\sigma_0 c}{(m_e c^2)^2} \mathcal{C}_N \mathcal{E}_N \frac{n_N}{m_N c^2} \{\langle \epsilon^4 \rangle - 6T \langle \epsilon^3 \rangle\} \\
&\times \frac{L_{e,\nu}}{4\pi r^2 f_\nu \langle \epsilon \rangle},
\end{aligned} \tag{3.36}$$

which is their equation (D.68). Here $\langle \epsilon \rangle$ is the mean neutrino-energy and T the temperature of the thermal target in MeV. In certain cases, especially in higher mass stars and long duration simulations ($t_{pb} > 3$ sec), the temperature exceeds $\langle \epsilon^4 \rangle / 6 \langle \epsilon^3 \rangle$, consequently changing the sign of $Q_{\nu N}$. As the scattering term in Equation (3.36) is implemented solely as an energy sink for neutrinos, the transport scheme becomes unstable and causes strong numerical oscillations in the neutrino-fluxes. Due to the tight coupling of fluxes and source-terms, strong gradients in the fluxes cause a strong response in the total source terms Q^+, Q^-. This heats up material around the neutron star and creates artificially high neutrino fluxes. A simple solution to this problem is to separate the temperature-dependent term and split Equation (3.36) into two separate energy source and sink terms

$$Q_{\nu N}^{em} = -\frac{3}{2} \frac{\sigma_0 c}{(m_e c^2)^2} \mathcal{C}_N \mathcal{E}_N \frac{n_N}{m_N c^2} T \langle \epsilon^3 \rangle \frac{L_{e,\nu}}{4\pi r^2 f_\nu \langle \epsilon \rangle}, \tag{3.37}$$

$$Q_{\nu N}^{abs} = \frac{1}{4} \frac{\sigma_0 c}{(m_e c^2)^2} \mathcal{C}_N \mathcal{E}_N \frac{n_N}{m_N c^2} \langle \epsilon^4 \rangle \frac{L_{e,\nu}}{4\pi r^2 f_\nu \langle \epsilon \rangle}. \tag{3.38}$$

3.3 The Vertex-Prometheus Code

Identical to PROMETHEUS-HOTB, VERTEX-PROMETHEUS is based on the hydrodynamics solver Prometheus which is coupled with a three-flavor, energy-dependent, ray-by-ray-plus (RbR+) neutrino transport scheme that iteratively solves the neutrino energy and momentum equations with a closure determined from a tangent-ray Boltzmann solver. It is thus able to include the PNS into the computation and capture neutrino interactions more accurate compared to the gray solver of PROMETHEUS-HOTB. For a detailed description of the physics and numerical procedures involved the reader is referred to Rampp and Janka (2002). VERTEX-PROMETHEUS also employs a 3D gravitational potential with general relativistic corrections to the monopole Marek et al. (2006) and the Yin-Yang grid following the implementation of Melson et al. (2015a). At high densities ($\rho \geq \rho_{HD} = 10^{11}\,\mathrm{g/cm^3}$) VERTEX-PROMETHEUS uses the EoS of Lattimer and Prakash (2000) with a nuclear incompressibility of K = 220 MeV. At low densities ($\rho \leq \rho_{HD}$) VERTEX-PROMETHEUS uses the EoS of Janka (1999) which includes the contributions of arbitrarily degenerate and relativistic e^+/e^- and nonrelativistic nucleons and nuclei. The relative abundances of 23 nuclear species are determined by a nuclear statistical equilibrium (NSE) solver in regions with temperatures above $T_{NSE} = 5 \times 10^9\,\mathrm{K}$. Below T_{NSE} a flashing scheme is used to approximately treat nuclear burning (see Rampp and Janka 2002).

Chapter 4

Evolution During the First Second

The following chapter focuses on the onset of the explosion of our models, so roughly the first second(s). Special attention is given to the energetics of the respective explosion, multidimensional effects, nucleosynthesis and redistribution of chemical elements in mass and velocity space due to non-radial motions.

4.1 Collapse and Post-bounce Setup in Prometheus-HOTB

As stated before, we simulated the collapse onset of the explosion of model e8.8 with PROMETHEUS-HOTB. We use the Lattimer & Swesty EoS (Lattimer and Swesty, 1991) for densities above $\rho_{\mathrm{HD}} = 10^{11}\,\mathrm{g/cm^3}$. At lower densities the EoS of Timmes and Arnett (1999) is used. $\mathrm{T_{NSE}}$ is set to $9 \times 10^9\,\mathrm{K}$ to make full use of our α-network. A non-equidistant geometrically increasing radial grid of 2000 zones ranging to $1 \times 10^5\,\mathrm{km}$ is used in the 1D and 2D simulations. In the 3D simulation we reduce the number of cells to 1400 for computational efficiency. The angular resolution of the multi-dimensional simulations is set to $2°$ employing the Yin-Yang grid for the full 4π simulation. After collapse we impose random density perturbations with an amplitude of 0.1% in the multi-dimensional simulations to break the spherically-symmetric initial condition. In Table 4.1 we list the parameter values of the PNS core model used for a set of simulations of model e8.8 (see also Sections 3.2.3 and 3.2.3). This allows us to span a wide range in explosion energies (as defined in Equation (4.2)) between $0.3 - 1.5 \times 10^{50}\,\mathrm{erg}$. These values are representative for the estimates of explosion energy found in previous studies of ESCNe (von Groote 2014; Radice et al. 2017), as well as the estimated kinetic energy of the ejecta in case of SN1054, which is close to $0.7 \times 10^{50}\,\mathrm{erg}$ (Smith, 2013). We computed the post-bounce evolution of the ESCN progenitor using 1D and 2D simulations for each of the calibrations listed

Table 4.1 Summary of the PNS core parameter values and resulting explosion energies used for the e8.8 model from 1D simulations. The explosion energy is essentially independent of dimensionality (1D, 2D, 3D)

Model	E_{exp} [foe]	p [index]	a [factor]	$R_{\mathrm{ib,f}}$ [km]	t_0 [s]	$R_{\mathrm{c,f}}$ [km]
e8.8$_3$	0.03	-3	1.0×10^{-2}	40	0.1	27
e8.8$_6$	0.06	-3	1.2×10^{-2}	40	0.1	22
e8.8$_{10}$	0.10	-3	4.0×10^{-1}	40	0.1	20
e8.8$_{15}$	0.15	-3	5.8×10^{-1}	40	0.1	18

in Table 4.1. We choose the e8.8$_{10}$ calibration as our reference case for a 3D simulation motivated by the most energetic model of von Groote (2014) using similar physics.

4.1.1   Collapse and Post-bounce Setup in Vertex-Prometheus

The collapse of the pre-SN model is computed in 1D using the full set of neutrino interactions until 10 ms after bounce. Thereafter, the simulations are mapped onto the three-dimensional Yin-Yang grid and random cell-to-cell density perturbations are imposed with an amplitude of 0.1%. The simulations of the iron core progenitors were computed using a non-equidistant radial grid with initially 400 zones extending to 10^9 cm, which was refined in steps to more than 600 zones. This guarantees a resolution $\Delta r/r$ of better than 1% at the gain radius. The innermost 1.6 km are calculated in spherical symmetry to avoid time stepping constraints at the grid center. The angular resolution for the z9.6 model was set to 2°. The collapse and post-bounce evolution of model s9.0 were computed with a newly implemented static mesh refinement (SMR) scheme presented in Melson et al. (2019), which increased the resolution to 1° outside of the gain radius and to 0.5° exterior to a radius of 160 km. The simulations with full neutrino transport were too expensive to continue them to late post-bounce times. At $t_{\mathrm{pb}} \gtrsim 0.41\,\mathrm{s}$ for model z9.6 and at $t_{\mathrm{pb}} \gtrsim 0.49\,\mathrm{s}$ for model s9.0 the neutrino transport was therefore switched off and replaced by a simple scheme for neutrino heating and cooling, which ensures a seamless continuation with a minimum of transient artifacts. Details of this scheme are given in Appendix A.

In both simulations ρ_{HD} is set to $10^{11}\,\mathrm{g/cm^3}$. For unshocked, collapsing stellar matter we choose $T_{\mathrm{NSE}} = 0.5\,\mathrm{MeV}$, and for neutrino-heated postshock matter we take $T_{\mathrm{NSE}} = 0.5\,\mathrm{MeV}$ for the simulation of model z9.6 and $T_{\mathrm{NSE}} = 0.34\,\mathrm{MeV}$ for model s9.0.

4.2   Energetics and Shock Propagation

In the following we provide a brief overview of the post-bounce phase. The reader is referred to Melson et al. (2015b) and Melson et al. (2019) for a detailed analysis of the post-bounce phase of the iron core progenitors in VERTEX-PROMETHEUS simulations. Generic features of the explosion of ECSNe are given in Kitaura et al. (2006); Janka et al. (2008); Fischer et al. (2010); Radice et al. (2017); Gessner and Janka (2018). Since our results closely resemble these previous findings, we summarize the most important features in the following. In Figure 4.1 we show the evolution of the angle-averaged radius of the supernova shock and the diagnostic explosion energy of our three-dimensional simulations during the post-bounce phase. The angle-averaged shock radius is calculated as

$$\langle R_{\mathrm{sh}} \rangle = \frac{1}{4\pi} \int R_{\mathrm{sh}}(\theta, \phi) \mathrm{d}\Omega, \tag{4.1}$$

where $\mathrm{d}\Omega = \sin\theta \mathrm{d}\theta \mathrm{d}\phi$. The diagnostic explosion energy at all times is given by the integral of the total energy density, defined as $e_{\mathrm{b}} = e_{\mathrm{int}} + e_{\mathrm{kin}} + e_{\mathrm{grav}}$, in the postshock region over volume elements where it has a positive value

$$E_{\mathrm{exp}} = \int_{V_{\mathrm{postshock}}} \mathrm{d}V \, e_{\mathrm{b}}, \quad e_{\mathrm{b}} > 0. \tag{4.2}$$

The sharp drop in density outside the ONeMg-core of model e8.8 leads to an early and strong drop in the accretion rate and hence ram pressure at the shock. Consequently, the forward shock expands rapidly and reaches the core/envelope boundary ($R_{\mathrm{He/H}} = 1210\,\mathrm{km}$), at 0.21 s after core bounce. This is in stark contrast to the typical core-collapse supernova, where the high ram pressure stalls the shock expansion significantly for several 100 ms. The explosion energy starts rising steeply as soon as the forward shock leaves the ONeMg core.
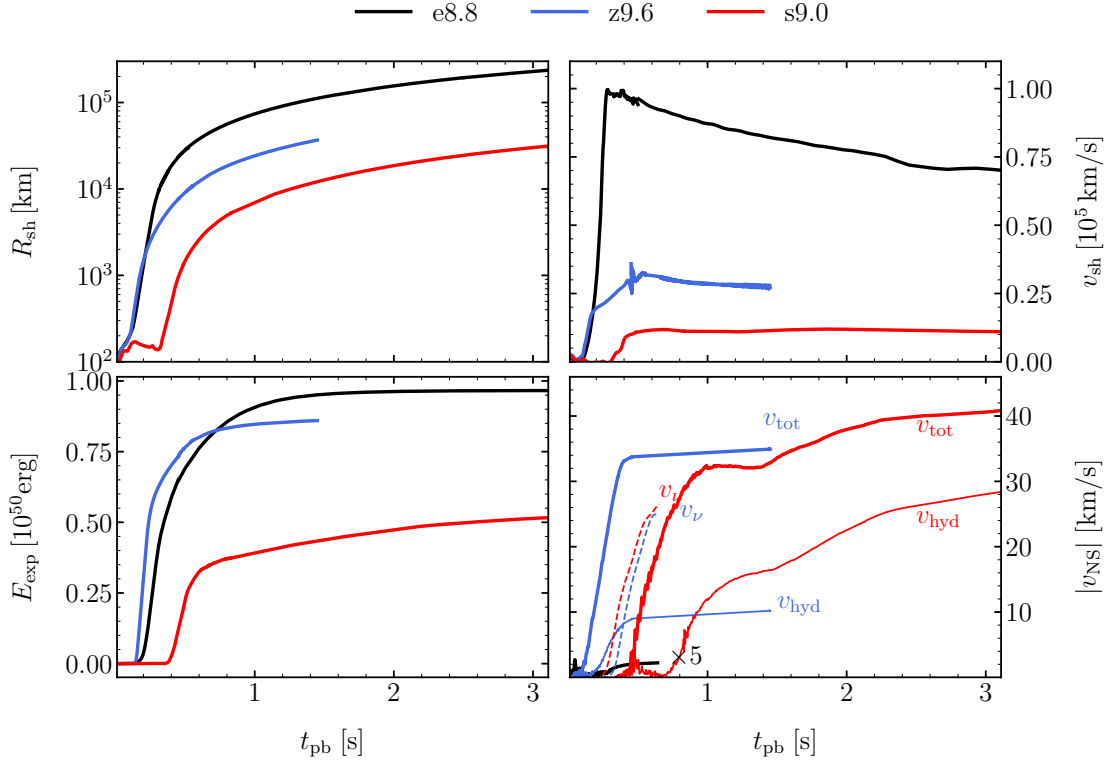
Fig. 4.1 Shock radius (upper left panel), shock velocity (upper right panel) and diagnostic explosion energy (lower left panel) versus post-bounce time for all of our 3D models. We also show the total PNS kick velocities (thick lines) hydrodynamically induced PNS kick velocities (thin lines) and neutrino induced PNS kick velocities (dashed lines) in the lower right panel. The differences between both velocities is associated with the PNS kicks caused by asymmetric neutrino emission due to the LESA phenomenon (see text for details). For the iron core progenitors we can track only hydrodynamic contributions to the kick after the transport module of VERTEX-PROMETHEUS is switched off at $t_{\mathrm{pb}} = 0.41$s and $t_{\mathrm{pb}} = 0.49$s for models z9.6 and s9.0, respectively, while for the ONeMg case our simplified neutrino treatment with the excised core of the PNS does not allow us to monitor the LESA induced kick. The kick of model e8.8 is scaled by a factor of 5 for better visibility.

The acceleration of the shock at the core/envelope boundary is followed by a huge deceleration at the lower boundary of the H-envelope (see upper right panel of Figure 4.1). This is caused by a sudden change of the density gradient at the core/envelope transition. Consequently, the neutrino-heated ejecta pile up in a dense, compressed and decelerated shell behind the SN shock.

The ECSN-like structure of model z9.6 is reflected in the evolution of the forward shock and growth of the diagnostic explosion energy. The shock radii remain almost perfectly

Table 4.2 Overview of PNS properties of our multi-dimensional models at t_{map}.

Model	t_{map} [s]	E_{exp}^{50} [erg]	$v_{\mathrm{NS,tot}}$ [km/s]	$v_{\mathrm{NS}}^{\mathrm{hyd}}$ [km/s]	v_{NS}^{ν} [km/s]	J_{NS}^{45} [cm²g/s]	θ_{vJ} [°]	α_{ej} [%]	α_{ν} [%]	M_{ns} [M$_\odot$]	R_{ns} [km]	M_{map} [M$_\odot$]	M_{g} [M$_\odot$]	P_{NS} [s]
e8.8$_3$ 2D	2.515	0.3	1.55	1.55	-	1.78	-	1.154	-	1.323	49.85	1.334	1.216	4.18
e8.8$_6$ 2D	2.515	0.6	0.94	0.94	-	2.75	-	0.041	-	1.316	50.22	1.327	1.210	2.69
e8.8$_{10}$ 2D	2.515	1.0	0.13	0.13	-	4.19	-	0.004	-	1.308	50.57	1.319	1.203	1.75
e8.8$_{15}$ 2D	2.515	1.5	0.59	0.59	-	1.67	-	0.011	-	1.299	50.86	1.309	1.195	4.37
e8.8 3D	0.470	1.0	0.44	0.44	-	0.70	90.0	0.004	-	1.307	50.57	1.311	1.197	10.46
z9.6 3D	1.440	0.86	34.90	10.16	24.89	2.55	45.4	4.623	1.35	1.340	20.98	1.340	1.221	2.93
s9.0 3D	3.140	0.48	40.87	28.45	26.46	8.05	31.3	10.02	1.18	1.350	19.58	1.351	1.230	0.94

Notes: All values are given at the end of our explosion simulations with neutrino treatment (t_{map}). $v_{\mathrm{NS}}^{\mathrm{tot}}$ is the total NS kick resulting from the hydrodynamic ($v_{\mathrm{NS}}^{\mathrm{hyd}}$) plus the neutrino-induced (v_{NS}^{ν}) contributions. We measure the contribution of neutrinos to the total kick until the neutrino transport is switched of at $t_{\mathrm{neut}} = 0.41$ s and $t_{\mathrm{neut}} = 0.49$ s after core bounce for models z9.6 and s9.0, respectively. Hydrodynamic contributions are taken until t_{map}. J_{NS} is the total angular momentum transported to the PNS through a radius of 100 km until t_{map}. θ_{vJ} is the angle between the direction of the total kick velocity $\boldsymbol{v}$ and the direction of $\boldsymbol{J}$. α_{ej} and α_{ν} are the final hydrodynamic and neutrino anisotropy-parameters, respectively (see Appendix A). For the iron core progenitors we average α_{ν} over the time the emission dipole is largest until the end of the simulation. M_{b} is the baryonic PNS mass, which is defined as the enclosed mass within the radius R_{NS}, at which the density drops below 10^{11} g/cm³. Note that for the simulations of the e8.8 progenitor, R_{ns} is determined by the chosen parameters of the inner grid boundary (see Table 4.1). M_{map} (see also Table 5.1) is the central mass contained within the excised region, from which we calculate the gravitational mass M_{g} for a PNS radius of 12 km. P_{NS} is the PNS spin period at the end of our post-bounce simulations, assuming a final PNS radius R_{NS} of 12 km, angular momentum conservation and a gravitational mass of M_{g}.

spherical in both the e8.8 and z9.6 models. The acceleration of the forward shock outside the iron core, however, ends earlier in the z9.6 case than in model e8.8, because of the more gradual change in the density profile. In both cases the explosion energies also start to rise early and saturate just after $t_{pb} \sim 1\,$s.

In contrast to the z9.6 and e8.8 models, model s9.0 lacks the very steep density gradient outside the Fe-core, as can be seen in Figure 2.2. The shock can expand initially up to $180\,$km at $t_{pb} \sim 130\,$ms but then enters a phase of recession. The arrival of the Si/O interface at the shock and the decreasing mass-accretion rate within the oxygen shell eventually lead to shock expansion at $\sim 0.3\,$s after bounce. Shock expansion is aided by strong convection behind the shock front. Similar to the results presented in Glas et al. (2019), who used the same progenitor, the model remains convection-dominated and does not exhibit any signs of the oscillatory growth of the standing-accretion shock instability (SASI) (Blondin et al., 2003; Foglizzo et al., 2007). However, although SASI does not develop in the simulation, the forward shock experiences large-scale deformation with a dipole amplitude of $\sim 10\%$ (compared to the angle-averaged shock radius). These deformations are driven by big plumes that form in the post-shock layer. Contrary to the ECSN-like models, strong non-radial motions persist around the PNS over several seconds after bounce. Continuous mass accretion onto the PNS through narrow funnels delays the emergence of the spherical neutrino-driven wind, which is why we needed to continue the simulations over three seconds after bounce. Explosion energy and shock velocity in model s9.0 remain considerably lower than in the other two progenitors (see Figure 4.1).
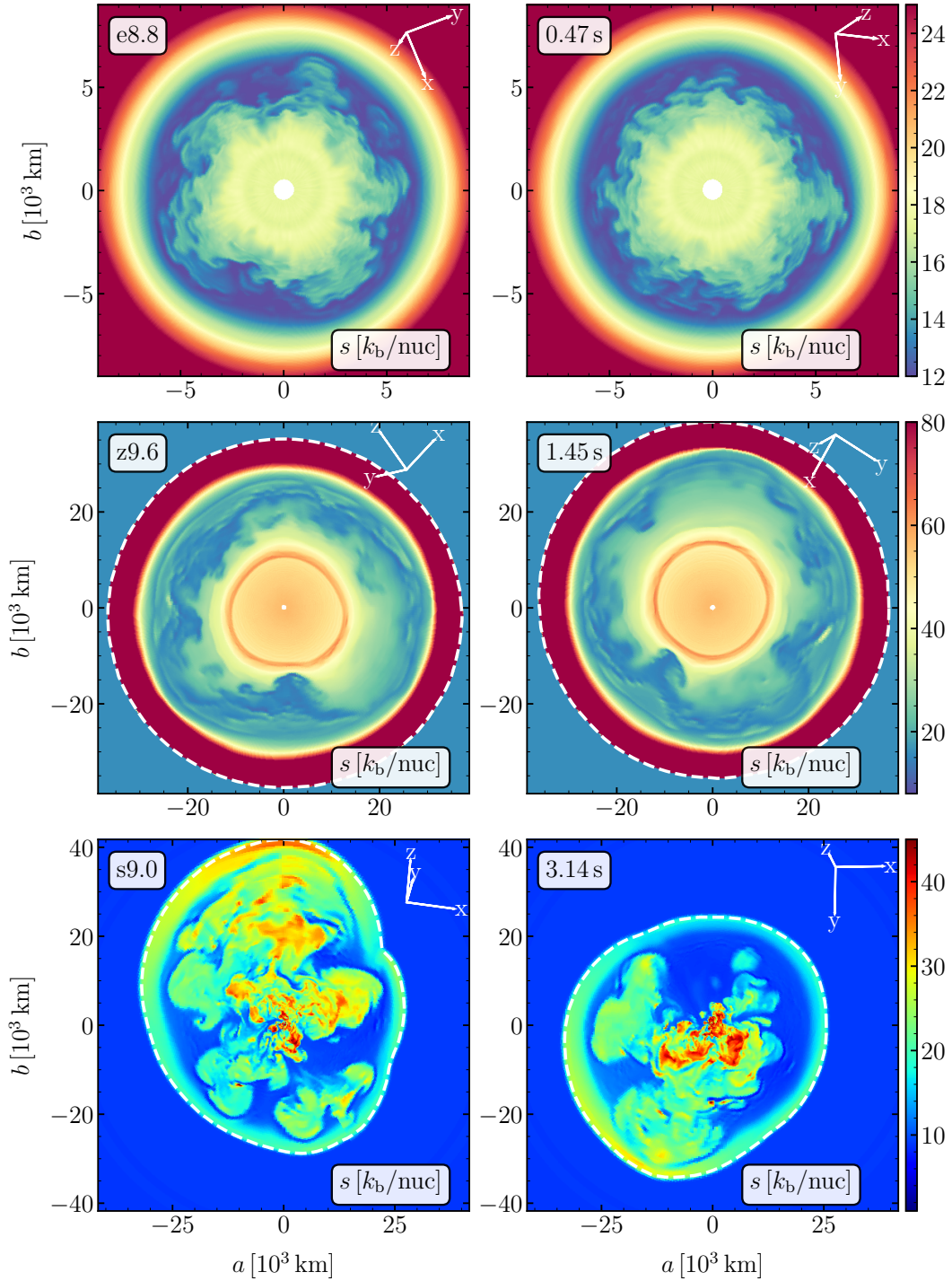
Fig. 4.2 Planar cuts of our 3D models showing the entropy color-coded at t_{map}. The left panels display cuts which are aligned such that the point of largest shock deformation is included in the plane. Therefore the coordinate directions of the plots have no association with the coordinates of the computational grid. The right panels show the plane of smallest shock expansion. Note the largely spherical morphology of model e8.8 and the deformed ejecta morphology of model s9.0. For better visibility of the small-scale structures of model s9.0 we chose a different color representation in this case. The white dashed line marks the shock surface. It is missing in the top two panels because in mode e8.8 the shock is at more than 20,000 km at this time already, far ahead of any explosion asymmetries.

In order to compare the final state of the post-bounce simulations of our model set, we present in Figure 4.2 planar cuts showing the entropy at the times t_{map} when we start our long-time simulations. The left panels are chosen such that they include the plane of the largest shock deformation. The right panels include the plane of the smallest shock deformation. Note the basically spherical shape of the shock and the mild post-shock asymmetries in both the e8.8 and z9.6 models. In strong contrast to the ECSN-like models, model s9.0 shows a clear dipolar shock deformation and ejecta morphology.

4.2.1 Neutron Star Properties

It is known from observations of young radio pulsars or pulsars in close binary systems, that neutron stars are born with kick velocities around $200-500\,\mathrm{km/s}$ (Janka, 2017). First, aspherical ejection of matter leads to a gravitational "tug" which accelerates the PNS in the opposite hemisphere of the maximum shock expansion and fastest ejecta. Second, anisotropic neutrino emission, due to the so-called "Lepton-Number Emission Self-sustained Asymmetry" (LESA) (Tamborra et al., 2014), can accelerate the PNS opposite to the direction of the largest total neutrino-energy flux. In the following we provide the theory to evaluate the hydrodynamic and neutrino-induced contributions to the PNS kick.

Using the momentum conservation equation the hydrodynamic NS kick can be simply estimated as

$$\boldsymbol{P}_{\mathrm{NS}} = \boldsymbol{v}_{\mathrm{NS}} M_{\mathrm{b}} = -\boldsymbol{P}_{\mathrm{gas}}, \tag{4.3}$$

where M_{b} is the baryonic (PNS) mass contained inside the radius R_{NS} where the angle-averaged density drops below $10^{11}\,\mathrm{g/cm^3}$ and $\boldsymbol{P}_{\mathrm{gas}} = \int_{R_{\mathrm{NS}}}^{\infty} \rho \boldsymbol{v} \mathrm{d}V$ is the momentum of the ejecta outside the PNS. The momentum transfer by neutrinos is given by

$$\dot{\boldsymbol{P}}_{\nu}(t) = \oint_{r=R_{\mathrm{gain}}} \frac{F_{\nu}}{c}\, \boldsymbol{e}_r\, \mathrm{d}S = -\dot{\boldsymbol{P}}_{\mathrm{ns}}^{\nu}(t)\,, \tag{4.4}$$

where F_{ν} is the neutrino energy flux, c the speed of light, $\boldsymbol{e}_r$ the unit vector in radial direction and R_{gain} is the so-called "gain radius", which is the radius where neutrino cooling balances neutrino heating. Due to the RbR approximation in VERTEX-PROMETHEUS, only radial momentum flux has to be considered. Assuming the PNS mass does not change significantly ($\dot{M}_{\mathrm{b}} = 0$), and using $\boldsymbol{P}_{\nu}(t) = \int_0^t \dot{\boldsymbol{P}}_{\nu}(t')\mathrm{d}t'$, the velocity of the NS can be calculated as

$$\boldsymbol{v}_{\mathrm{NS}}(t) = -\frac{\boldsymbol{P}_{\mathrm{gas}} + \boldsymbol{P}_{\nu}}{M_{\mathrm{b}}}. \tag{4.5}$$

.

One can connect the asymmetry of the ejecta and neutrino emission by the means of an anisotropy parameter. The hydrodynamic parameter reads

$$\alpha_{\text{ej}} = \frac{|\boldsymbol{P}|_{\text{gas}}}{P_{\text{ej}}} \tag{4.6}$$

where

$$P_{\text{ej}} = \int_{R_{\text{NS}}}^{R_{\text{sh}}} \rho |\boldsymbol{v}| \text{d}V \tag{4.7}$$

The time dependent total flux of neutrino momentum through the sphere at R_{gain} is given by $c^{-1} E_\nu$, where

$$\dot{E}_\nu(t) = \oint_{r=R_{\text{gain}}} F_\nu \, \text{d}S \,. \tag{4.8}$$

This allows us to define the instantaneous neutrino emission anisotropy parameter as

$$\widetilde{\alpha}_\nu(t) = c \, \frac{|\dot{\boldsymbol{P}}_\nu(t)|}{\dot{E}_\nu(t)} \,. \tag{4.9}$$

In analogy to the ejecta momentum, the momentum radiated by neutrinos is

$$\frac{1}{c} E_\nu(t) = \frac{1}{c} \int_0^t \oint_{r=R_{\text{gain}}} F_\nu \, \text{d}S \text{d}t' \tag{4.10}$$

so that the integral neutrino emission asymmetry at time t becomes

$$\alpha_\nu(t) = c \, \frac{|\boldsymbol{P}_\nu(t)|}{E_\nu(t)} \,. \tag{4.11}$$

In addition, we compute the NS spin by integrating the flux of angular momentum through a sphere of radius $r_0 = 100\,\text{km}$ around the origin,

$$\frac{\text{d}\boldsymbol{J}_{\text{NS}}}{\text{dt}} = r_0^2 \int_{4\pi} \rho v_r \boldsymbol{r} \times \boldsymbol{v} \text{d}\Omega, \tag{4.12}$$

where ρ is the density, $\boldsymbol{v}$ and $\boldsymbol{r}$ are the vector valued velocity and position and v_r the radial velocity.

In order to estimate the spin period $P_{\text{NS}} = 2\pi I_{\text{NS}}/|J_{\text{NS}}|$ of the neutron star, with I_{NS} being the moment of inertia of the PNS, we use the approximation by Lattimer and Schutz (2004)

$$\begin{aligned} I_{\text{NS}} &= 0.237 M_{\text{g}} R_{\text{NS}}^2 \left[1 + 4.2A + 90A^4\right], \tag{4.13} \\ A &= M_{\text{g,M}_\odot} R_{\text{NS,km}}^{-1}, \end{aligned}$$

where $M_{\mathrm{g,M_\odot}}$ is the gravitational mass of the PNS in units of $\mathrm{M_\odot}$, and $R_{\mathrm{NS,km}}$ is the radius of the PNS in units of km. In the above equation the gravitational mass M_{g} can be estimated from the baryonic mass M_{b} as (Lattimer and Prakash, 2000)

$$M_{\mathrm{g}} = M_{\mathrm{b}} - \frac{0.6\beta}{1 - 0.5\beta} M_{\mathrm{g}}, \tag{4.14}$$

where $\beta = GM_{\mathrm{g}}/R_{\mathrm{NS}}c^2$ and $M_{\mathrm{b,M_\odot}}$ is the baryonic mass of the PNS in solar masses.

In Table 4.2 we provide properties of the PNS resulting from our post-bounce simulations. We list the PNS kick velocity (v_{NS}), anisotropy parameter (α_{ej}), angular momentum (J_{NS}) and spin period (P_{NS}) along with the PNS radius (R_{ns}) and baryonic PNS mass (M_{b}) at the point in time when we terminate the post-bounce simulations which include neutrino transport or neutrino heating (see also Table 5.1). The PNS radius R_{ns} is defined as the angle-dependent radius where the density drops below $10^{11}\,\mathrm{g/cm^3}$. The PNS mass M_{b} is the mass contained interior to R_{ns}. M_{map} is the mass contained within our inner grid boundary, and thus removed from the hydrodynamic grid at the start of the long-time simulations (see Table 5.1). M_{g} the corresponding gravitational mass. We also list the total angular momentum J_{NS} of the PNS and the angle θ_{vJ} between the total kick velocity $\boldsymbol{v}$ and the direction of the angular momentum vector $\boldsymbol{J}$.

The almost spherical explosions of the ECSN-like progenitors yield very low hydrodynamic kick velocities (in agreement with Gessner and Janka 2018). Anisotropic neutrino emission cannot be evaluated in the simulation of model e8.8, because of the spherical treatment of the central PNS region. The contribution of anisotropic neutrino emission in model s9.0 is of comparable size as the contribution due to aspherical ejection of matter and even exceeds the hydrodynamic contribution in model z9.6. LESA manifests itself in a dominant and stable spherical harmonics $\ell = 1$ mode of the lepton-number emission and a corresponding energy-emission dipole of several percent amplitude compared to the monopole (see Tamborra et al. 2014; Tamborra et al. 2014). LESA is observed in both simulations conducted with VERTEX-PROMETHEUS.

We show in Figure 4.3 planar slices of the electron fraction (left panels) and entropy per nucleon (right panels) of the iron core progenitors. The black, blue and green arrows indicate the total, hydrodynamic and neutrino-induced directions of the PNS kick. In case of model z9.6 the hydrodynamic and neutrino-induced kicks are clearly aligned. This results from the anti-correlation of the LESA lepton-number emission dipole and the direction of the maximum $\nu_{\mathrm{e}} + \bar{\nu}_{\mathrm{e}}$ as well as total neutrino luminosity (Tamborra et al., 2014). Increased heating by $\nu_{\mathrm{e}} + \bar{\nu}_{\mathrm{e}}$ absorption in the postshock region in the hemisphere opposite to the LESA dipole pushes the supernova shock to larger radii. The induced asymmetry of

the post-shock ejecta leads to the hydrodynamic acceleration of the PNS in the opposite direction due to the gravitational pull of the slower ejecta. The neutrino-induced NS kick acts in the same direction, i.e., nearly aligned with the LESA dipole, because of the maximum total neutrino luminosity in the anti-LESA direction.

Due to the weak convection in model z9.6, the neutrino emission asymmetry is the dominant contribution to drive the PNS kick. While the gravitational tug of the ejecta can only account for $v_{\mathrm{NS}}^{\mathrm{hyd}} \sim 10\,\mathrm{km/s}$, the asymmetric emission of neutrinos alone would enable a kick velocity of $v_{\mathrm{NS}}^{\nu} \sim 25\,\mathrm{km/s}$. The total kick sums up to $v_{\mathrm{NS}}^{\mathrm{tot}} = 35\,\mathrm{km/s}$. A correlation or even alignment of the neutrino-induced and hydrodynamic kick is less clear in model s9.0. The asymmetric neutrino energy emission is also responsible for a sizeable contribution to the PNS kick in this case, and even for the dominant contribution during the first 500 ms after bounce. However, the neutrino-induced kick is not closely aligned with the LESA kick as in model z9.6, although also in model s9.0 it is the same hemisphere as the LESA dipole direction. The hydrodynamic PNS kick, however, is in the opposite hemisphere, different from the case of model z9.6. Both this different orientation of the hydrodynamic kick relative to the LESA dipole, and the misalignment of LESA direction and neutrino-induced kick in model s9.0 are a consequence of the fact that hydrodynamic instabilities in the postshock layer are much more violent and corresponding asymmetries of the mass distribution much stronger than in model z9.6.

The neutrino heating asymmetry associated with LESA (with more heating in the anti-LESA direction) is not powerful enough to determine the morphology of the postshock flow in this model. The shock expansion and explosion are weaker in the anti-LESA direction, where convective downdrafts towards the PNS are numerous and massive and thus determine the hydrodynamic PNS kick in this direction (blue arrows in the lower panels of Figure 4.3). Accretion-associated asymmetries of the total neutrino luminosity are also the reason why the neutrino-induced kick is not well aligned with the LESA lepton-emission dipole. The luminosity maximum and the electron-number emission maximum are not anti-parallel in model s9.0. The combined hydrodynamic and neutrino-induced kicks in model s9.0 lead to a PNS velocity of $\sim 41\,\mathrm{km/s}$ at mapping time t_{map}. It must be emphasized that in both models, z9.6 and s9.0, the Vertex-Prometheus neutrino transport was switched off at about 0.41 s and 0.49 s after core bounce, respectively. At this time the neutrino-induced kicks have not reached their final values, which will be higher than the numbers presented in Table 4.2.
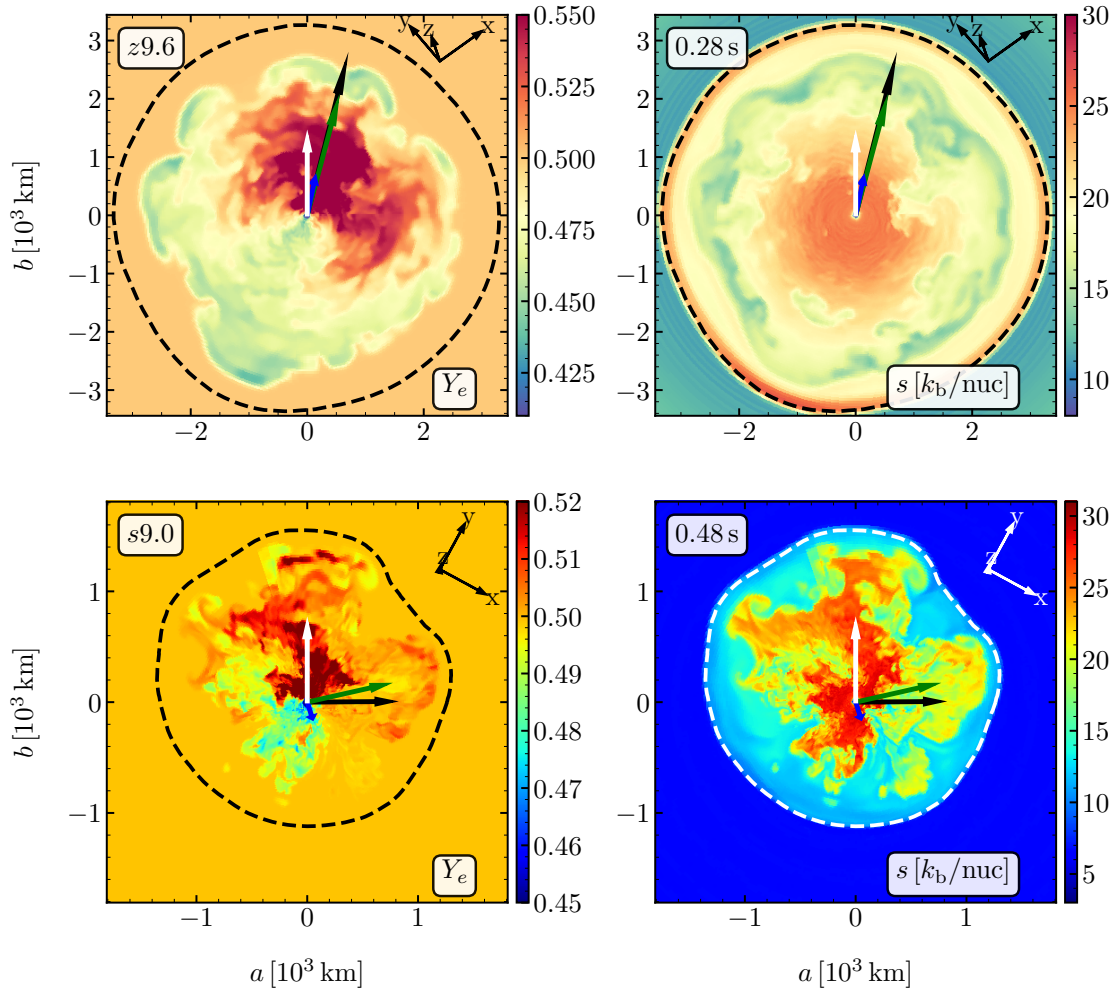
Fig. 4.3 Planar slices of the electron fraction Y_e (left panels) and entropy per nucleon (right panels) of models z9.6 and s9.0 at 0.28 s and 0.49 s after bounce, respectively. We choose times where the LESA dipole is strong in both models. The planes are chosen such that the LESA dipole direction (white arrow) is pointing to the north and are not aligned with the global coordinate system. The arrows indicate the directions of the (instantaneous) total PNS kick (black), the hydrodynamic PNS and neutrino kick of the PNS (blue and green, respectively). The black or white dashed line marks the shock radius and the tripods give the global orientation. Note that in model z9.6 the blue and green arrows are nearly aligned, adding up to the black arrow.

4.2.2 Elemental production and distribution shortly after shock revival

Due to the small α network in combination with a simplified neutrino transport scheme in PROMETHEUS-HOTB and the simple flashing scheme in VERTEX-PROMETHEUS we can only give rough estimates on the nucleosynthesis in our models. However, in order to understand outward/inward mixing of heavy/light elements in later stages of the evolution it is instructive to look at the total yields and the distribution of the elements in velocity space. In Table 4.3 we list the total masses of selected elements for our 3D models at t_{map}. Values in brackets show the mass of the respective element within the shock radius. Note that in the simulations with VERTEX-PROMETHEUS free protons (p) are allowed in the postshock matter whereas in the simulation with PROMETHEUS-HOTB they are recombined with free neutrons to ^{4}He.

As our models have only explosion energies of the order of $\sim 10^{50}$ erg, only very little amounts of ^{56}Ni ($M_{\mathrm{Ni}} \sim 10^{-(4...3)}\,\mathrm{M}_\odot$) are produced. Note that the amount of Tr produced is significantly higher in model e8.8 which is partly attributed to the simplified neutrino transport scheme.

In order to assess the strength of mixing during the first second in our 3D models, we present in Figure 4.4 normalized mass distribution of selected elements behind the shock radius as functions of velocity (top panels) and mass coordinate (lower panels). For sampling the velocity space, we chose 50 bins between the maximal and minimal velocities within the considered region. We use 30 bins to sample the distribution in the mass coordinate. The total masses on the grid at the time when we map our simulations onto the new computational grid are listed in Table 4.3, whereas the binding energy ahead of the shock is listed in Table 4.4.

The quasi-spherical explosion of model e8.8 manifests itself also in the distribution of elements over mass and velocity space, where the initial shell structure of the progenitor is essentially preserved. Most material of the thin carbon shell of the progenitor travel with $\gtrsim 30,000 - 70,000\,\mathrm{km/s}$ ahead of the outer mass shells of the former ONeMg core, which travel with up to $\sim 60,000\,\mathrm{km/s}$. Most of the newly synthesized iron-group and α nuclei expand with velocities below $\sim 30,000\,\mathrm{km/s}$. Inefficient mixing also confines the neutrino-heated ejecta within $M(r) \leq 1.338\,\mathrm{M}_\odot$.

Slightly more violent convection in the z9.6 model leads to more efficient mixing in mass and velocity space (see middle panels of Figure 4.4). Some neutrino-heated material could already be mixed into the carbon and oxygen shells and travels at more than $\gtrsim 20,000\,\mathrm{km/s}$. The bulk of the metal-rich ejecta still expand with slower velocities, however. Similar to model e8.8, the deceleration of the forward shock at the CO/He interface in model z9.6 also compressed some of the ejecta into a dense shell. Model s9.0, again, differs strongly

Table 4.3 Total masses of elements M_i of the pre-collapse progenitor models as shown in Figure 2.1 (top) and behind the shock front in our 3D simulations at mapping time t_{map} as well as binding energies ahead of the shock.

Species	Progenitor $M_i [M_\odot]$		
	e8.8	z9.6	s9.0
H	2.68	5.10	4.54
^{4}He	1.79	3.11	2.68
^{12}C	2.71×10^{-2}	2.24×10^{-2}	3.37×10^{-2}
^{16}O ^{20}Ne ^{24}Mg	0.94	0.04	0.13
^{28}Si	3.98×10^{-3}	2.32×10^{-2}	1.34×10^{-2}
Iron-group (NSE)	0.39	1.30	1.32

Species	Postshock ejecta at t_{map}		
n	-	4.25×10^{-5}	8.22×10^{-8}
p	-	4.64×10^{-4}	7.27×10^{-5}
H	1.97×10^{-7}	0	0
^{4}He	4.90×10^{-3}	8.24×10^{-3}	5.48×10^{-5}
^{12}C	4.08×10^{-5}	1.52×10^{-3}	3.25×10^{-3}
^{16}O ^{20}Ne ^{24}Mg	1.00×10^{-4}	2.20×10^{-3}	4.13×10^{-2}
^{28}Si	1.63×10^{-5}	2.27×10^{-4}	1.29×10^{-3}
^{56}Ni	1.05×10^{-3}	6.50×10^{-4}	4.72×10^{-3}
Tr	6.69×10^{-3}	1.05×10^{-3}	1.06×10^{-6}

Notes: The top table shows the total mass of selected elements in the pre-collapse models. The bottom table lists the total masses behind the shock in 3D simulations at t_{map}. n and p label free neutrons and protons, respectively, left after the freeze-out from NSE, whereas H labels hydrogen from the envelope. Since the onset of the explosion of model e8.8 was simulated with Prometheus-HOTB no free protons remain in the ejecta. The high mass of ^{4}He compared to ^{56}Ni and Tr in model z9.6 is a consequence of the high value of $T_{NSE} \sim 5.8 \times 10^9$ K in this simulation instead of $\sim 4.0 \times 10^9$ K in model s9.0.

Table 4.4 Binding energies ahead of the shock at t_{map} for the 3D simulations.

Model	E_{bind}
	$[10^{47}\,\mathrm{erg}]$
e8.8	-0.56
z9.6	-6.89
s9.0	-9.76

Notes: The table shows the total binding (i.e. internal + kinetic + gravitational) energy $E_{\mathrm{bind}}(r > R_{\mathrm{sh}})$ ahead of the shock at the time of mapping t_{map} for all 3D models.

from the ECSN-like models. Strong and long lasting postshock convection completely erases the initial onion shell structure of the progenitor. Elements are nearly homogenously mixed over mass and velocity coordinates (see right panels of Figure 4.4). The fastest neutrino-heated ejecta are associated with a large high entropy plume inducing a dipolar asymmetry of the shock wave, which can be see in Figure 4.2.
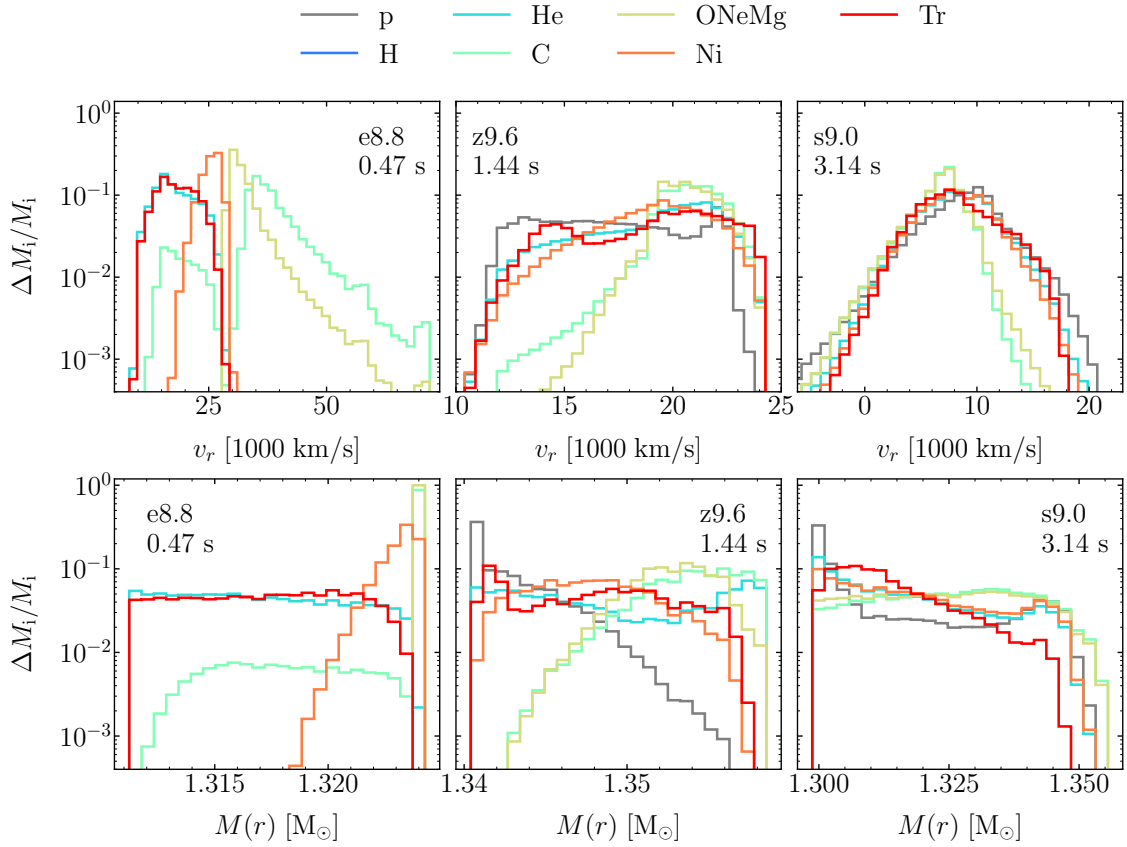
Fig. 4.4 Normalized mass distributions of chemical elements as functions of radial velocity (top panels) and enclosed mass (bottom panels) for all the postshock material in our 3D models at t_{map} (see Table 5.1). We use 50 bins in velocity space and 30 bins in the mass coordinate. The normalization is performed with the masses given in Table 4.3. The mass coordinate in the 3D models is defined by mass enclosed by given radius.

4.2.3 Two-dimensional Simulations

The overall morphology of the 2D and 3D simulation of model e8.8$_{10}$ is very similar as can be inferred from Figure 4.5, where we show slices of the entropy at the indicated times.
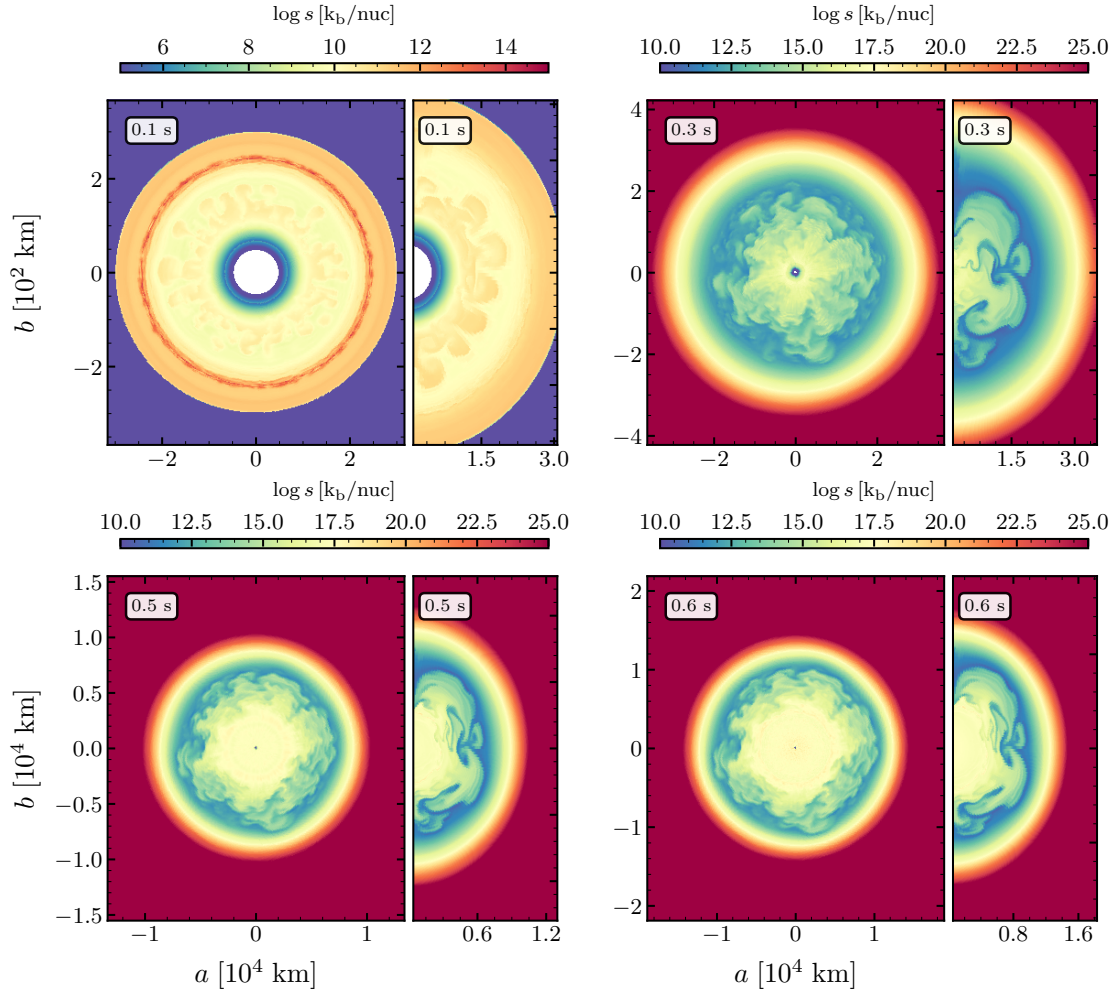
Fig. 4.5 Slices of the 2D (right side of panels) and 3D (left side of panels) simulations of model e8.8 showing the entropy per nucleon at the indicated times. At $t_{\mathrm{pb}} \gtrsim 0.3\,\mathrm{s}$ the forward shock is beyond the plot boundaries. The high entropy plumes in the post-shock regime have similar sizes, where in the 3D model, some small scale structures are superimposed on the larger neutrino-heated plumes.

Both simulations develop high entropy plumes of similar sizes. In the 3D simulation, however, these larger structures seem to be superimposed with small scale features at the outermost tips of the plumes. This may be attributed to the "inverse-cascade" in the 2D

simulations, which states that in 2D simulations kinetic energy tends to live on large ℓ modes, whereas in 3D, kinetic energy is dissipated to smaller scales.

However, these small scale structures have no significant impact on the distribution of chemical elements, as can be seen in Figure 4.6. There, we show the mass distributions of our 2D simulations of model e8.8 for all calibrations listed in Table 4.1 at $t_{\mathrm{pb}} = 2.5\,\mathrm{s}$. Naturally, the maximum achieved velocities and the total amount of ejecta scales with the explosion energy, where both are higher for higher energetic models. Due to the almost identical explosion timescales, convection behind the shock leads to similar structures in all 2D simulations. We therefore find almost identical mass distributions for the 2D simulations, where higher energetic models show a slightly higher efficiency to mix neutrino-heated matter to larger mass coordinates.

Differences to the 3D simulation are small as well, where the 2D models show a tail of low velocity $^{56}\mathrm{Ni}$ which is missing in the 3D case. This may be related to the lower resolution in the 3D simulation.
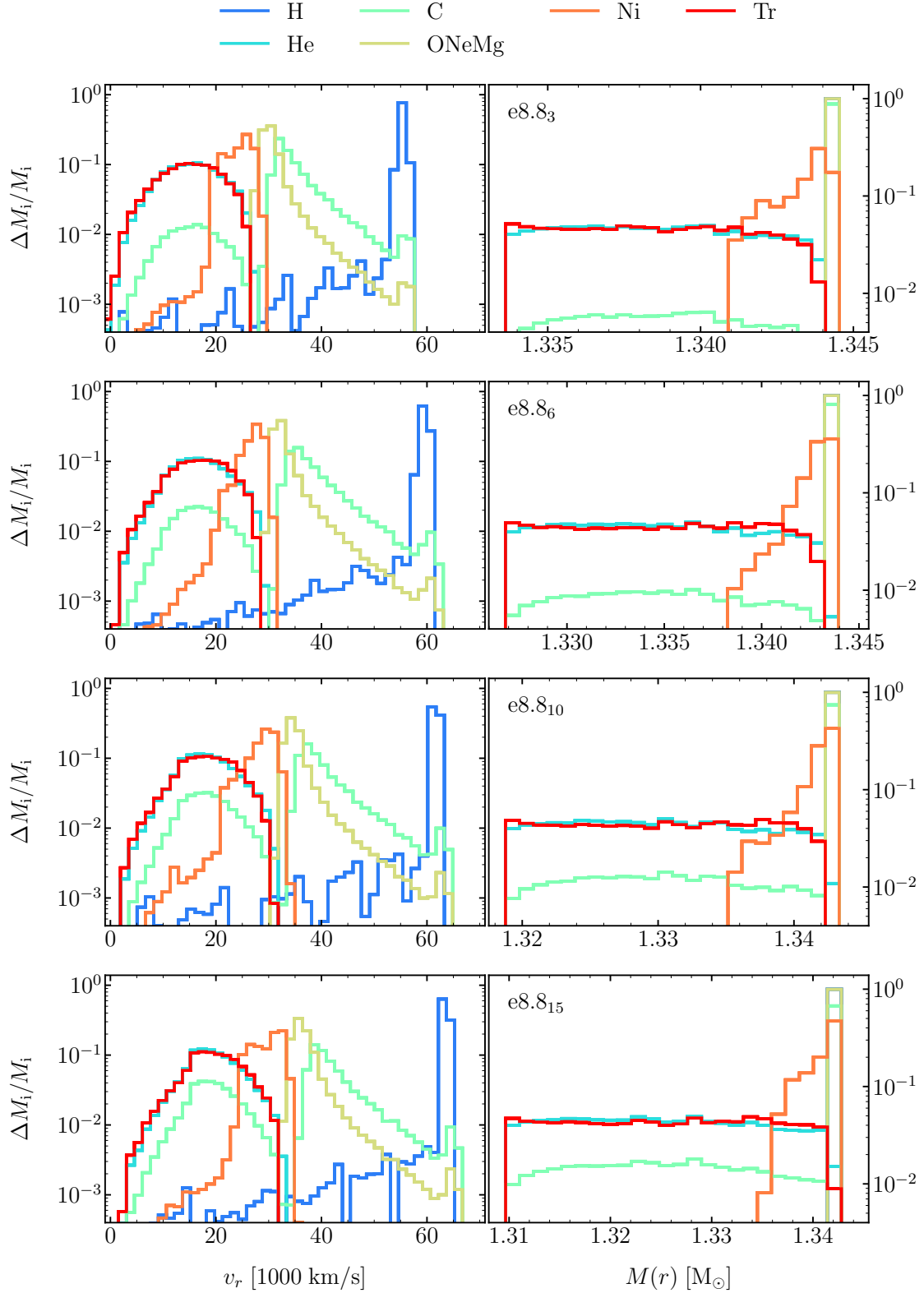
Fig. 4.6 Mass distributions of the 2D simulations of model e8.8 at $t_{pb} = 2.5\,s$. Note the very similar distributions among the different calibrations. Only the maximum velocity and the total mass of unbound ejecta differ and scale with the explosion energy.

Chapter 5

Evolution Beyond Shock-Breakout

In order to capture the dynamics of the ejecta after shock-revival, one needs to continue the simulations described in the previous Chapter on longer timescales, which may extend from a few hours to several days depending on the progenitor structure. This goal is hard to achieve with the currently available computational resources. The grid size required to resolve the neutron star and the hydrodynamical instabilities that will emerge in the ejecta (some hundreds of thousand kilometers above the PNS) is not feasible. Therefore, in order to determine the long-time evolution of the models, we exclude the neutron star and its immediate surroundings from our calculations and replace it by a point mass and a suitable boundary in our simulations. To aid us with the interpretation of the multi-dimensional simulations, we appeal to 1D spherically symmetrical simulations, with the same physics. We use these simulations to study 1) the propagation of the forward shock, 2) the points in time when it passes composition-interfaces, and 3) when and how the reverse shock forms and reaches the PNS.

In the following we discuss the numerical and physical setup of our long-time simulations. We then present the propagation of the shock of our one dimensional simulations and estimate the occurrence and strength of possible hydrodynamical instabilities like the RT instability. Thereafter we analyze the results of our multi-dimensional simulations focusing on the morphology of the neutrino-heated ejecta and the mixing processes that take place as the ejecta travel through the stellar envelope.

5.1 Numerical Setup for the Long-time Simulations

In the following, we describe the numerical setup which is used the long-time simulations computed with PROMETHEUS-HOTB. Similar to the setup during the onset of explosion,

Table 5.1 Initial positions of our inner and outer grid boundaries and mapping times t_{map} in seconds after bounce for our long-time simulations.

Model	Dim.	R_{ib} [km]	R_{ob} [km]	M_{map} [M$_\odot$]	t_{map} [s]
e8.8$_3$	2D	1000	8.4×10^8	1.334	2.515
e8.8$_6$	2D	1000	8.4×10^8	1.327	2.515
e8.8$_{10}$	2D	1000	8.4×10^8	1.319	2.515
e8.8$_{15}$	2D	1000	8.4×10^8	1.309	2.515
e8.8	3D	500	8.4×10^8	1.326	0.470
z9.6	3D	600	1.5×10^8	1.340	1.440
s9.0	3D	1000	2.9×10^8	1.351	3.140

gravity is treated by a 1D potential with general-relativistic corrections. We also follow nuclear reactions with the 13-species α-network. However, in order to continue the simulations to such large timescales, the initial data from the simulations until shock revival need to be mapped onto a new computational domain within PROMETHEUS-HOTB. The details of the mapping procedure are given in the following section.

5.1.1 Computational Grid and Mapping Procedure

We map the final state of the post-bounce simulations conducted with PROMETHEUS-HOTB and VERTEX-PROMETHEUS onto a new computational domain by excising the PNS and the subsonic outflows in its vicinity. In Table 5.1 we list the time of mapping and the inner and outer boundaries of the new computational grid. The mass contained within the inner boundary R_{ib} (M_{map}) is treated as a point mass[1]

The multi-dimensional long-time simulations are conducted with an angular resolution of 2°. We use a non-equidistant (geometrically increasing from the inner to the outer boundary) radial grid adjusting the number of radial grid cells to achieve a resolution better that 0.1%. In order to guarantee sufficient resolution where needed, the radial grid is allowed to move with the ejecta starting from $t_{pb} \approx 10\,s$.

This enables us to better resolve the post-shock material as it propagates through the envelope, to reduce numerical diffusion of the species and to relax the CFL criterion. We find the radius R_{max} of the cell with the fastest ejecta (v_{max}). For cells with $R_{cell} < R_{max}$

---

[1]We ensure that matter at radii smaller than R_{ib} has velocities smaller than the local escape velocity and will thus eventually contribute the to final NS mass.

and positive radial velocity, the cell velocity is defined as

$$v_{\text{cell}} = a \frac{v_{\max}}{R_{\max}} \cdot R_{\text{cell}}, \tag{5.1}$$

where a is an adjustable parameter and R_{cell} the radius of the cell center. Outside the shock the grid velocity follows a power law to prevent sharp jumps in resolution. Figure 5.1 shows an example configuration of the moving grid. Additionally, we excise the innermost cells of the computational domain, when matter within this cell is free falling with supersonic velocities and the new radius of the boundary fulfills $R_{\text{ib}} \leq 0.5\% \, R_{\text{sh}}$.
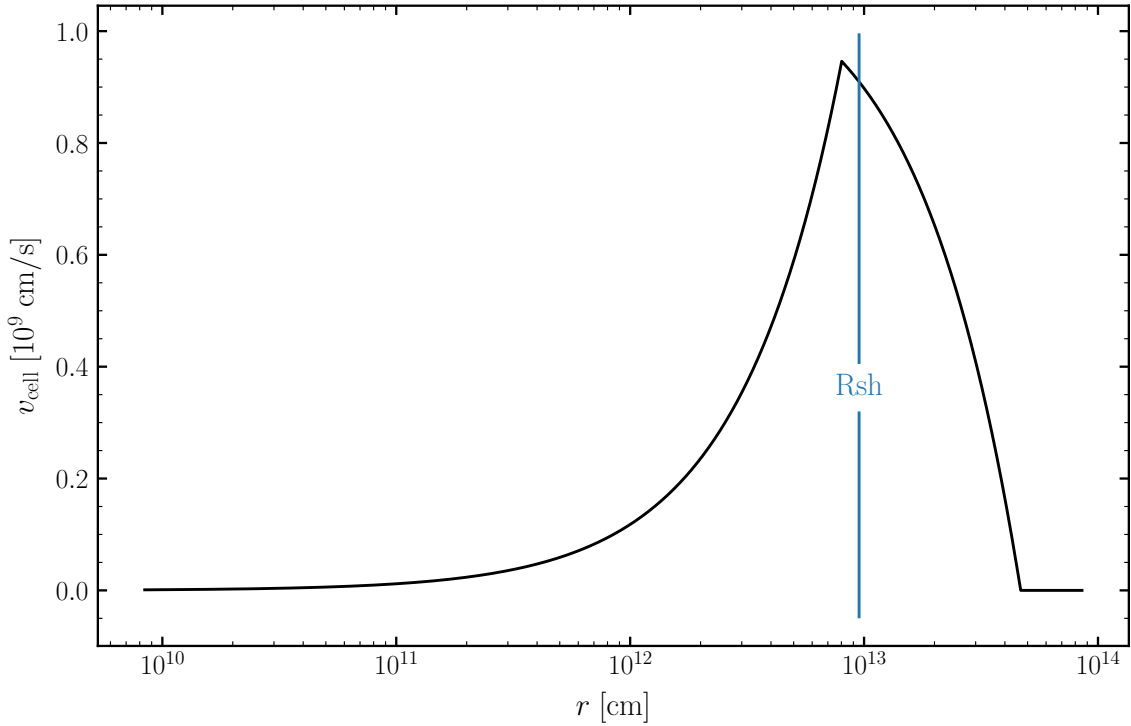
Fig. 5.1 Grid velocity of the radial grid as defined in Equation (5.1). The vertical line shows the shock radius of this snapshot of the 2D $e8.8_{10}$ long-time simulation at $t_{\text{pb}} = 1.4 \, \text{h}$

When mapping the iron core models into PROMETHEUS-HOTB, we recombine free n and p from the freeze-out of NSE into ^{4}He under the condition of charge conservation and account for the energy release. Moreover, we combine all neutron-rich nuclei formed in neutrino-heated ejecta into tracer (Tr) material.

5.1.2 Inner Boundary Condition

When mapping from the simulations of the onset of explosion to the follow-up simulation, the central region interior to R_{ib} of Table 5.1 is removed from the computational domain. Similar to Wongwathanarat et al. (2015) we prescribe an inflow boundary condition at R_{ib}, which corresponds to the neutrino-driven baryonic mass-loss ("neutrino-wind"; e.g Qian and Woosley 1996) generated by ongoing neutrino-energy deposition in the surface layers of the cooling PNS. In contrast to Wongwathanarat et al. (2015), we employ neutrino-wind results adopted from 1D simulations of the explosions, seamlessly connected to the full multi-dimensional explosion simulation by choosing R_{ib} to be in the supersonic wind region (ensuring that perturbations cannot propagate back to the inner boundary creating artifacts) and by applying the wind data at times where the outflow properties match between the 1D and multi-dimensional models. This is possible because the neutron stars in all 1D and multi-dimensional models are extremely similar and the neutrino-emission and thus the neutrino-driven winds also have very similar properties. For both iron core progenitors we employ neutrino wind conditions of a 1D simulation of model z9.6 with the VERTEX-PROMETHEUS code. It includes PNS convection by a mixing-length treatment, for which reason the neutrino-emission is essentially identical to the multi-dimensional calculation (Mirizzi et al., 2016). The time dependence of the radial velocity v_r, density ρ and total (i.e. kinetic + internal) energy density e, which are needed for setting the boundary condition, are shown in Figure 5.2 as extracted from the 1D explosion simulation of the z9.6 model at a radius of 600 km (in the supersonic wind domain). For the 3D simulation of model e8.8 we use the neutrino-wind results at 500 km from the corresponding 1D run with the same explosion energy. Using time dependences of the boundary conditions normalized by the initial value at the mapping time t_{map} guarantees a smooth, seamless transition from the earlier evolution to the long-time evolution of the explosion. Transient artifacts are thus kept minimal.

Due to continuous non-radial motions in the post-bounce simulation of model s9.0, the simulations had to be continued to $t_{\mathrm{pb}} = 3.14\,\mathrm{s}$. At this time the neutrino-driven wind was already very weak, because of which we did not include it in the long-time simulation of this model.
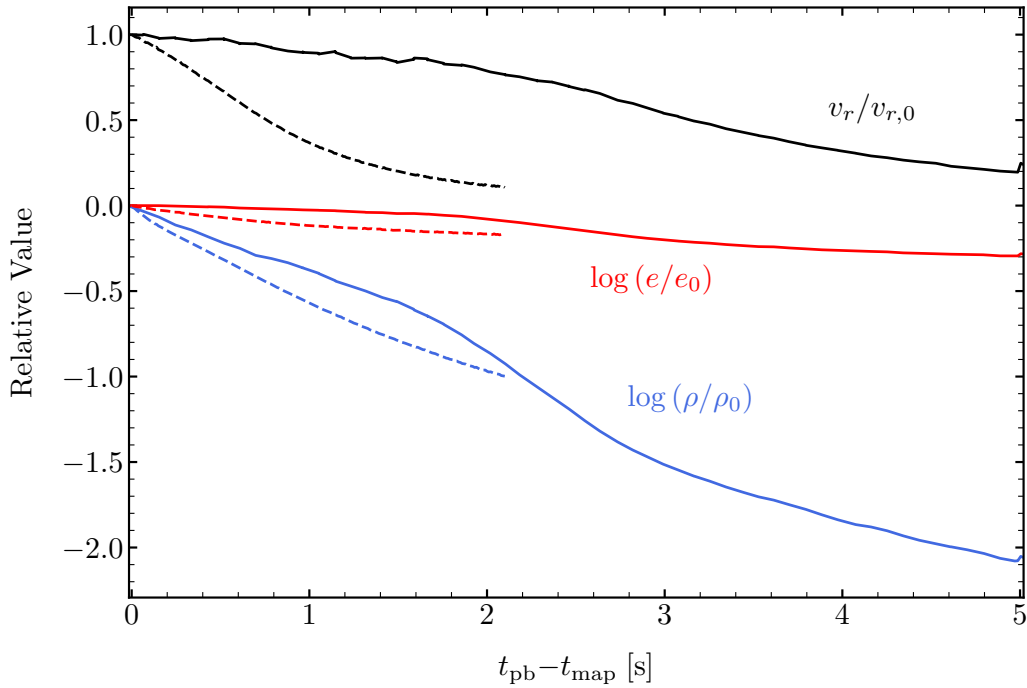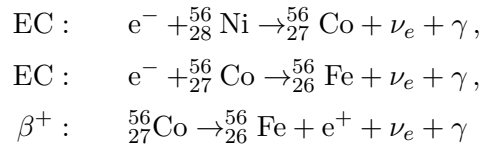
Fig. 5.2 Time-dependent behavior of neutrino-wind density ρ, radial velocity v_r and the total energy density e, normalized to their initial values at t_{map} (see Table 5.1), which defines the start of the long-time simulations of model e8.8 and z9.6. The data for model z9.6 are extracted from a 1D simulation of the explosion of the $9.6\,\mathrm{M}_\odot$ progenitor with Vertex-Prometheus (see Mirizzi et al. 2016), evaluated at a radius of 600 km (solid lines). For model e8.8 we use data of the respective 1D simulation with Prometheus-HOTB (dashed lines).

5.1.3 β-Decay

During the explosion of massive stars, a few tens of a solar masses of radioactive ^{56}Ni and other elements are produced. This radioactivity powers the light curves of supernova transients. To follow in the energy input by radioactive ^{56}Ni decay we add ^{56}Co and ^{56}Fe to our set of nuclei. ^{56}Ni (half-life $t_{1/2} = 6.077\,\mathrm{d}$) decays to ^{56}Co via electron capture (EC) decay. The resulting ^{56}Co nucleus is unstable ($t_{1/2} = 77.27\,\mathrm{d}$) and decays to ^{56}Fe by electron capture decay or positron decay (β^+). We thus add ^{56}Co and ^{56}Fe to our set of nuclei. The respective decay reactions are given by

$$\mathrm{EC}: \quad \mathrm{e}^- + {}^{56}_{28}\mathrm{Ni} \rightarrow {}^{56}_{27}\mathrm{Co} + \nu_e + \gamma\,,$$

$$\mathrm{EC}: \quad \mathrm{e}^- + {}^{56}_{27}\mathrm{Co} \rightarrow {}^{56}_{26}\mathrm{Fe} + \nu_e + \gamma\,,$$

$$\beta^+: \quad {}^{56}_{27}\mathrm{Co} \rightarrow {}^{56}_{26}\mathrm{Fe} + \mathrm{e}^+ + \nu_e + \gamma$$

The above reactions provide an energy source for the surrounding plasma in the form of gamma radiation (E_γ) and kinetic energy ($E_{\mathrm{kin,e+}}$) of the positrons that are produced in the β^+ decay. We include the annihilation energy of the positrons (E_{rec}) in the energy of the gamma's. The produced neutrinos escape freely. The average energy available (including the kinetic energy of the positron in the cobalt decay) per decay is $E_{\gamma,\mathrm{Ni}} = 1.72\,\mathrm{MeV}$, $E_{\gamma,\mathrm{Co}} = 3.735\,\mathrm{MeV}$ (Nadyozhin, 1994). A fraction of the γ's may escape depending on the optical depth $\tau(r)$ of the gas, which is defined as

$$\tau(r) = -\int_{R_*}^{r} \kappa_\gamma Y_\mathrm{e}(r')\rho(r')\,\mathrm{d}r', \tag{5.2}$$

where R_* is the radius of the stellar surface, Y_e the electron fraction and κ_γ is the optical opacity. Assuming Compton-scattering is the dominant opacity source, we adopt a constant value of $\kappa_\gamma = 6.0 \times 10^{-2}\,\mathrm{cm^2\,g^{-1}}$ (Swartz et al., 1995). Therefore, the energy per mass $\Delta E_i/\Delta M$ deposited by each species i, with mass fraction X_i and nuclear mass m_i into the surrounding plasma during a time step Δt is given by

$$\frac{\Delta E_\mathrm{i}}{\Delta M} = \frac{\Delta X_i}{m_i}\left[E_\gamma\left(1 - e^{-\tau(r)}\right) + E_{\mathrm{kin,e+}}\right], \tag{5.3}$$

where $\Delta X_i = \left(1 - e^{-\Delta t/t_{0,i}}\right)$ is the change of X_i during Δt with $t_{0,i}$ being the life-time of species i, and $E_{\mathrm{kin,e+}}$ is the kinetic energy of the positron in the cobalt decay. The energy is deposited locally and thermodynamic quantities are self-consistently updated.

5.2 Spherically-Symmetric Simulations and Linear Stability Analysis

In order to aid us with the interpretation of our three-dimensional simulations, we appeal to 1D long-time simulations which are started from angle-averaged initial states of the 3D explosion models at the same times as given in Table 5.1. The numerical and physical setup for the spherically symmetric simulations remains unchanged. They can teach us about the behavior of the shock, while it propagates through the envelope. Note that we use the e8.8$_{10}$ calibration as the reference case for the long-time evolution of the ECSN and refer to this model in the following analysis unless otherwise noted.

5.2.1   Rayleigh-Taylor Instability

The Rayleigh-Taylor instability is a hydrodynamic instability at the interface between liquids or gases of different densities. A pressure gradient acts such that the heavier matter is accelerated towards the lighter one. An exemplary configuration is shown in Figure 5.3.
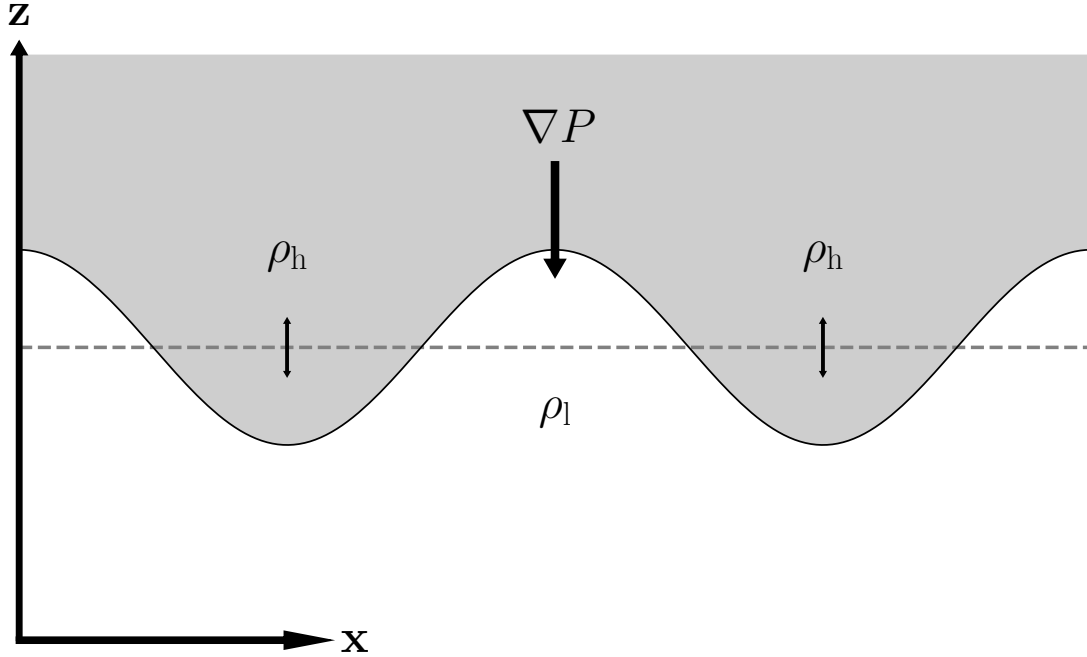

Fig. 5.3 Example configuration of a Rayleigh-Taylor unstable interface. The heavier liquid (gray area, ρ_{h}) sits on top of a lighter fluid (white area, ρ_{l}) and is under an accelerating force $\nabla \boldsymbol{P}$. When the initial interface (dashed line) is disturbed (solid line and border of gray area) the RT instability can grow.

Disturbing the interface gives rise to the growth of the RT instability. Following Chandrasekhar, we define $\rho + \delta\rho$ to be the actual density at any point (x, y, z) as a result of the disturbance and $\delta\rho$ to be the density increment. u_i $(i = 1, 2, 3)$ are the (small amplitude) components of the velocity. The governing equation is linearized continuity equation in planar geometry as given by

$$\rho \frac{\partial u_i}{\partial t} = -\frac{\partial}{\partial x_i}\delta p - g\delta\rho, \tag{5.4}$$

where δp, g are the pressure variation and the acceleration, respectively. Note that we drop the viscous stress tensor of the continuity equation for simplicity. Analyzing the disturbance into normal modes, we seek solutions of the form

$$f(x, y, t) = e^{ik_x x + ik_y y + nt}, \tag{5.5}$$

where k_x and k_y are the constant wavenumbers, $k = k_x^2 + k_y^2$ and n is a constant. Using Equation (5.5) and Equation (5.4) we find, again in the inviscid case,

$$\frac{\partial}{\partial z}\left(\rho \frac{\partial}{\partial z} w\right) - \rho k^2 w = -\frac{k^2}{n^2} g\left(\frac{\partial}{\partial z}\rho\right) w, \tag{5.6}$$

where w is the z component of the velocity. Considering two uniform fluids of densities ρ_1 and ρ_2 separated by a horizontal boundary at $z = 0$ and omitting surface tension effects Equation (5.6) simplifies to

$$\left(\frac{\partial^2}{\partial z^2} - k^2\right) w = 0. \tag{5.7}$$

The general solution of Equation 5.7 is

$$w = Ae^{kz} + Be^{-kz} \tag{5.8}$$

Since w has to vanish for $z \to \pm\infty$ we must suppose

$$w_1 = Ae^{kz} \ (z < 0) \tag{5.9}$$

and

$$w_2 = Ae^{-kz} \ (z > 0), \tag{5.10}$$

where we choose the same constant A for $z > 0$ and $z < 0$ as the solutions to Equation (5.7) have to be continuous at the boundary between ρ_1 and ρ_2. Also, under the constraint of continuity at the interface (see Chandrasekhar 1961, Chapter 10, Equation 41), the growth rate of small perturbations is found to be

$$n^2 = gk\left(\frac{\rho_h - \rho_l}{\rho_h + \rho_l}\right) \tag{5.11}$$

5.2.2 Linear Stability Analysis

As mentioned already, the velocity of the forward shock depends on the progenitor structure, in particular the ρr^3-profile. According to Sedov et al. (1961) and as shown above one

expects an increase/decrease in the shock velocity when the gradient of the ρr^3-profile is negative/positive. This acceleration and deceleration leads to crossing density and pressure gradients in the post-shock region, or stated otherwise, the gradients of pressure and density have opposite signs. Thus, perturbations in the matter become unstable to the Rayleigh-Taylor (RT) instability (Rayleigh, 1882; Chevalier and Klein, 1978). As the ρr^3-profiles, and hence the shock speed, vary significantly between the progenitors, growth of RT instabilities will affect the long-time evolution of our models in different ways.

In the context of supernova explosions, Equation (5.11) has only limited validity due to the assumption of planar geometry, however. Bandiera (1984)[2] extended the formalism to the case of supernovae. The growth rate of the RT instability at a specific mass coordinate $M(r)$ in the incompressible case σ_{inc} is given by

$$\sigma_{\mathrm{inc}}(t) = \sqrt{\frac{p}{\rho}\frac{\partial \ln p}{\partial r}\frac{\partial \ln \rho}{\partial r}} \tag{5.12}$$

and in the compressible case is given by

$$\sigma_{\mathrm{c}}(t) = \frac{v_{\mathrm{cs}}}{\gamma}\sqrt{\left(\frac{\partial \ln p}{\partial r}\right)^2 - \gamma\frac{\partial \ln p}{\partial r}\frac{\partial \ln \rho}{\partial r}} \tag{5.13}$$

where the symbols have their usual meaning and v_{cs} is the speed of sound. Note that Equation (5.12) is less restrictive than its incompressible counterpart. Nevertheless, we are interested in the position of maximal growth not in the actual value. Calculating the amplifications factors from e.g. angle-averaged values of multi-dimensional models yields a similar functional form but lower amplitudes (see Müller et al. 2018). For the time-dependent amplification factor ξ/ξ_0 we integrate the compressible/incompressible growth-rate (as given by Equation (5.13)/Equation (5.12)) according to

$$\frac{\xi}{\xi_0}(t) = \exp\left(\int_0^t \sigma_{\mathrm{c,i}}\,\mathrm{d}t'\right) \tag{5.14}$$

giving a lower bound for the actual growth rate (Wongwathanarat et al., 2015). Equation (5.14) enables us to estimate the time and location in mass coordinate, when the fluid becomes unstable to the RT instability. It helps us to estimate the growth of perturbations in the ejecta and thus can give hints at the origin of inward/outward mixing of elements.

Figure 5.4 shows the amplification factors in the incompressible (colored lines) and compressible (gray line) case for our 1D simulations, where significant differences between the models are evident.

---

[2]Bandiera (1984) use the fastest growing mode for their derivation of Equations (5.12) and (5.13)
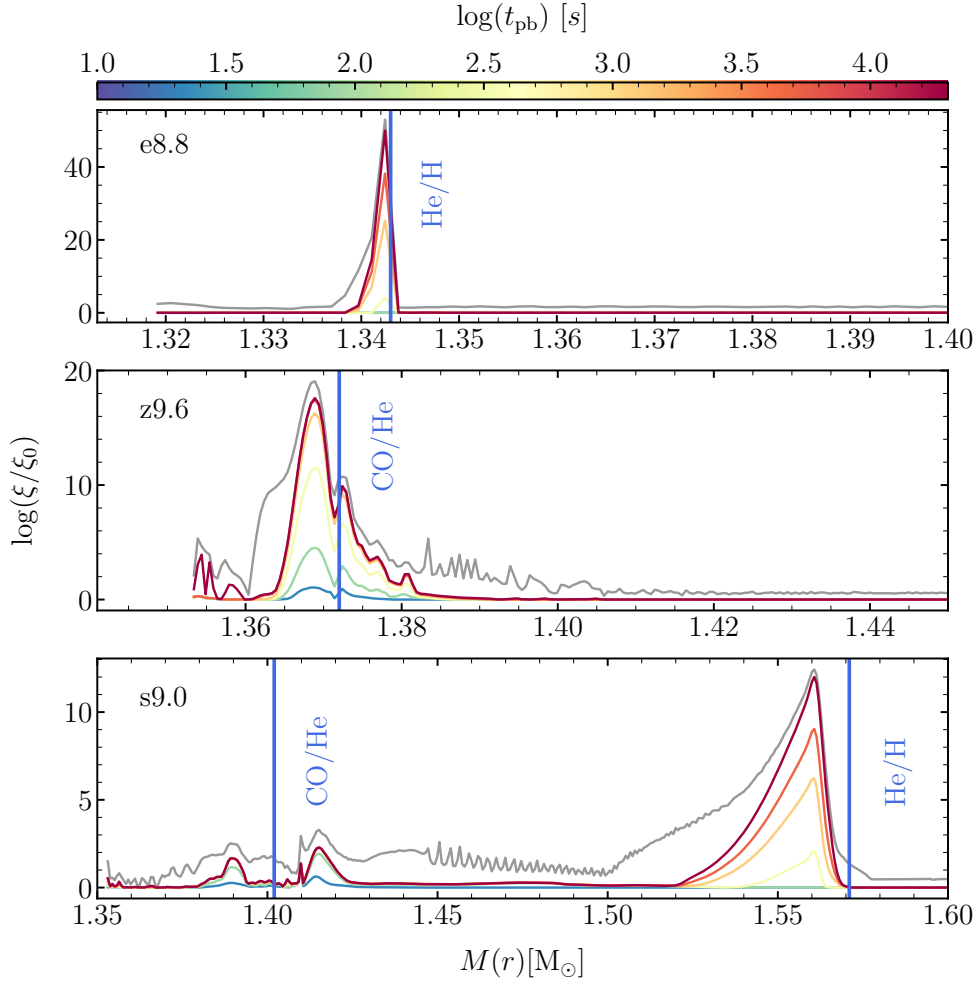
Fig. 5.4 Integrated growth rates for RT instability for all considered models at different times evaluated with Equation (5.14) (colored lines). The different composition interfaces of the progenitors are indicated by vertical blue lines. The gray line denotes the growth factor in the compressible case at $t = 10^4$ s. The different progenitor structures have a large impact on the estimated growth factor as can be seen most prominently by comparing models z9.6 and s9.0. While the ECSN-like progenitors develop only a narrow region of instability around the interface with the steepest density gradient (e.g. He/H for model e8.8 and CO/He for model z9.6), model s9.0 shows two distinct regions of high growth factor around the CO/He and the He/H interfaces.

The top panel of Figure 5.4 shows the integrated growth rate of the 1D e8.8$_{10}$ model. The extreme deceleration of the forward shock when moving into the hydrogen envelope induces very high growth factors at $M(r) \sim 1.34\,\mathrm{M_\odot}$. The ECSN-like structure of model z9.6 is reflected in its amplification factors. Strong deceleration of the forward shock at

the CO/He interface creates the necessary condition for the RT instability to grow. As can be seen in Figure 5.4, the amplification factors at $\sim 1.37 \, M_\odot$ reach high values as observed in the ECSN case. Interestingly, no growth is expected at the He/H interface, which stems from the very small step in the ρr^3-profile at this interface (see Figure 2.2).

Model s9.0 shows striking differences to the models described above. Due to its more shallow ρr^3-profile in the core region and the consequently weaker episodes of shock deceleration and acceleration, the peak amplitudes of the growth factors are smaller. They are, however, of similar magnitude as in the more massive models investigated by Wongwathanarat et al. (2015).

Two distinct regions of instability can be discerned around the CO/He and He/H interfaces. Similar to the red supergiants presented in Wongwathanarat et al. (2015), the strongest contribution arises from the He/H interface followed by the CO/He interface where the amplification factors are about 10 magnitudes lower. While the compressible and incompressible analyses give similar results for models e8.8 and z9.6, the compressible evaluation of the growth factors in model s9.0 predicts additional growth within the He-shell of the star. This is caused by the passage of the reverse shock at later times ($t_{\rm pb} > 3 \times 10^3 \, {\rm s}$). Note that, at this stage, the instability is already in a strongly non-linear phase, where Equation (5.13) loses its validity.

In order to explore the influence of explosion energy on the amplification factors we show in Figure 5.5 the evaluation of Equation 5.14 for all calibrations of model e8.8. We see that the final amplification factors increase with the explosion energy[3]. The reason for this is the steeper pressure gradient behind the shockwave in more energetic models after it passes the He/H interface as the deceleration in the H-envelope is stronger. The RT unstable region remains small in all cases. Therefore, we do not expect large differences in the efficiency of mixing between the models in the long run.

---

[3]The shift in mass coordinate of the peak of the amplification factors is caused by a slight expansion of the outer layers of the He-shell of the star. The supernova shock of models with higher explosion energy reaches the layers earlier, reducing the time available for the shells to expand. This has no influence on the subsequent evolution as only a very small mass is affected.
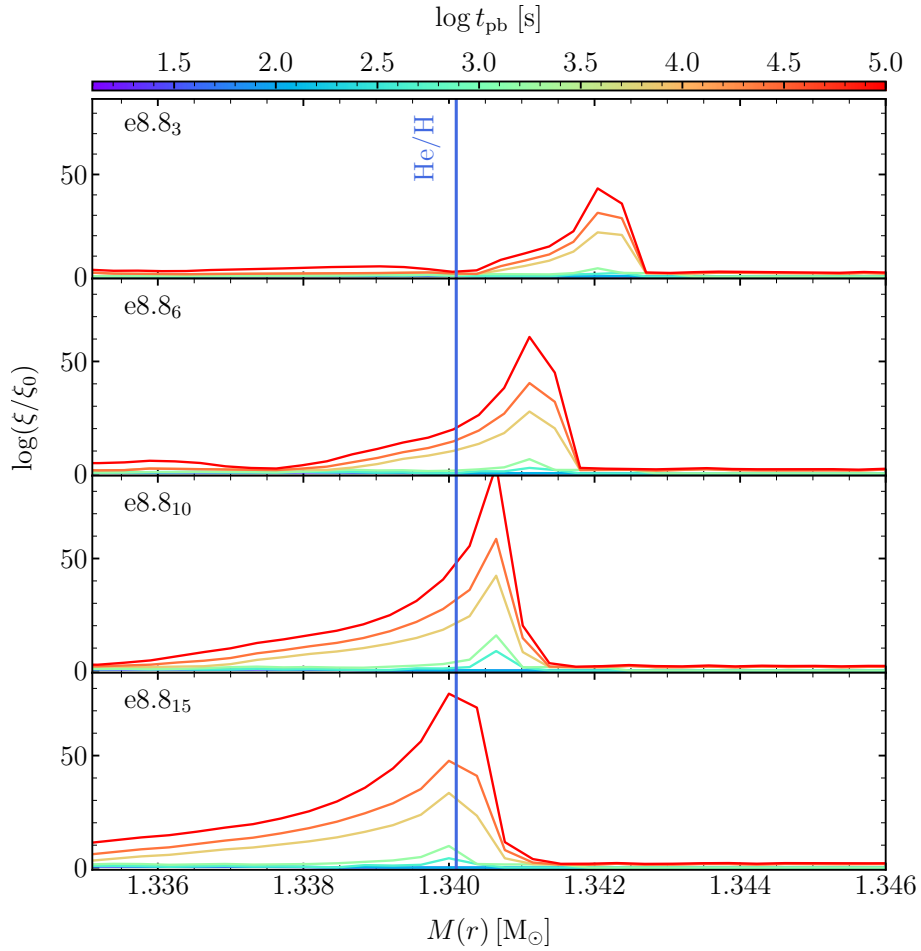
Fig. 5.5 Amplification factors evaluated with Equation (5.14) for all of our calibrated 1D simulations of model e8.8. Models with larger explosion energy clearly show larger amplification factors around the He/H interface which is caused by a steeper pressure gradient behind the shock in the more energetic simulations after it left the core.

5.3 Multi-dimensional Simulations

As has been stated before, 1D simulations are not able to capture the dynamical evolution of the explosion of massive stars as they ignore the growth of non-radial instabilities. To fully understand the asymmetries found in the remnants of past CCSNe, multi-dimensional simulations are necessary. We therefore performed, for the first time, multi-dimensional (2D and 3D) simulations of the long-time evolution of the explosions of low-mass iron-core (z9.6 and s9.0) and ONeMg-core (e8.8) progenitors, started multi-dimensional initial data. Of particular interest is the evolution of the morphology of the neutrino-heated ejecta, which

we trace by the ^{56}Ni + Tr mass fraction, and the evolution of the distribution of elements in mass and velocity space, as these are the quantities accessible to direct observations of supernova remnants.

Note that we do not apply the wind boundary condition to the 2D long-time simulations of model e8.8, as the immediate post-bounce phase was calculated up to $t_{\mathrm{pb}} = 2.515\,\mathrm{s}$. where the neutrino-driven wind is already weak and does not influence the subsequent evolution. We do not include the effect of the neutrino-driven wind in the long-time simulation of model s9.0 because at mapping time $t_{\mathrm{map}} = 3.14\,\mathrm{s}$ it is already very weak and will not influence the subsequent evolution significantly. The starting conditions for the multi-dimensional simulations are summarized in Table 5.1.

5.3.1   Propagation of the Forward Shock

We show in Figure 5.6 the angle-averaged shock radii R_{sh}, reverse shock radii R_{rsh} shock velocities v_{sh} and maximum velocity of the ^{56}Ni + Tr $= 0.03$ iso-surface of our 3D long-time simulations. The forward shock of model e8.8 has passed the He/H interface and is traveling through the H-envelope. It left the core with about $100,000\,\mathrm{km/s}$ and is progressively decelerated due to the monotonically increasing ρr^3 within the H-envelope (see also Figure 4.1). Since the innermost neutrino-heated ejecta are not in sonic contact with the supernova shock, they do not feel the deceleration and thus travel with constant velocity of $\approx 3,000\,\mathrm{km/s}$ until they catch up with the immediate post-shock matter at $t_{\mathrm{pb}} \approx 130\,\mathrm{s}$. The interaction of the fast neutrino-heated ejecta with the post-shock material pushes the shock to higher velocities (see Figure 5.6). Nevertheless, the forward shock decelerates continuously (without any phases of acceleration) until it reaches the surface of the star. Note the large deceleration of the shock from its initial velocity of $75,000\,\mathrm{km/s}$ at $t_{\mathrm{pb}} = 2.55\,\mathrm{s}$ down to $< 1000\,\mathrm{km/s}$ when it leaves the star. A large fraction of the kinetic energy of the shock wave is used in heating the hydrogen in the outer layers of the envelope leaving around $0.25 \times 10^{49}\,\mathrm{erg}$ of kinetic energy in the ejecta.

The early strong deceleration of the forward shock at the bottom of the H-envelope at $t_{\mathrm{pb}} \gtrsim 0.21\,\mathrm{s}$ (see also Figure 4.1) has lead to the compression of the CO and He layers into a high density shell. Less than $1\,\mathrm{s}$ later, a strong reverse shock forms at the base of this shell as the forward shock is progressively slowed down. The dense shell separates the postshock material from the neutrino-heated ejecta as can be seen in the density profile shown in Figure 5.7. It is remarkable that in the ECSN the neutrino-heated ejecta are denser than the postshock shell of the matter swept up by the shock in the H-envelope. The formation of the dense shell or "wall" (Kifonidis et al., 2006) has important consequences for the evolution of the metal-rich ejecta as well as for the growth of Rayleigh-Taylor instabilities.

After $t_{\mathrm{pb}} \approx$ 1h, continuous deceleration of the forward shock causes the reverse shock to travel back in mass coordinate. (see Figure 5.7). It takes, however, a total of approximately $\sim 9\,\mathrm{h}$ for the reverse shock to reach the inner boundary of our computational domain.

The forward shock of model z9.6 has already crossed the CO/He interface at t_{map} and is traveling at roughly $27,000\,\mathrm{km/s}$. Behind the shock, a dense shell has formed due to the deceleration of the fast neutrino-driven wind in a wind-termination shock. In between the shocks, the high density peak atop the bulk of the ejecta is formed by the deceleration of the forward shock at the CO/He interface. Above the O/He interface and similar to model e8.8, a featureless density profile in the He-core and hydrogen envelope leads to an untroubled but gradually decelerated expansion of the forward shock, which reaches the stellar surface at around $t_{\mathrm{pb}} \approx 1.3\,\mathrm{d}$). At the time of shock breakout the forward shock travels only at $\sim 1000\,\mathrm{km/s}$ due to the large deceleration in the hydrogen envelope of the star. Different from the ECSN progenitor the reverse shock forms within the He-core of the star (see Figure 5.7) but also fairly early at some $t_{\mathrm{pb}} \approx 15\,\mathrm{s}$. Within the next $1000\,\mathrm{s}$, the reverse shock propagates back in radius and reaches the inner boundary at $t_{\mathrm{pb}} \approx 1\,\mathrm{h}$, which is 8 hours earlier than in model e8.8.
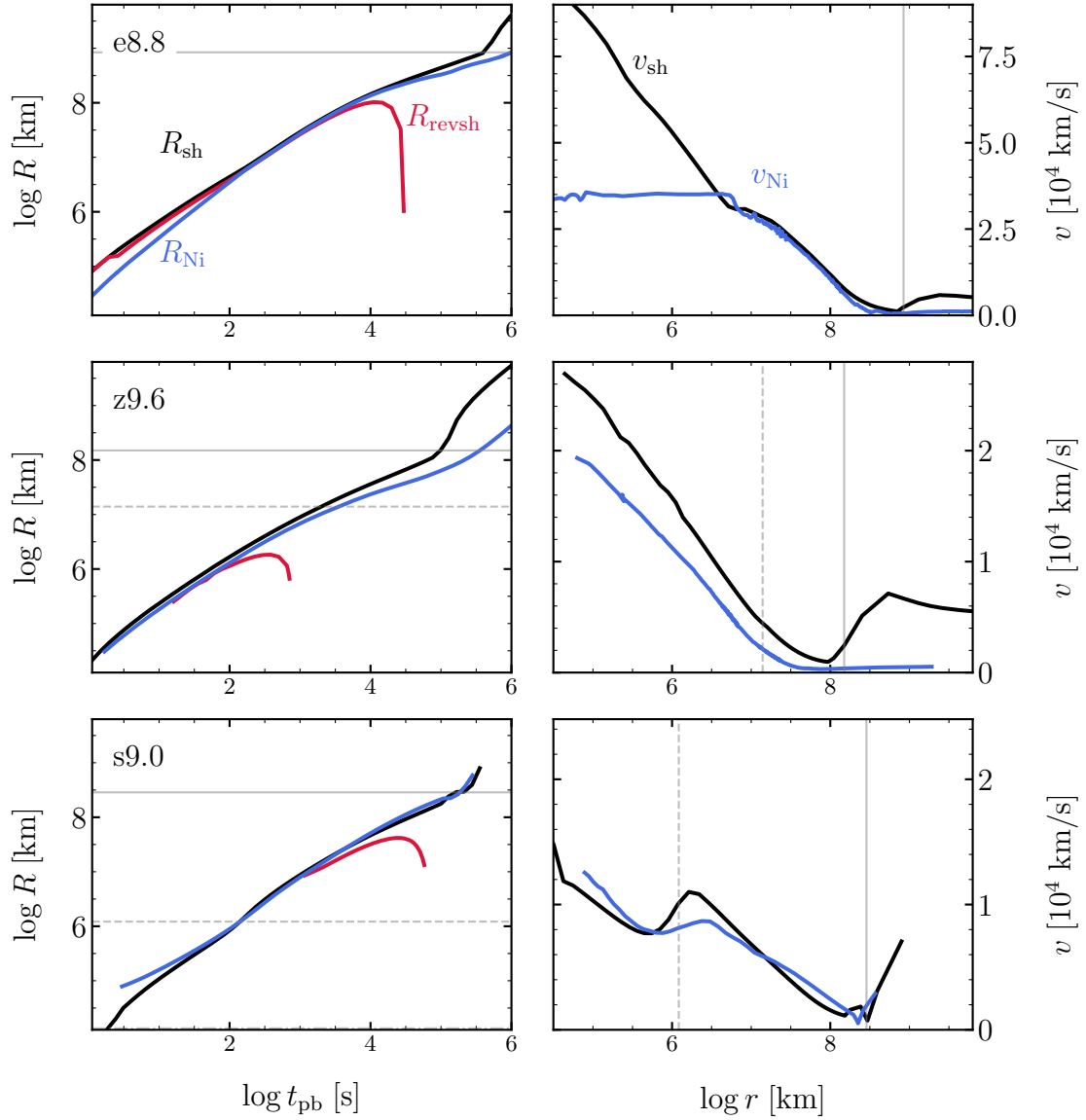
Fig. 5.6 *Left panels*: Angle-averaged shock radius R_{sh} (black), angle-averaged reverse shock radius R_{rsh} (red) and maximum radius of the mass fraction $X_{^{56}Ni+Tr} = 0.03$ iso-surface (blue). *Right panels*: Average shock velocity v_{sh} (black) and maximum velocity of the $X_{^{56}Ni+Tr} = 0.03$ iso-surface (blue) in our 3D long-time simulations. The vertical gray dashed and solid lines mark the location of the He/H interface and the surface of the progenitor stars, respectively. The expansion of the forward shock in the ECSN-like progenitors proceeds without continuous deceleration until the shock reaches the stellar surface. In contrast, the forward shock in model s9.0 accelerates strongly around the He/H interface. The reverse shocks in models e8.8 and z9.6 form within ≈ 1 s and ≈ 15 s, respectively, whereas we observe the formation of a reverse shock from the He/H interface in model s9.0 at ≈ 2500 s. Note that in model s9.0 the velocity of the fastest $^{56}Ni + Tr$ surface is higher than the average shock velocity within the hydrogen envelope of the star.

The trajectories of the forward and reverse shocks in the 3D simulation of model s9.0 are shown in the right panels of Figure 5.6. The long-time simulation is initiated at $t_{\rm pb} = 3.14\,{\rm s}$, when the forward shock has just crossed the CO/He interface and is traveling at $v_{\rm sh} \approx 11,000\,{\rm km/s}$, just a fraction of the shock velocity found in the ECSN-like models. Acceleration and deceleration of the supernova shock at the C/O interface causes the formation of a dense shell in the post-shock region (see Figure 5.7). The density contrast between the shell and the ejecta is, however, around one magnitude smaller than found for the dense shells that formed at the core/envelope boundary in model e8.8 and at the CO/He interface in model z9.6. In the following, the shock slows down to $v_{\rm sh} \approx 8,000\,{\rm km/s}$ within the He-core of the star before it accelerates again around the He/H composition interface reaching $v_{\rm sh} \approx 7,500\,{\rm km/s}$. This is due to the steep density gradient just below the He/H interface in the progenitor. Thereafter, the forward shock encounters the increasing ρr^3 in the hydrogen envelope and is thereby strongly decelerated, causing a compression of the post-shock material into a double-peaked dense shell. At the bottom of the hydrogen shell a strong reverse shock forms shortly afterwards (see Figure 5.7). Note that the formation of the reverse shock from the He/H interface occurs well later than observed in the ECSN-like progenitors. Eventually the reverse shock reaches the inner boundary of our numerical grid at $t_{\rm pb} \approx 25\,{\rm h}$. A first reverse shock from the CO/He interface had moved back to the stellar center at $t_{\rm pb} \approx 30\,{\rm s}$ (Figure 5.7). The minimum spherically shock radius encounters the stellar surface at $t_{\rm pb} \approx 2.8\,{\rm d}$ while the maximum radius of the shock reaches the surface already at $t_{\rm pb} \approx 2.1\,{\rm d}$ (see also Section 5.3.2).
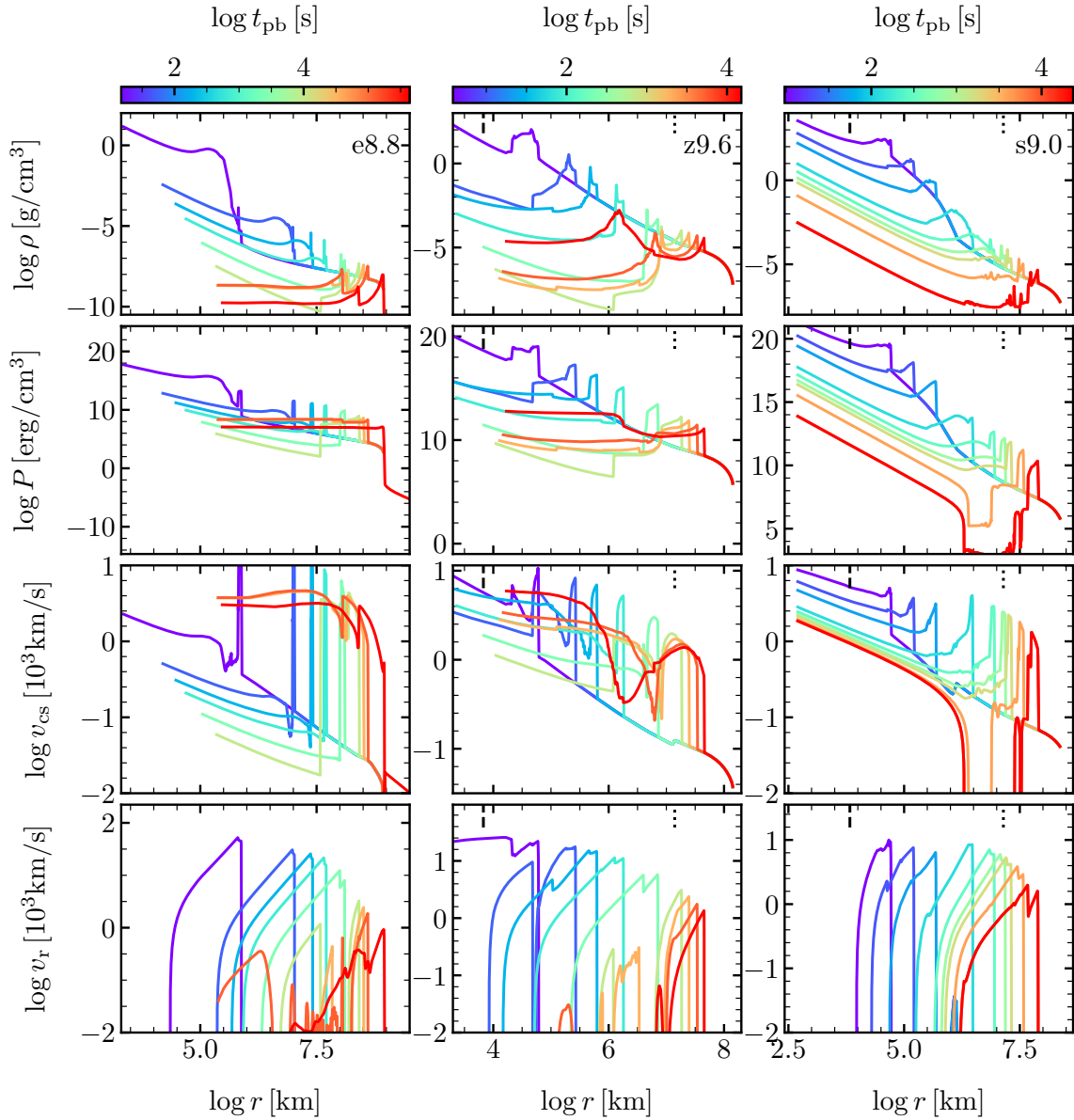
Fig. 5.7 Profiles of the density (first row), pressure (second row), sound speed v_{cs} (third row) and radial velocity (last row) at selected times of our 1D simulations of models e8.8 (left), z9.6 (middle) and s9.0 (right). The dashed and dotted lines at in the upper parts of the plots indicate the radii of the CO/He and He/H composition interfaces. Note that a positive gradient of v_{cs} indicates RT unstable layers (see Equation (5.12)).

5.3.2 Morphology of Neutrino-heated Ejecta

In the following we focus on the long-time development of the early-time asymmetries which we trace by the propagation of the neutrino-heated ejecta or more specifically the ^{56}Ni + Tr-rich material. Kifonidis et al. (2003) already noted that ^{56}Ni is produced between the high-entropy bubbles that expand due to strong neutrino-heating from below. Thus the distribution of ^{56}Ni traces the asymmetries that developed during the onset of the explosion.

Model e8.8

In Figure 5.9 we show slices of the ^{56}Ni + Tr mass fraction of the 3D simulation of model e8.8. The dashed white line indicates the shock radius, whereas the thin dotted white or black line indicates the position where the enclosed mass equals the mass shell of the He/H interface in the progenitor.

Exactly as in the 1D simulation, the CO and He layers are compressed into a dense shell, just behind the supernova shock. The dense shell is located at a radius of $\approx 3{\times}10^5$ km at $t_{\rm pb} = 9$ s (see Figure 5.7 and Figure 5.8). Already at $t_{\rm pb} \approx 1.5$ s, a reverse shock begins to form at the bottom of the dense shell (see thin yellow shell in Figure 5.8 at 9 s) . By this time the bulk of the neutrino-heated ejecta has expanded in the volume inside $\approx 2{\times}10^5$ km. While this innermost metal-rich material seems to expand in a basically self-similar fashion (see similarity of the snapshots until $t_{\rm pb} = 150$ s in Figure 5.9), the growth of the RT instability in small protrusions in the unstable layer around the He/H interface (located between the dense shell and the forward shock) begins to fragment the surface of the dense ejecta. At $t_{\rm pb} = 300$ s, the neutrino-heated ^{56}Ni +Tr ejecta catch up with the expanding dense shell and are strongly decelerated. RT plumes become clearly visible near the He/H interface first at about 1400 s in Figure 5.9.
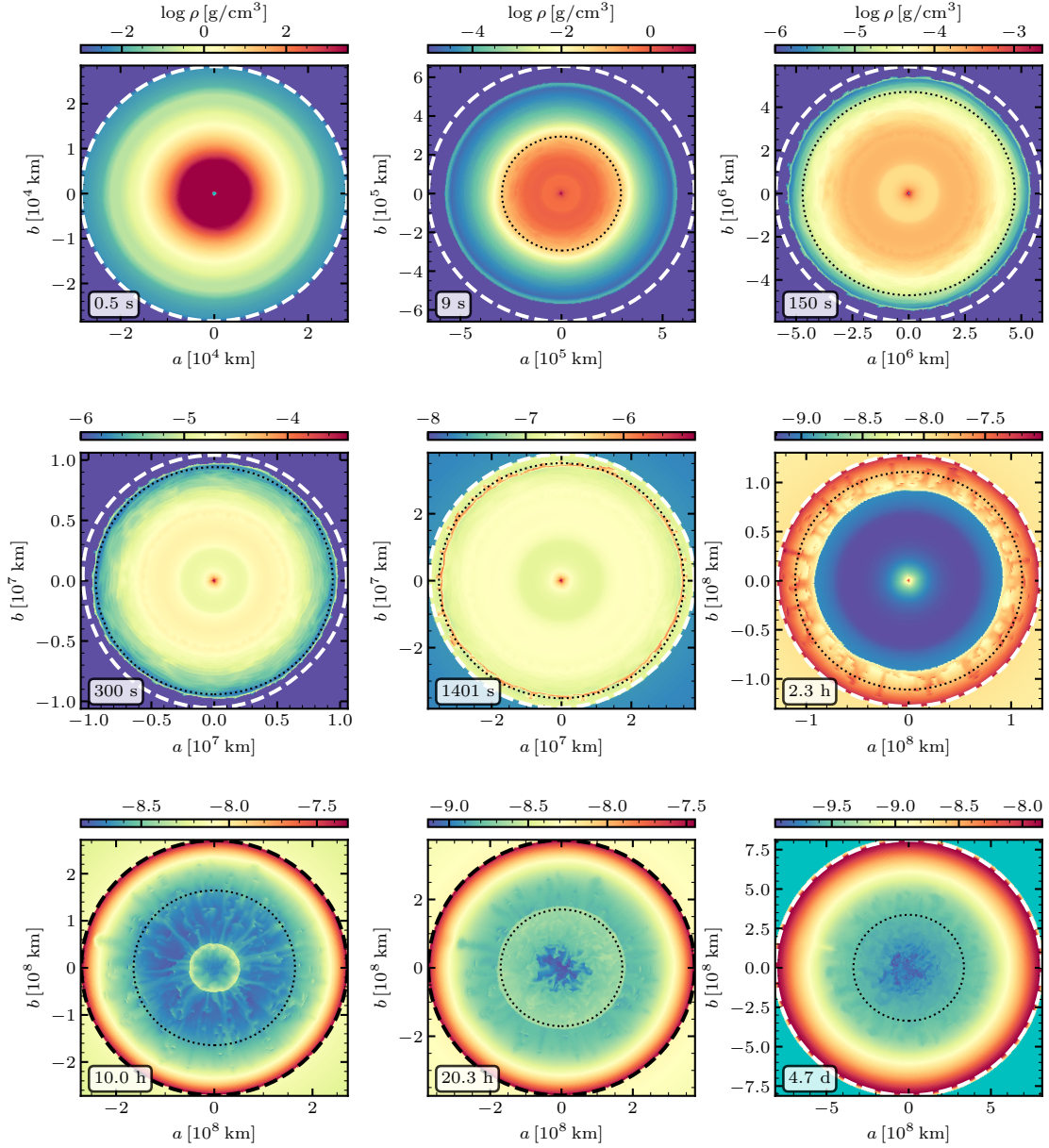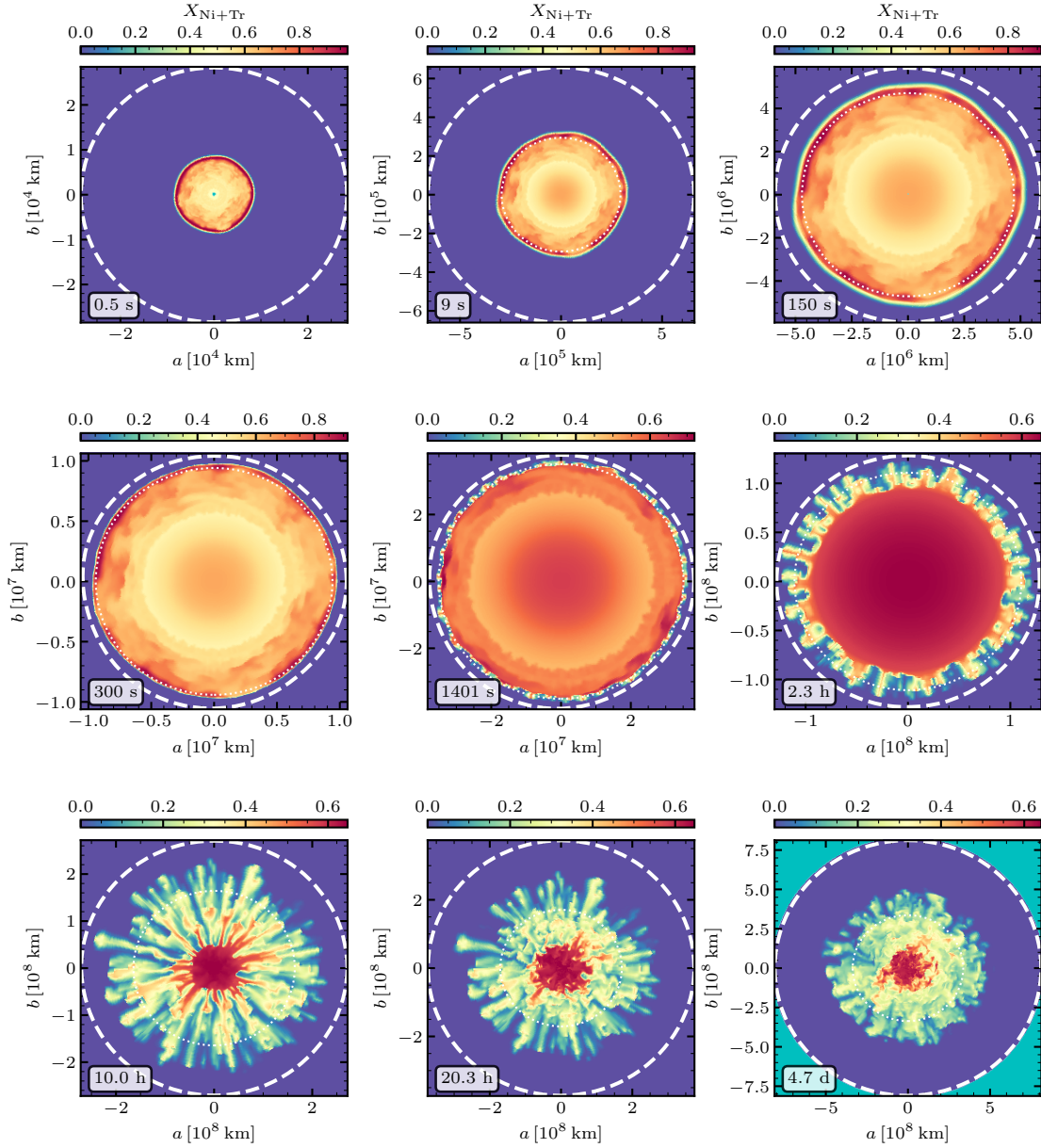
Fig. 5.8 Slices showing the density distribution in the 3D simulation of model e8.8. The dashed white or black line indicates the position of the supernova shock and the dotted white or black lines mark the radial location where the enclosed mass is equal to the mass coordinate of the He/H shell of the progenitor. Cyan colored regions in the lower right panel represent the surrounding medium embedding the progenitor. The dense shell at which the reverse shock will form (see also Figure 5.9) is first visible as the light yellow ring with a radius of about $\approx 3 \times 10^5$ km at $t_{\rm pb} = 9$ s. The panel at $t_{\rm pb} = 2.3$ h shows the formation of small RT fingers. These fingers grow with time and partly take up the neutrino-heated material (see panels at $t_{\rm pb} \approx 2.3$ h and $t_{\rm pb} \approx 10$ h). At $t_{\rm pb} \approx 4.7$ d the innermost ejecta are characterized by an overall spherical shape, superimposed with the remains of the RT fingers. The reverse shock is very prominent at $t_{\rm pb} \approx 2.3$ h and travels inward from about 3 h on (see Figure 5.6). It reaches the center at $t_{\rm pb} \approx 9$ h to be reflected outward again (see lower left panel).

In consequence, the higher entropy/lower density bubbles are compressed to flat structures while the higher density regions in between the bubbles are able to penetrate the dense shell, thereby inducing perturbations at this interface. These RT plumes grow over the following hours around the mass shell of the He/H interface, mixing clumps of ^{56}Ni from the central volume outward into the carbon and helium rich layers.

The reverse shock, which is visible at $t_{\mathrm{pb}} = 2.3\,\mathrm{h}$ in Figure 5.8 as the yellow to blue discontinuity, begins to propagate back in radius, thereby compressing the innermost ejecta. At $t_{\mathrm{pb}} \approx 10\,\mathrm{h}$ the inward passage of the reverse shock and the growth of the RT instability has erased the initial structures present at the onset of the explosion. However, the overall morphology of the neutrino-heated ejecta is still basically spherical with only small scale asymmetries (see also Figure 5.10).

Fig. 5.9 Slices showing the ^{56}Ni+Tr mass fraction in the 3D simulation of model e8.8. The dashed white or black line indicates the position of the supernova shock and the dotted white or black line marks the radial location where the enclosed mass is equal to the mass coordinate of the He/H shell of the progenitor. Cyan colored regions in the bottom right panel represent the surrounding medium embedding the progenitor. Until $\approx$150 s the neutrino-heated ejecta expand essentially self-similarly. This untroubled expansion ends at about 300 s, when the material is decelerated in the dense postshock shell (see Figure 5.7). At $\approx$1400 s the growing RT instability at the He/H interface clearly begins to affect the outer layers of the neutrino-heated ejecta. From about 2 h on the plumes grow in size, while the reverse shock (visible at the base of the plumes) begins to propagate back in radius (see Figure 5.6). 9 h after bounce the reverse shock reaches the center and on the way compresses the metal-rich ejecta in the central region. Note that the plumes are evenly distributed in angular direction and radial extent.
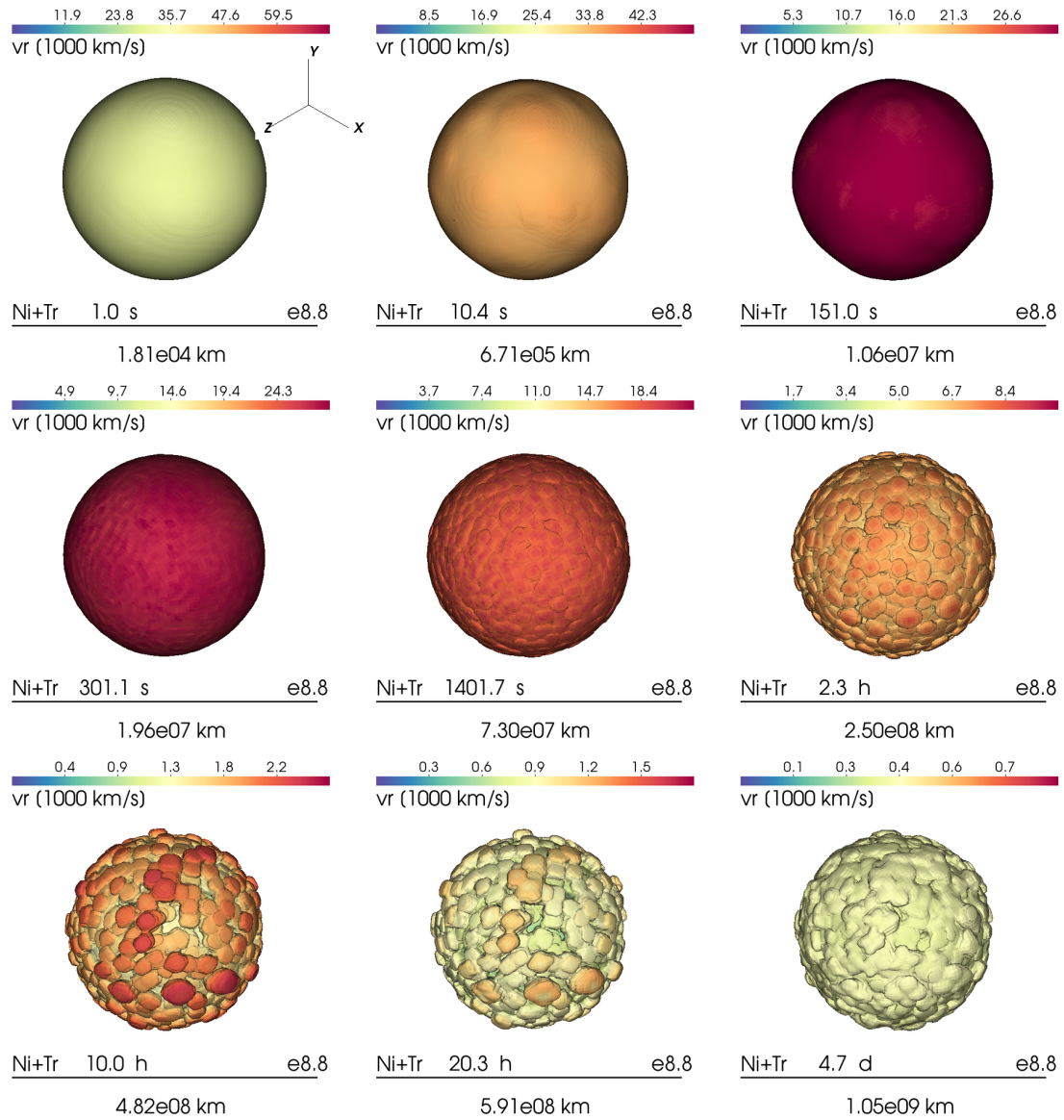
Fig. 5.10 3D renderings of model e8.8 showing the ^{56}Ni + Tr = 0.03 isosurface at the same times as in Figure 5.9. The color-coding represents the radial velocity of the material and the tripod in the left panel indicates the orientation of the global coordinate system. From the initially spherical distribution of the neutrino-heated ejecta we observe the growth of small scale RT plumes. Due to the spherical beginning of the explosion and the growth of RT instabilities on small angular scales the final distribution of the neutrino-heated ejecta is basically isotropic.

Model z9.6

In Figure 5.12, we show slices of the ^{56}Ni + Tr mass fraction in the 3D simulation of model z9.6. The dashed white line indicates the shock radius while the dotted lines indicate the positions where the enclosed mass equals the mass shells of the CO/He and He/H interfaces in the progenitor. The dense shell which forms after the forward shock crossed the CO/He interface (see Figure 5.7) is visible as the circular dark-red region after about 9 s in Figure 5.11.

Within the first ≈ 9 s the fastest of the neutrino-heated ejecta encounter this dense CO-rich shell (see Figure 5.11) and are compressed and squeezed to flat structures around 30 s later. Similar to the results presented for the e8.8 model, the slightly over-dense regions between the high entropy plumes induce long-wavelength perturbations as they deform and try to penetrate the RT unstable dense shell. Over the next few minutes, RT fingers grow on top of these deformations and fragment the dense shell into numerous ^{56}Ni-rich shrapnels.

While the fingers grow progressively, the reverse shock from the shock propagation through the He layer (visible as the green to yellow discontinuity at $t_{\rm pb} = 187$ s in Figure 5.11) begins to propagate back in radius. At $t_{\rm pb} = 829$ s the reverse shock has almost reached the center of our numerical grid having compressed and decelerated the innermost material. At $t_{\rm pb} = 1.7$ h, the forward shock has crossed the He/H interface and the inner material has been fully shredded by the instability.

As the shock does not show any significant change in velocity at the He/H interface, we observe no additional growth of the RT instability nor the formation of another reverse shock. Thus, the morphology of the innermost ejecta seems to be determined early on, already before the shock crosses the He/H interface.

Comparing the distribution of ^{56}Ni and Tr of model e8.8 (Figure 5.9) model z9.6 (Figure 5.12) shortly before shock breakout we find a slightly more clumped morphology in the $9.6 \, {\rm M}_\odot$ progenitor. The morphology of the neutrino-heated ejecta in model z9.6 also remains fairly spherical with small-scale clumps (see Figure 5.11 and 5.13). However, different from model e8.8 one can recognize a hemispheric asymmetry with bigger plumes between the 8 o'clock and 10 o'clock positions in Figure 5.12 and weaker plumes in the opposite hemisphere. The strongest plume is visible near the 11 o'clock position in Figure 5.13.
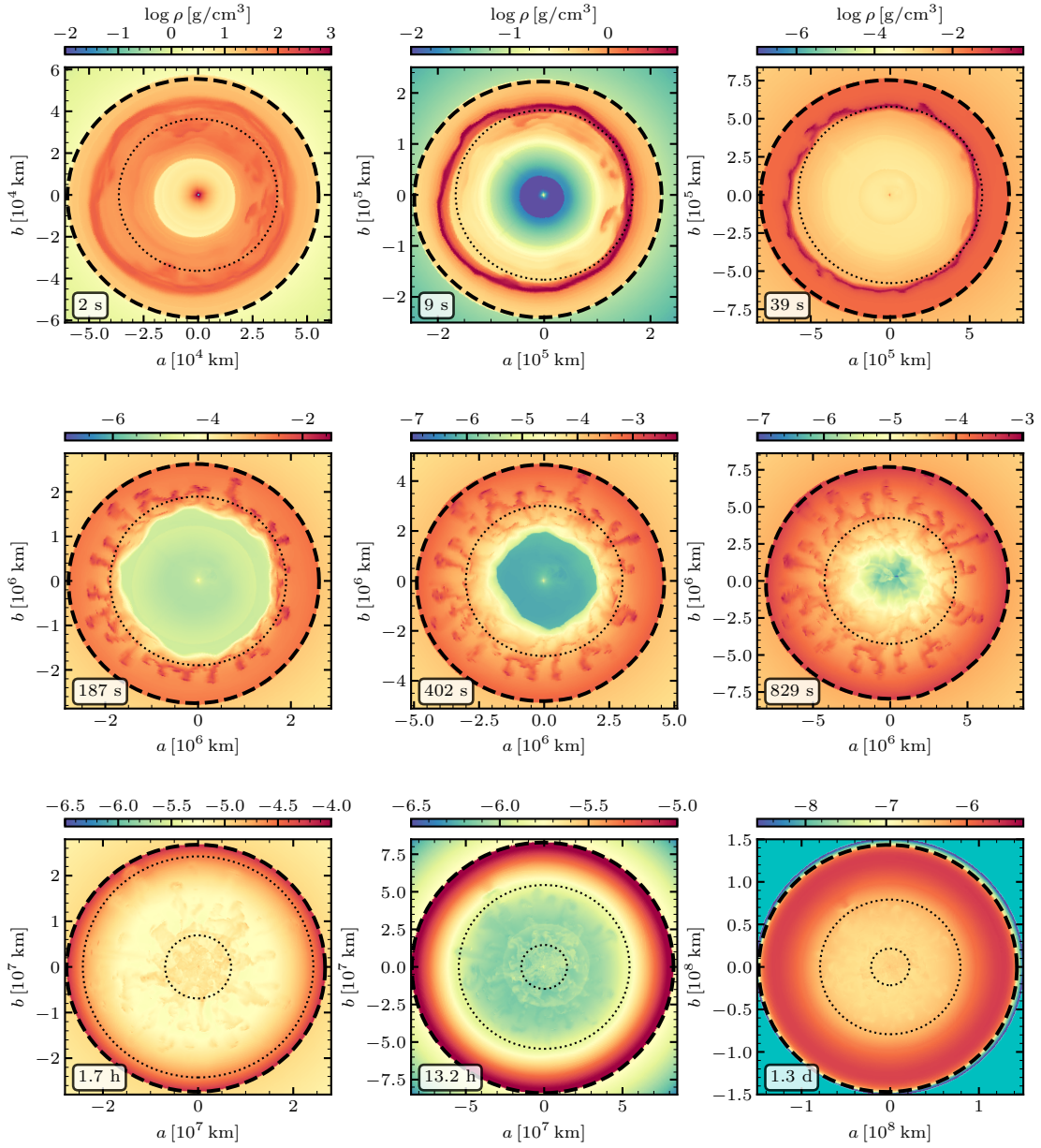
Fig. 5.11 Slices showing the density in the 3D simulation of model z9.6 at the indicated times. Cyan colored regions in the bottom right panel represent the surrounding medium of the progenitor. The dashed black line marks the shock position, the dotted black lines indicate the radial locations where the enclosed mass equals the mass shells of the Co/He and He/H interfaces of the progenitor. A termination shock of the neutrino-driven wind is visible as the yellow/orange discontinuity at $t_{pb} \approx 2\,s$. The shock deceleration in the layer leads to the formation of a dense shell that is extremely compressed by the outward shock from the reflection of the wind termination shock at the center. Over the next $\approx 100\,s$ RT plumes start to grow within the unstable region between the shocks thereby fragmenting the dense shell. A second reverse shock from when the supernova shock propagates through the He-layer of the progenitor. As this reverse shock propagates back in radius, similar to the results presented for model e8.8, the plumes grow to their maximal radial extent (see panels at $t_{pb} = 187\,s - 829\,s$). The final morphology of the ejecta at $t_{pb} \approx 1.3\,d$ resembles the late time morphology in model e8.8.

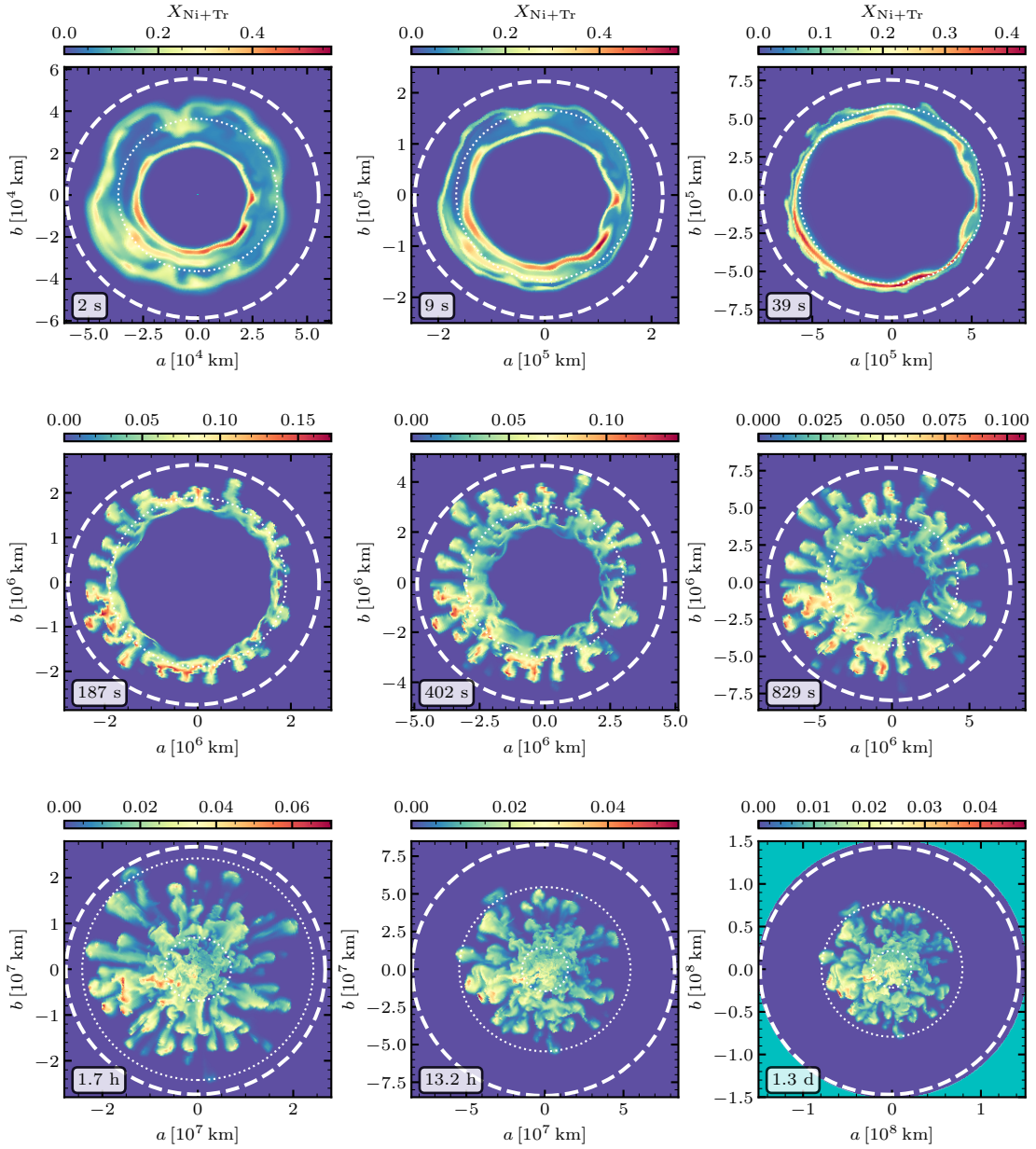Fig. 5.12 Slices of the ^{56}Ni + Tr mass fraction of the 3D simulation of model z9.6 at the indicated times. Cyan colored regions in the bottom right panel represent the surrounding medium of the progenitor. The dashed white line marks the shock position, the dotted white line indicate the radial locations where the enclosed mass equals the mass shells of the CO/He and He/H interfaces of the progenitor. The initial asymmetries that developed during the onset of the explosion are still visible at $t_{pb} = 1.5\,s$, but they are soon compressed to flat structures as they encounter the RT unstable dense shell behind the CO/He interface (see times from $t_{pb} = 9\,s$ to $t_{pb} = 39\,s$ and also Figure 5.11). Over the next, roughly, one hour, the growing RT instability mixes the outer ^{56}Ni-rich layers outwards in mass coordinate in numerous small fingers. 1.7 h after bounce the RT instability has basically saturated and the first iron-rich clump reach the He/H interface of the progenitor, where in model z9.6 no secondary Rt instability occurs. The final morphology of the ^{56}Ni-rich ejecta has mostly lost any resemblance with the state at t_{map} and is dominated by small-scale structures. However, the overall distribution of ^{56}Ni and Tr remains roughly spherical with many small-scales asymmetries and only a slight global deformation, which exhibits larger and stronger iron-rich plumes between the 8 o'clock and 10 o'clock directions and weaker structures in the opposite directions.
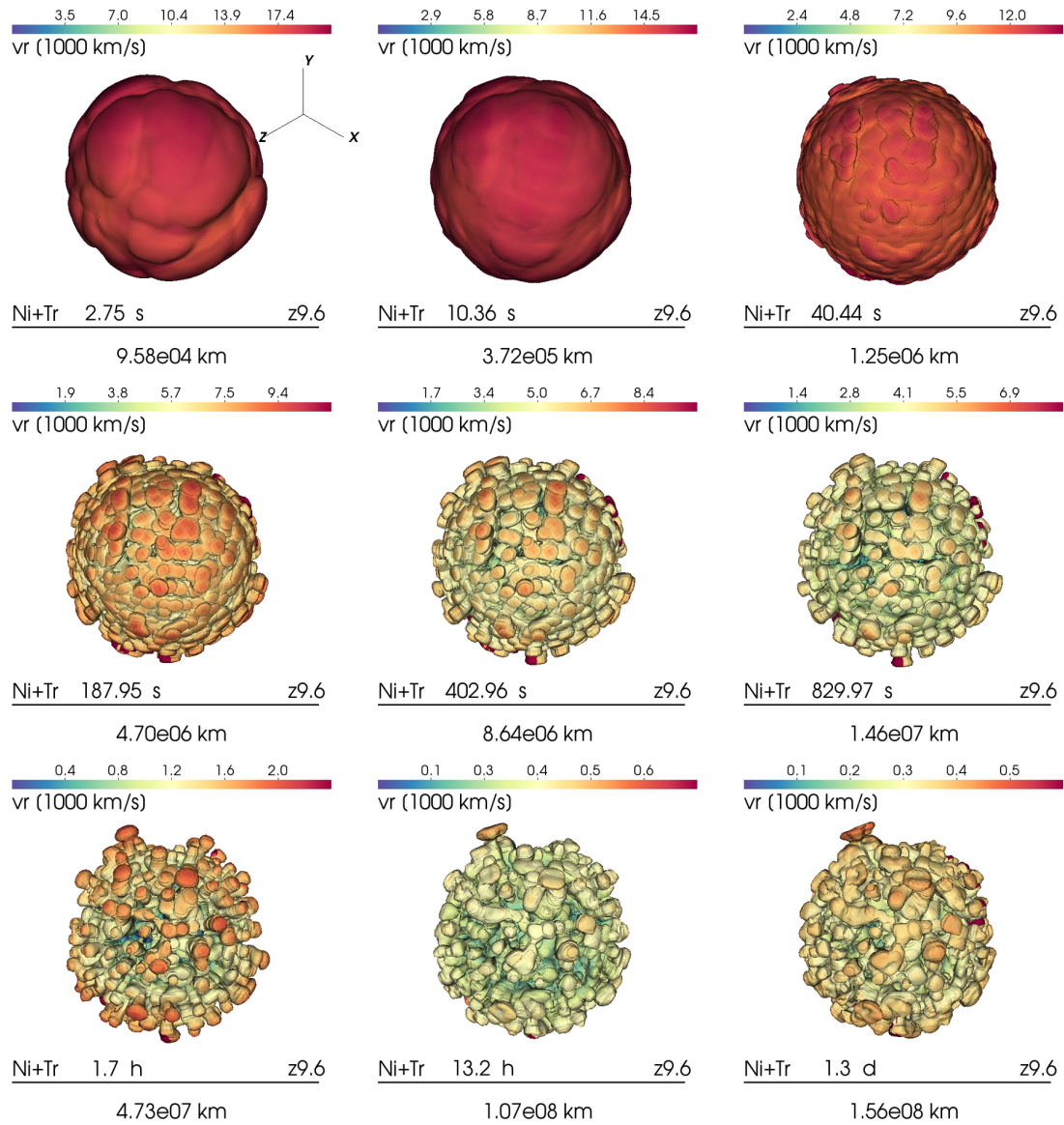
Fig. 5.13 3D renderings of model z9.6 showing the ^{56}Ni + Tr = 0.03 isosurface. The color-coding represents the radial velocity. At $t_{\mathrm{pb}} = 10.36$ s one can see the initial "ripples" of the developing RT instability which grows from perturbations at the CO/He interface. 170 s later the morphology of the ejecta is dominated by small-scale RT fingers. Over the next hours, the RT instability grows at similar rates in all directions, eventually leaving an overall spherical morphology of the neutrino-heated ejecta.

Model s9.0

The evolution of the neutrino-heated ejecta of model s9.0 proceeds drastically differently from the ECSN-like progenitors. As discussed in Section 4, the initial asymmetries and shock deformation seen in model s9.0 are considerably larger than found in the ECSN-like models. Strong convection leads to the formation of a large high entropy plume, which is rich in iron-group material and expands about two times faster than the surrounding material at the time of shock-revival ($t_{\mathrm{pb}} \approx 0.5\,\mathrm{s}$). It crosses the CO/He interface of the star at $t_{\mathrm{pb}} \approx 1.3\,\mathrm{s}$, shortly after the forward shock. In comparison, the slowest moving material reaches the interface around $0.65\,\mathrm{s}$ later.

The crossing of the CO/He interface by the shock wave has several dynamical consequences. Due to the increasing ρr^3 behind the interface, the shock is decelerated and the postshock matter is swept up and compressed into a dense shell. Note that the neutrino wind in this model is very weak and, different from model z9.6, there is no low-density central region and no wind termination shock. Instead, the central volume around the neutron star contains relics of ^{56}Ni-rich low-density plumes and ^{56}Ni-poor, higher density downflows all the time.

The high density shell behind the shock is aspherical in contrast to the shells found in the ECSN-like progenitors, which is also reflected by the still deformed supernova shock (see first two panels in Figure 5.14 for $t_{\mathrm{pb}} = 3$ and $124\,\mathrm{s}$). Around the dense shell we observe the growth of large plumes which stem from the initial asymmetries of the explosion. These can be seen in the 10 o'clock direction in Figure 5.15 at $t_{\mathrm{pb}} = 124\,\mathrm{s}$ and in Figure 5.16. At the top of these plumes small RT fingers grow, in line with the analysis of the amplification factors presented in Section 5.2. Note that at this point in time the still deformed supernova shock crosses the He/H interface (see Table 2.1).

Due to the varying ρr^3 around this composition interface, the shock accelerates and decelerates, thereby forming a dense shell (see yellow shell in Figure 5.14 at $t_{\mathrm{pb}} = 742\,\mathrm{s}$).
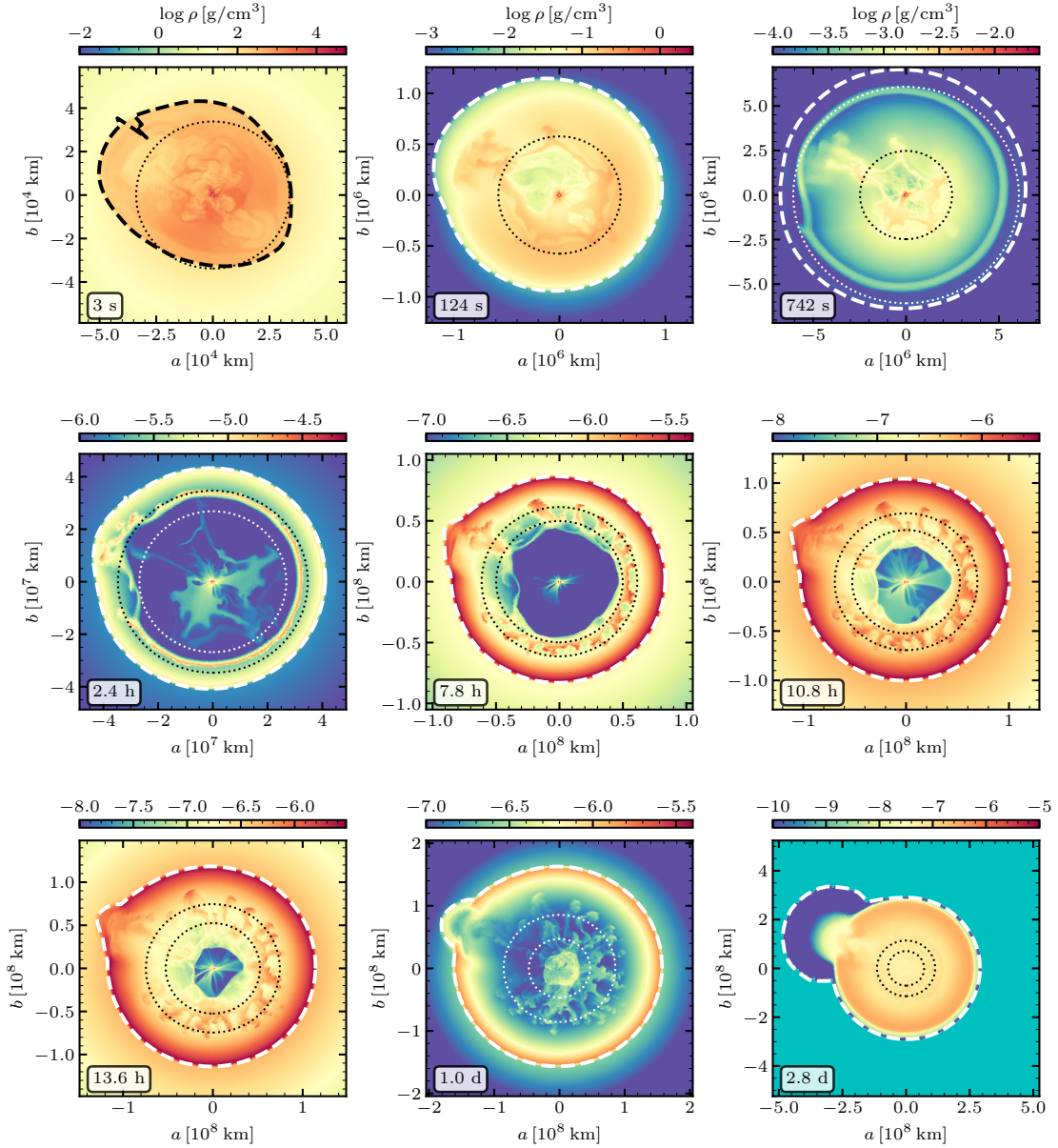
Fig. 5.14 Slices of the density of model s9.0 at the indicated times. The dashed white or black line indicates the shock radius while the dotted white or black lines mark the locations where the enclosed mass equals mass shells of the CO/He and He/H interfaces of the progenitor. The cyan colored regions in the bottom right panel represents the surrounding medium of the progenitor. Different from the ECSN-like progenitors we observe the growth of large-scale RT plumes caused by the large asymmetries at the onset of the explosion. The seed for the largest plume is set already at around $3\,s$ after bounce when the shock passes the CO/He interface. We first observe the growth of the RT instability at the top of the largest and fastest initial convective plume (see e.g. $t_{\rm pb} = 124\,s$ in 10 o'clock direction) and muss less deceleration of a dense clump of ^{56}Ni + Tr penetrating the CO/He interface in this direction ad therefore begins to move far ahead of the slower ^{56}Ni + Tr. Shortly afterwards the plume arrives at the unstable He/H interface, inducing a large-scale perturbation there. While the slower clumps of ^{56}Ni + Tr are further decelerated by the reverse shock that forms at the He/H interface, the large clump begins to push the shock, thereby transporting a significant amount of neutrino-heated ejecta to velocities larger than the average shock velocity (see also Figure 5.6).
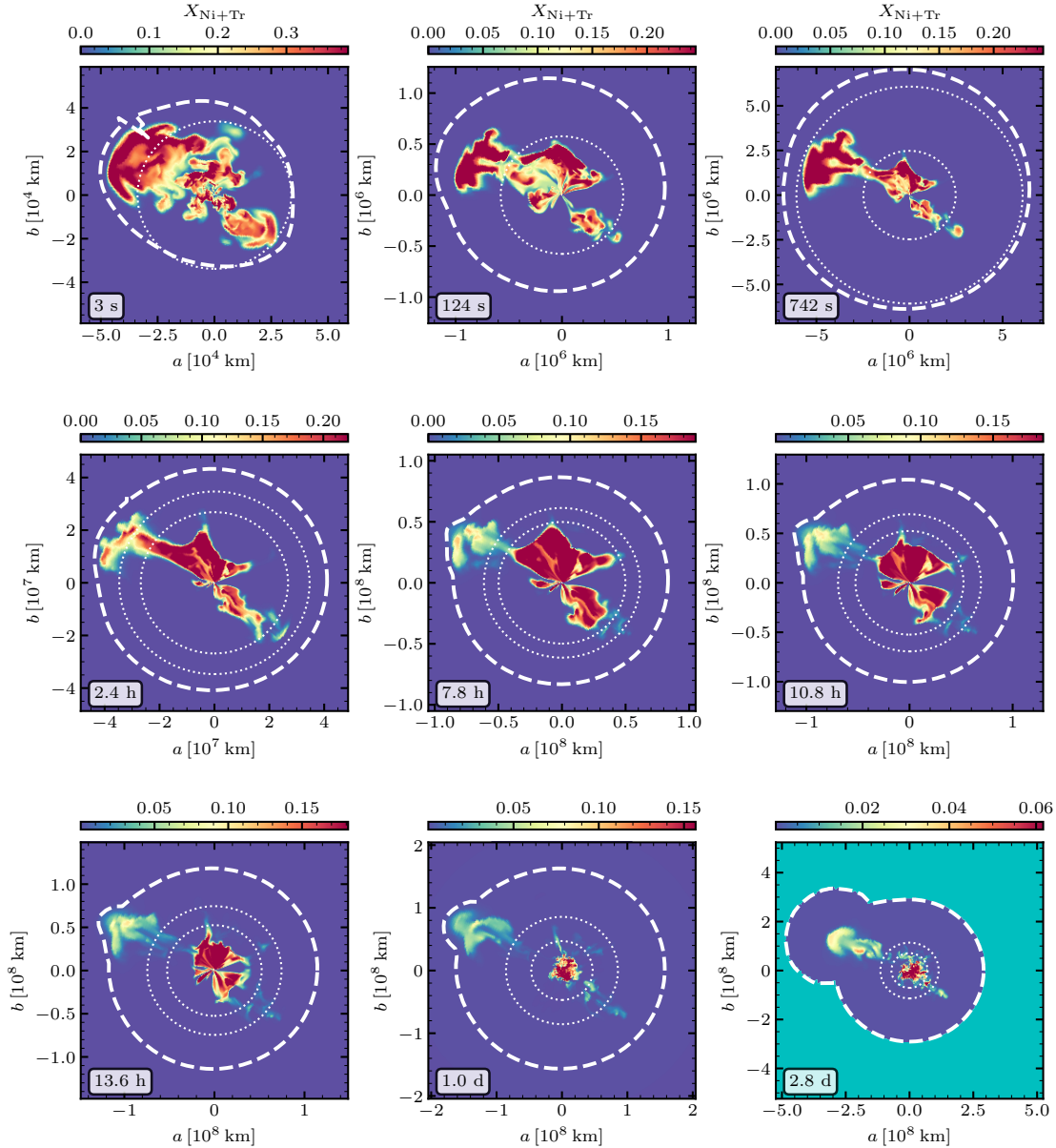
Fig. 5.15 Slices of the ^{56}Ni + Tr mass fraction of model s9.0 at the indicated times. The dashed white or black line indicates the shock radius while the dotted white or black lines indicate the position where the enclosed mass equals the mass shells of the CO/He and He/H interfaces of the progenitors. The cyan colored region in the bottom right panel represents the embedding surroundings of the progenitor. The ^{56}Ni + Tr distribution underlines the connection between the initial asymmetries and the large clump that overtakes the average shock even before shock breakout. At $t_{pb} = 3\,s$ around 25% of the ^{56}Ni-rich material is ejected in the 10 o'clock direction. While the innermost ejecta are compressed and decelerated strongly by the dense shells and reverse shocks that form at the CO/He and He/H interfaces, about half of the large clump experiences less dramatic deceleration and deforms the otherwise spherical shock wave shortly before shock breakout.

When the fast and dense metal-rich plume encounters the shell, it induces a high-amplitude perturbation in this RT unstable layer. From this perturbation, aided by the large initial momentum of the metal-rich plume, we observe the growth of a large RT plume. As the shock is decelerated in the H-envelope, the dense plume retains higher velocities than the speed of the shock and the plume is able to deform the forward shock in its trajectory (compare Figure 5.14 at $t_{pb} \geq 2.4\,h$).

Concurrently, the reverse shock, which forms at the bottom of the He/H interface, propagates back into the ejecta and strongly decelerates and compresses the ^{56}Ni + Tr rich material close to the center (see Figure 5.14 at $t_{pb} \approx 7.8h$). The growing RT instability around the CO/He interface (clearly visible in Figure 5.14 at $t_{pb} \approx 7.8h$) seems to only slightly affect the outer boundary of the central ^{56}Ni + Tr-rich material, as can be seen in Figure 5.15 at $t_{pb} \geq 7.8h$ (in line with the small amplification factors found in this region).
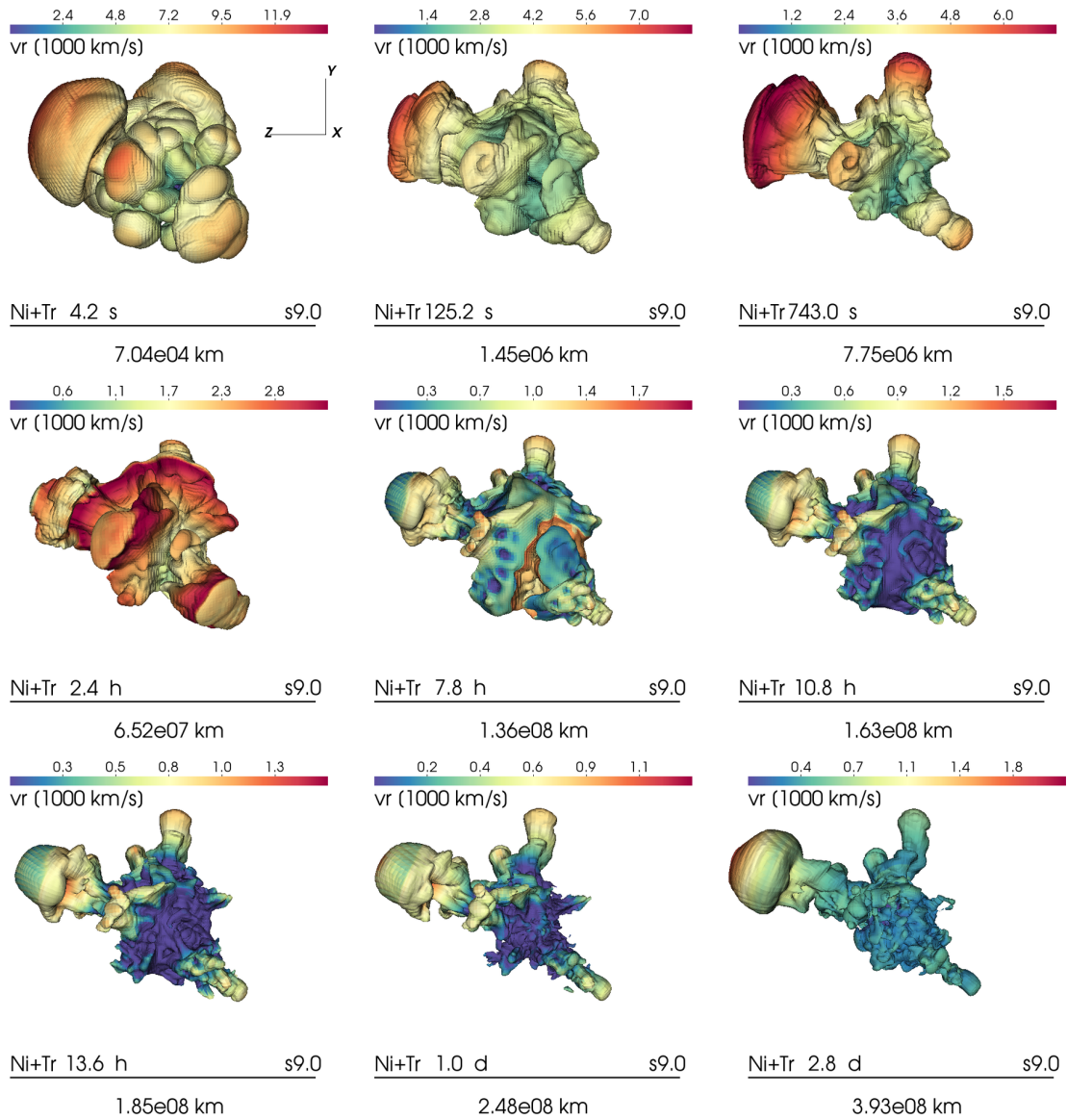
Fig. 5.16 3D renderings of the $X_{^{56}\mathrm{Ni}+\mathrm{Tr}} = 0.03$ iso-surface of model s9.0 at the indicated times. The color-coding represents the radial velocity of the material and the tripod in the left panel indicates the orientation of the global coordinate system. During the first roughly 800 s the largest initial asymmetries grow to large metal rich clumps, slower iron-group matter in the interior is decelerated by the collision with the dense shell formed around the CO/He interface. In the following, these fastest plumes encounter the dense shell behind the He/H and induce large-amplitude perturbations at the RT unstable layer. Consequently, large metal rich RT fingers begin to grow from the interface. At $t_{\mathrm{pb}} = 2.8\,\mathrm{d}$ we find one very large and two smaller metal rich plumes, of which the larges one penetrates the surface of the star even ahead of the average shock radius (see also Figures 5.12 and 5.11).

Due to the strong deceleration of the innermost material, the fast plume almost fully detaches from the core material as it propagates through the hydrogen envelope of the star (see last two panels in Figures 5.15, 5.14 and 5.16). It encounters the surface of the star at around $t_{\rm pb} \approx 2.1$ d, so more than half a day earlier than the spherically shaped minimum radius of the which reaches the stellar surface at $t_{\rm pb} \approx 2.8$ d. Why is the large plume able to travel with such high velocities, even deforming the forward shock, while the bulk of material travels at considerably slower speed? First, the fastest ^{56}Ni + Tr material is, at all times, in close vicinity of the immediate post-shock matter (see Figure 5.6). Second, after the forward shock has crossed the He/H interface, the nickel-rich plume is decelerated less than the average shock (see Figure 5.6), since this material is denser than its surroundings. Third, large growth rates at the He/H interface lead to an efficient outward mixing of the dense plume within the unstable layers and the plume can therefore also escape the strong deceleration by the reverse shock. In consequence, the ^{56}Ni + Tr-rich plume catches up with the forward shock in the hydrogen envelope. Due to its large momentum it deforms the outgoing forward shock in its trajectory. This is similar to a transient situation about half an hour and 3 h in model e8.8, where the neutrino-heated ejecta in RT plumes catch up with the strongly decelerated immediate post-shock material, thereby pushing the forward shock (see Figure 5.6 and Figure 5.8).
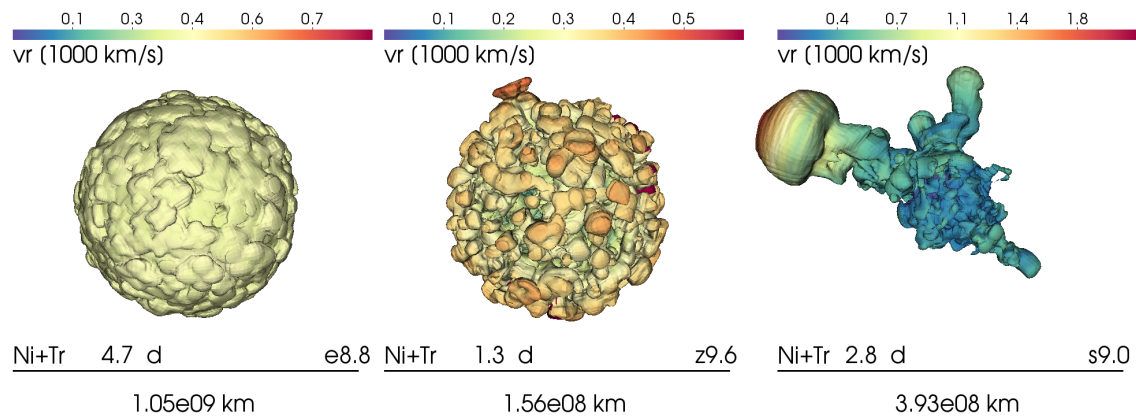
Compilation of the Results

Fig. 5.17 3D renderings of the 3D models (e8.8, z9.6, s9.0 from left to right) showing the ^{56}Ni + Tr = 0.03 isosurface at the indicated times. The color-coding represents the radial velocity. The similar structure of the ECSN-like progenitors manifests itself in the final morphology of the neutrino-heated ejecta. Numerous small RT plumes extend from the central region, but the overall morphology remains spherical. In contrast, model s9.0 is dominated by large scale asymmetries.

Summarizing our results, we show in Figure 5.17 3D renderings of the ^{56}Ni + Tr = 0.03 isosurface at the time of shock-breakout for all our 3D simulations. The similarity of models e8.8 and z9.6 is again striking and remembers of the spherical morphology also found in type Ia supernovae such as the remnant of Kepler's supernova (SN1604). The morphology of the neutrino-heated ejecta found in model s9.0, however, is strongly asymmetric and is dominated by a large metal-rich plume. The s9.0 model resembles the morphology at shock breakout found for more massive progenitors (see e.g. Wongwathanarat et al. (2015)).

5.3.3   Extent of Mixing

Model e8.8

In Figure 5.18 and Figure 5.19 we display the mass distributions of free protons from NSE freeze-out, hydrogen from the envelope, helium, carbon, oxygen-neon-magnesium, nickel and the tracer nucleus as functions of radial velocity and mass coordinate (defined as the enclosed mass $M(r)$ at radius r) for model e8.8. The distributions shows the fraction of the total mass of a certain element, normalized to the total mass of that element contained within the forward shock. For the evaluation in mass coordinate we use 25 bins to sample the ejecta from the inner boundary to the shock radius, whereas we use 50 bins in velocity space.

Before $t_{\rm pb} \approx 300\,{\rm s}$ the enormous deceleration experienced by the ejected matter from around $\approx 70,000\,{\rm km/s}$ to $\approx 30,000\,{\rm km/s}$ (see Figure 5.18), is a consequence of the interaction of the shock with the H-envelope of the star. The CO and He rich material experiences most of the deceleration, whereas the bulk of ^{56}Ni travels at $\approx 30,000\,{\rm km/s}$ followed by the bulk of neutron rich material (traced by Tr) and the newly synthesized ^{4}He and ^{12}C. A fraction of swept up hydrogen from the envelope is partly mixed downward into the CO and He layers, which is caused by the RT unstable dense layer between the forward and reverse shock. However, the mass of hydrogen mixed into these layers is of order $\approx 10^{-5}$ before $300\,{\rm s}$. The neutrino-heated ejecta catch up with the immediate post-shock material at $300\,{\rm s}$. The resulting compression of the ejecta is reflected in the velocity space. The bulk of ^{56}Ni is moving with velocities similar to the CO and He shells, and experiences a strong deceleration as it encounters the dense shell. The growth of the RT instability in the unstable layers until $\approx 1400\,{\rm s}$ pushes the neutrino-heated ejecta to slightly larger velocities than the bulk of the CO and He layers.
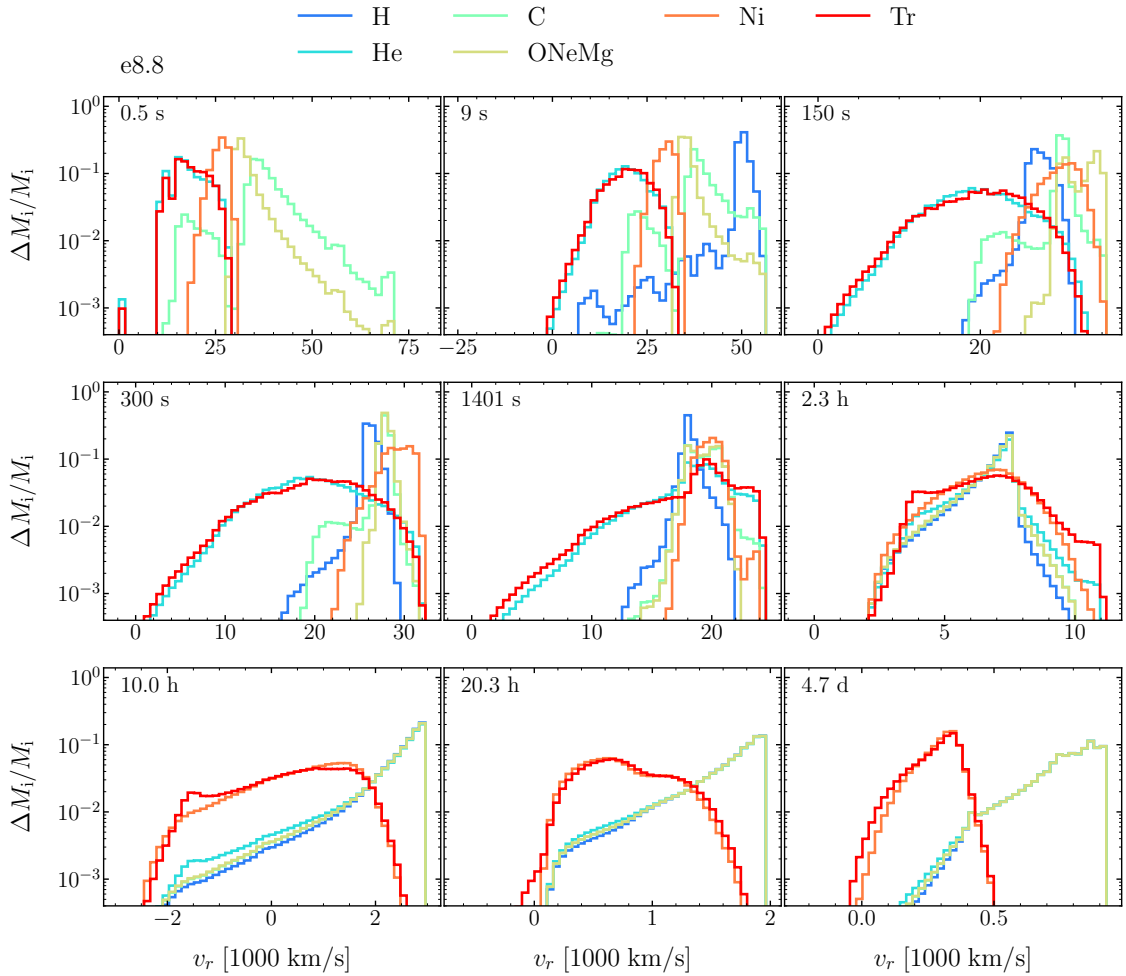
Fig. 5.18 Normalized mass distributions of chemical elements for the 3D simulation of model e8.8 in velocity space. The initial shell-like structure of the progenitor remains visible in the velocity distribution until about $t_{\rm pb} \approx 300\,{\rm s}$, where the neutrino-heated ejecta catch up with RT unstable layers just behind the shockwave. The growth of the RT instability leads to some mixing of ^{56}Ni and Tr into the carbon and helium layers of the star. However, the resulting mixing is very inefficient due to the almost spherical expansion of the ejecta. At the time of shock breakout the neutrino-heated ejecta are moving with small velocities in the inner volume of the explosion.

However, the dense shell prevents efficient mixing of ^{56}Ni and Tr (see Figure 5.19). Continuous deceleration of matter and the growth of the RT instability (until $\approx 2.3\,{\rm h}$) after bounce causes the inner ejecta to be homogeneously distributed in velocity space.

With time the reverse shock travels back in radius and strongly compresses and decelerates the neutrino-heated ejecta (see also Figure 5.8). It marks the point in time

where outward mixing in mass coordinate has basically saturated, as can be seen in the last two panels of Figure 5.19. Eventually, a significant amount of ^{56}Ni and Tr is only mixed to $M(r) \approx 1.5\,\mathrm{M_\odot}$.
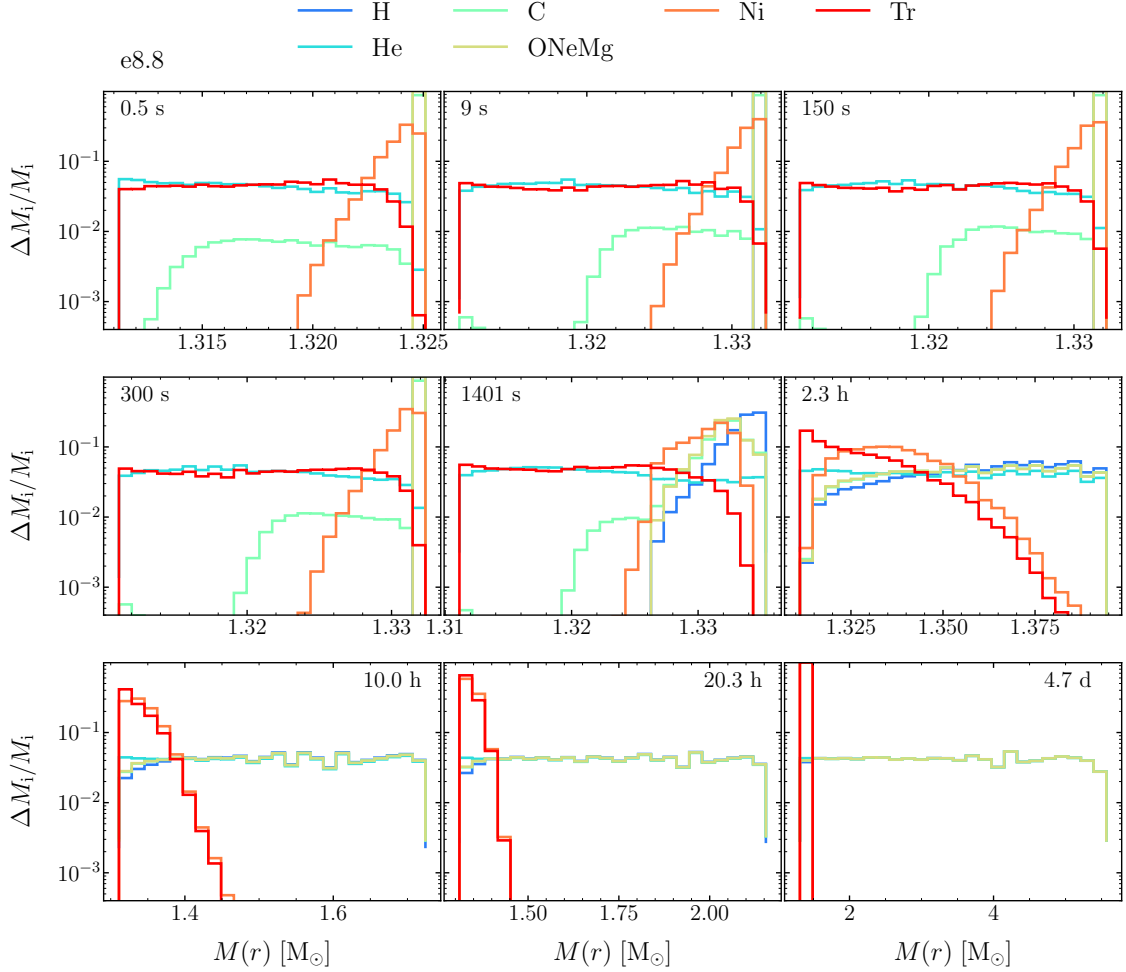

Fig. 5.19 Normalized mass distributions of elements of model e8.8 versus enclosed mass. Until $t_{\mathrm{pb}} \approx 300\,\mathrm{s}$, we see the strong compression of the CO and He shells into a thin region behind the shockwave. Note that the newly synthesized carbon and helium is uniformly distributed over the innermost ejecta. During the phase of strongest RT growth (periods before $t_{\mathrm{pb}} \approx 5\,\mathrm{h}$) we observe slight mixing of ^{56}Ni and Tr into the former CO and He shells. Also tiny amounts of carbon and oxygen are mixed down deeper into the ejecta as the reverse shock travels back in mass. At the time of shock breakout, ^{56}Ni and Tr could only be mixed to $M(r) \approx 1.48\,\mathrm{M_\odot}$ so only some $0.1\,\mathrm{M_\odot}$ outside of the former ONeMg-core.

Model z9.6

Figure 5.20 and Figure 5.21 show the mass distribution versus radial velocity and enclosed mass for the 3D simulation of model z9.6, respectively.
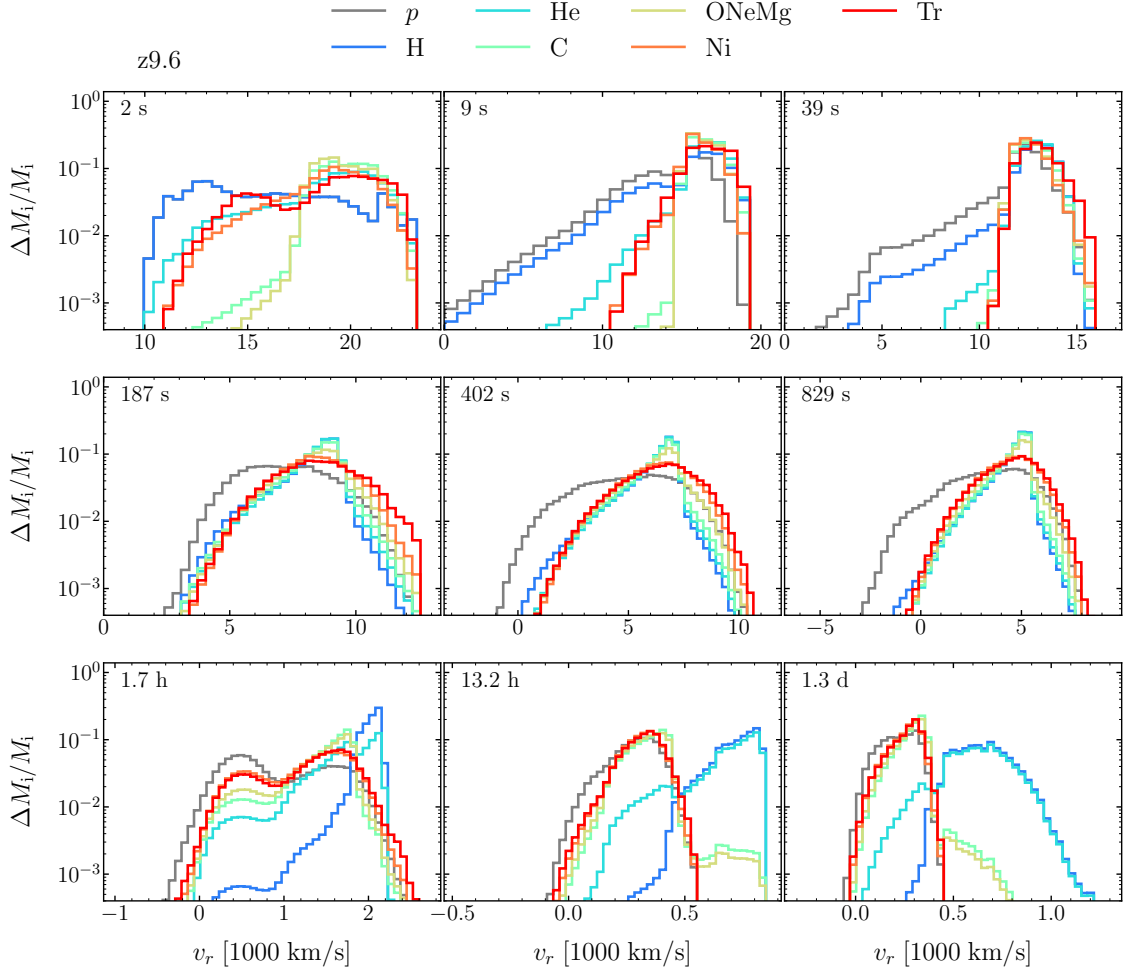

Fig. 5.20 Normalized mass distributions of elements of model z9.6 in velocity space for the same times as shown in Figure 5.12. Within the first $\approx 40\,\text{s}$ the ejecta are strongly decelerated and compressed in velocity space as they encounter the dense shell at the CO/He interface. When at $t_{\text{pb}} = 187\,\text{s}$ the shell begins to fragment, only a small fraction of the neutrino-heated ejecta can be mixed outward to higher velocities. The bulk of ^{56}Ni and Tr is strongly decelerated as the reverse shock propagates back into the central object at $t_{\text{pb}} = 829\,\text{s}$. Consequently, most of ^{56}Ni and Tr is centrally localized at $t_{\text{pb}} = 22\,\text{h}$.

Note that we separate free protons (p) and hydrogen (H) from the stellar envelope.

Different to the ECSN model, the neutrino-heated ejecta are in close proximity to the CO-shell early on which is caused partly by stronger mixing during the onset of the explosion and the acceleration of the innermost ejecta by the neutrino-driven wind. The formation of the reverse shock in the He-core, aids in a more efficient mixing of metal rich ejecta into the CO- and He-core material after $t_{\mathrm{pb}} \geq 40\,\mathrm{s}$.

As the RT instabilities grow in the unstable layers between the forward and the reverse shock, slightly more $^{56}\mathrm{Ni}$ and Tr can be mixed outwards in comparison to model e8.8. At the time of shock breakout, neutrino-heated matter is mixed only up to a volume containing $M(r) \approx 2\,\mathrm{M_\odot}$.
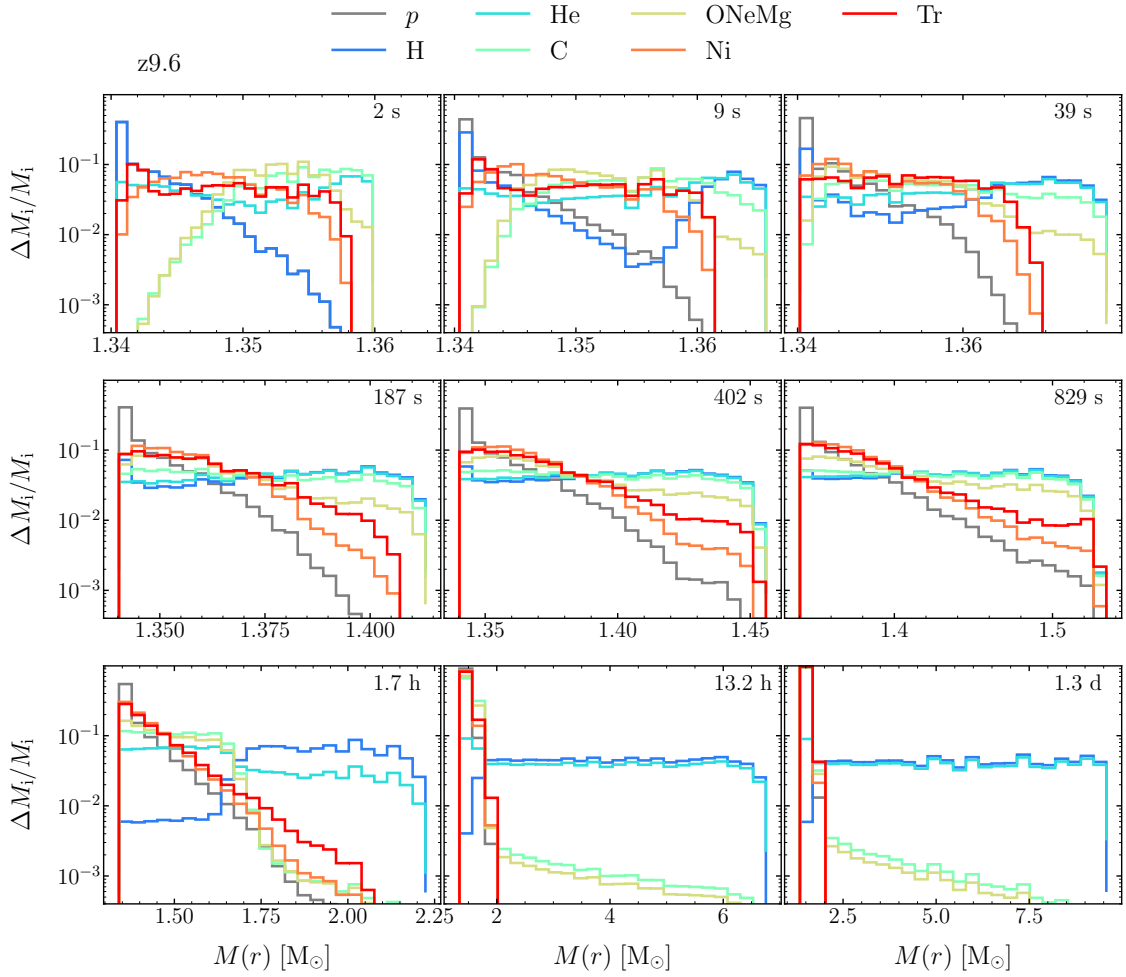
Fig. 5.21 Normalized mass distributions of elements from the 3D simulation of model z9.6 versus enclosed mass. Similar to model e8.8, early formation of the reverse shock and small initial asymmetries lead to inefficient mixing. At $t_{\mathrm{pb}} = 22\,\mathrm{h}$ the neutrino-heated ejecta remain within the $M(r) \approx 2\,\mathrm{M}_\odot$ mass coordinate which is just outside the former helium-core.

Model s9.0

Mixing in model s9.0 is highly more efficient as can be inferred from Figure 5.22 and Figure 5.23, where we show the distribution of elements in velocity space and versus mass coordinate of the 3D simulation. Convection during the onset of explosion leads to a broad distribution of elements in mass and velocity space.
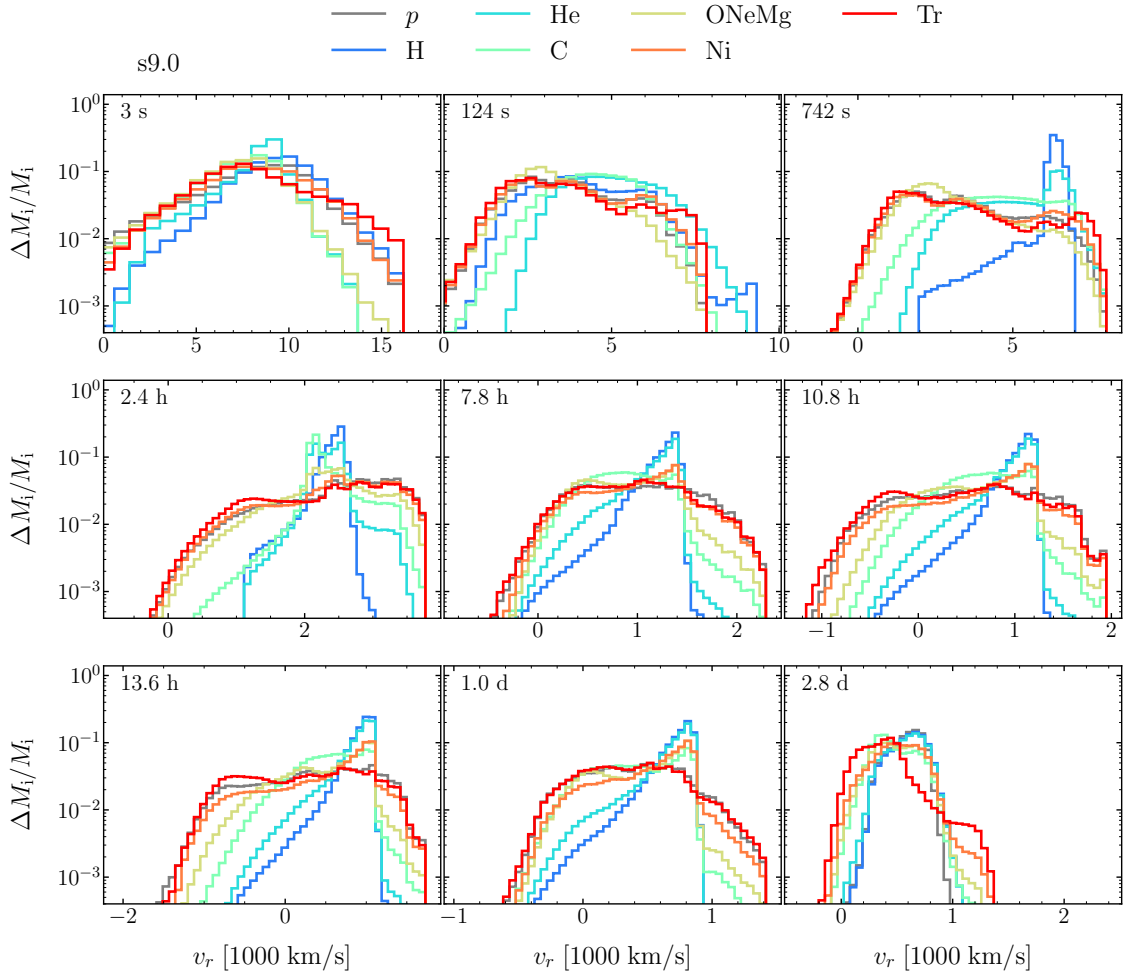
Fig. 5.22 Normalized mass distributions of elements of model s9.0 in velocity space for the same times as shown in Figure 5.15. The first $\approx 100\,\mathrm{s}$ are characterized by a bulk deceleration within the He-core. Until $\approx 2.1\,\mathrm{h}$ the reverse shock which formed at the He/H interface decelerates the inner ejecta, while large RT plumes mix a considerable amount of neutrino-heated ejecta to higher velocities. Shortly before shock breakout at $2.8\,\mathrm{d}$, we find a small amount of ^{56}Ni and Tr ($\Delta M_{\mathrm{i}}/M_{\mathrm{i}} \approx 8 \times 10^{-2}$) still propagating faster than the forward shock. This material resides in the large clump visible in Figure 5.14.

Until the forward shock reaches the He/H interface at $t_{\mathrm{pb}} \approx 124\,\mathrm{s}$, we observe an overall deceleration of matter from $20,000\,\mathrm{km/s}$ to $8,000\,\mathrm{km/s}$ (see Figure 5.22). At the same time, the reverse shock which formed at the CO/He interface, causes the deceleration of a large fraction of the metal-rich ejecta and separates them from lighter nuclei in velocity space (see panel 3 in Figure 5.22). The RT plumes mix parts of the He-core downward in mass coordinate (see panel 3 in Figure 5.23). At $t_{\mathrm{pb}} \approx 530\,\mathrm{s}$, we can observe the consequences

of the ρr^3-profile of model s9.0 around the He/H interface. It accelerated within the He-core of the star (see also Figure 5.6), which consequently lead to an acceleration of the fastest neutrino-heated matter from $\approx 7,500\,\mathrm{km/s}$ (at $t_{\mathrm{pb}} \approx 124\,\mathrm{s}$) to $\approx 8,500\,\mathrm{km/s}$ at ($t_{\mathrm{pb}} \approx 530\,\mathrm{s}$). The fastest ^{56}Ni-rich ejecta thus arrive at the reverse shock with very high velocities, faster than the mean shock velocity (visible as the velocity of the bulk of hydrogen) at the same point in time (see panel at $t_{\mathrm{pb}} \approx 530\,\mathrm{s}$ in Figure 5.22).

Over the next $\approx 400\,\mathrm{s}$ the forward shock is continuously decelerated, while the fastest neutrino-heated ejecta, which almost exclusively reside within the large RT plume described in the previous Section, remain almost constant in velocity. This enables mixing of the metal-rich ejecta also to higher mass coordinates. Only when the plume plunges deeper into the hydrogen envelope, it is decelerated as is the bulk of the ejecta. The reverse shock which formed at the He/H interface (visible in e.g. at $v_{\mathrm{r}} \approx 4,000\,\mathrm{km/s}$ at $t_{\mathrm{pb}} \approx 3,200\,\mathrm{s}$) now falls back in radius and decelerates the innermost material. However, the fast plume is unaffected by the reverse shock and continues its way through the H-envelope. At the time of shock-breakout we find a considerable amount if neutrino-heated ejecta mixed outward to high velocities and mass coordinate in strong contrast to the ECSN-like models.
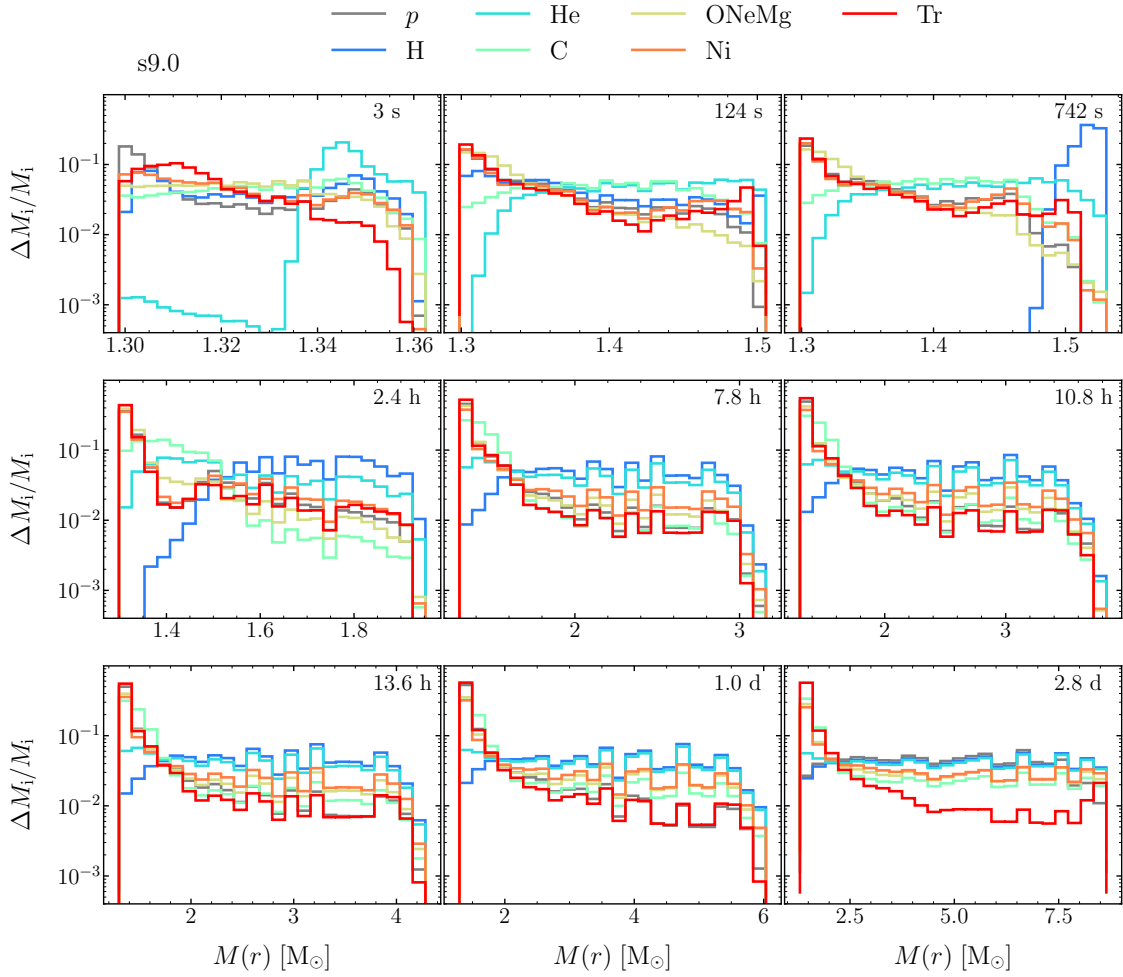
Fig. 5.23 Normalized mass distributions of elements of model s9.0 against versus coordinate. Within the first roughly $100\,\mathrm{s}$ He-layer of the star is homogeneously mixed throughout the ejecta. While the forward shock travels through the H-envelope (starting from $t_{\mathrm{pb}} \approx 127\,\mathrm{s}$) hydrogen is mixed deep into the ejecta and large amounts of ^{56}Ni and Tr are lifted to large mass coordinates. Shortly before shock breakout, we observe a significant amount of neutrino-heated material at mass coordinates above $7\,\mathrm{M}_\odot$.

Compilation of Results

Figure 5.24 shows the element distribution shortly before shock breakout for all 3D simulations as functions of radial velocity and enclosed mass. The distributions of the iron-group ejecta in the ECSN-like models (e8.8 and z9.6) have similar shapes in velocity and mass coordinate (apart from the differences that result from the different initial progenitor composition).

They are characterized by a maximum centred around 0.25×10^3 km/s and have a high-velocity tail which extends to $\sim 0.45 \times 10^3$ km/s (using $\Delta M_i / M_i = 8 \times 10^{-4}$ as a threshold value). The mixing in velocity space corresponds to mixing in mass coordinate to a maximum of $\sim 1.45\,M_\odot$ in model e8.8 and $\sim 2\,M_\odot$ in model z9.6, so only to the bottom of the respective hydrogen envelope.

Why is the mixing more efficient in model z9.6 in comparison to model e8.8 although the explosion energy and the integrated growth factors are larger in the latter? The answer can be found in inspecting Figures 5.9, 5.8 and 5.12, 5.11. Model z9.6 already shows a larger asymmetry already at the onset of the explosion. Additionally, the density profile of model z9.6 exhibits less extreme drops outside the Si/CO and CO/He interfaces than the sharp drop in density in the ECSN progenitor. This initial asymmetry triggers more and faster growth of the RT instability at the CO/He interface in model z9.6 (see Figures 5.12, 5.11) on a time scale much shorter than the growth of the RT mushrooms in model e8.8. While in model z9.6 large RT plumes are visible already at about 1000 seconds after bounce, it takes many hours for such structures to develop at the He/H interface of model e8.8 (see Figure 5.9). From this result we conclude that the extend of mixing during the supernova blast is not determined only by the linear growth factors but depends strongly on the asymmetry the explosion starts with.

In contrast to the ECSN-like models, heavy elements are mixed to large mass coordinates and velocities in model s9.0. This is facilitated by the extreme initial asymmetries at the onset of the explosion. Fast metal-rich plumes arrive quickly at the He/H interface and trigger the RT instability there, thereby transporting a significant amount of the total ^{56}Ni + Tr mass to large mass coordinates into the H-envelope. Outward mixing of intermediate-mass elements is driven by the growth of the RT instability which causes a fragmentation of the dense shells which form after the forward shock crosses the CO/He and He/H interfaces. Most importantly, the biggest plume is able to transport ^{56}Ni + Tr-rich matter to large velocities and mass coordinates. It contains about 25% of the total ^{56}Ni + Tr mass at t_{map} and carries about half of that to radii well ahead of the average radius of the shock when it reaches the stellar surface. We find that about 4% of the ^{56}Ni + Tr-rich material travels with more than $1,000$ km/s and thus far ahead of the bulk of the metal-rich matter.
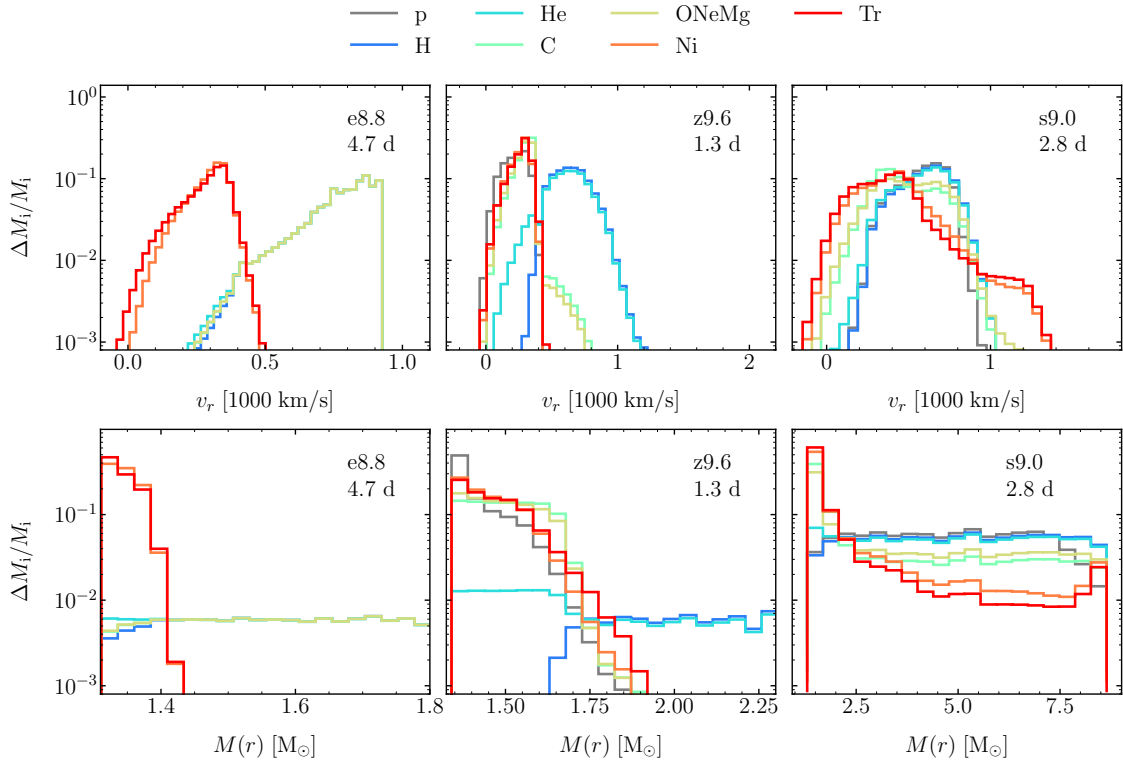
Fig. 5.24 Normalized mass distributions of elements versus radial velocity (top row) and enclosed mass (bottom row) for all our models at the time of shock breakout. We use 50 bins in velocity space covering and 30 bins in mass space, where we only show the distribution within $1.8\,\mathrm{M_\odot}$ and $2.3\,\mathrm{M_\odot}$ for models e8.8 and z9.6, respectively, since mixing of the neutrino-heated ejecta beyond these mass-shells is insignificant. For model s9.0 we consider the whole computational domain for our analysis. The ECSN-like models (e8.8 and z9.6) only mix a tiny amount of ^{56}Ni into the bottom of the H-envelope, whereas vigorous mixing in model s9.0 transports a significant amount of neutrino-heated ejecta to large mass coordinates.

5.3.4   Long-time Evolution of Compact Remnant Properties

While the supernova shock wave travels through the progenitor star, some material falls back onto the newly formed NS (e.g., Chevalier, 1989; Woosley, 1989; Zhang et al., 2008; Fryer, 2009; Wong et al., 2014). This fallback is needed to explain the observed broad range of compact remnant masses (Zhang et al., 2008; Wong et al., 2014; Ertl et al., 2019). A first episode of fallback occurs when the neutrino-driven wind abates and the wind termination shock moves back towards the PNS (Arcones et al., 2007). This period happens at early times, roughly within $\sim 10\,$s after bounce. At later times fallback is driven by the reverse shocks that originate from the acceleration and deceleration phases of the SN shock passing the composition shell interfaces. As described in Sections 5.3.2 and 5.3.1, these reverse shocks propagate backward into the central volume.

In Figure 5.25 we show the corresponding time-dependent mass accretion rates through the inner boundary of our computational grid, $|\dot{M}|(R_{\rm ib})$ (to panel), the corresponding time-integrated accreted mass $\int {\rm d}t\,|\dot{M}|(R_{\rm ib})$ (middle panel), and the evolution of the angular momentum of the PNS, $J_{\rm NS}(t)$ (lower panel), driven by the angular momentum that falls back through the inner grid boundary into the central volume and that is assumed to be accreted into the compact remnant for all of our 3D long-time simulations, starting from $t_{\rm map}$. For comparison, Table 5.2 lists the values of the PNS masses (baryonic and gravitational), total angular momenta, $J_{\rm NS}$, and spin periods, the angle between PNS spin and kick vectors, θ_{vJ}, the total amount of fallback $M_{\rm fb}$, as well as the spin period $P_{\rm NS}$ at $t_{\rm map}$ and at the end of the 3D simulations, $t_{\rm fin}$.
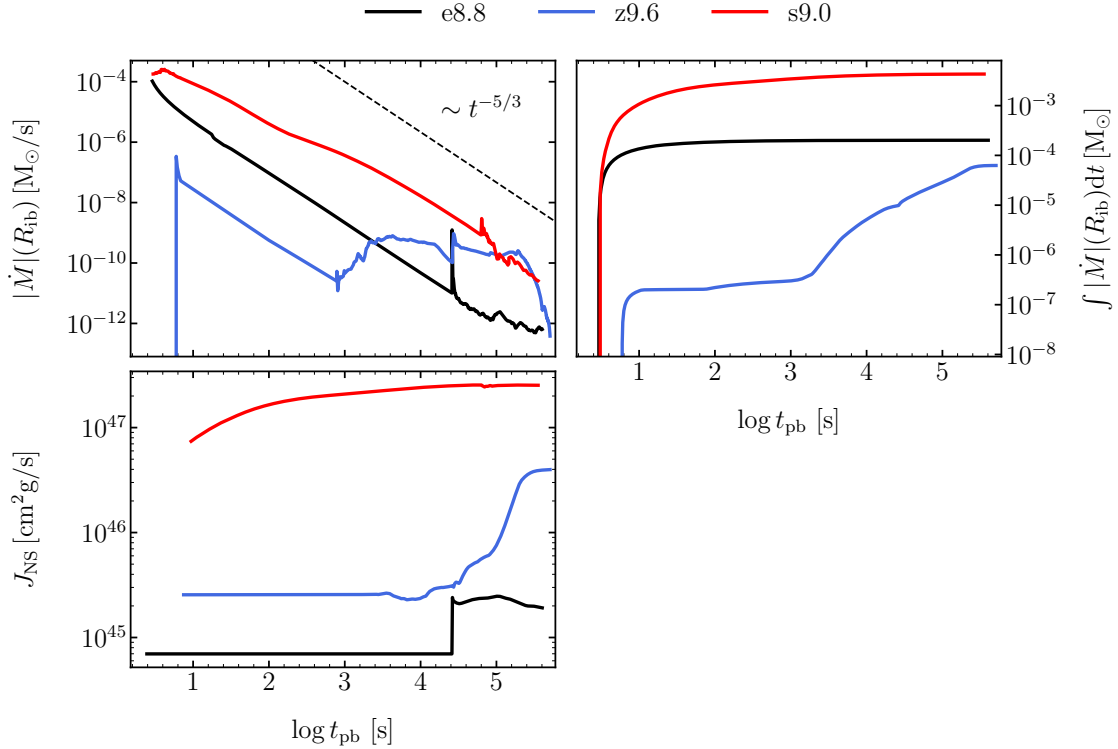
Fig. 5.25 Time evolution of the PNS mass accretion rate (top left panel), cumulative accretion of mass (top right panel), and PNS angular momentum (bottom left panel) associated with fallback during the long-time simulations of all 3D models. After some initial transition phase, which lasts longer in model s9.0 because of the 3D asymmetries of the slow ejecta in the vicinity of the PNS, all models adjust to the well-known power-law decline according to $\dot{M} \propto t^{-5/3}$ (black dashed line). This continues until the reverse shock from the outer layers in each model has propagated inward and reaches the inner boundary of the computational grid at radius R_{ib}. In models e8.8 and s9.0 early fallback clearly dominates, whereas in model z9.6 the reverse shock contributes significantly to the total fallback mass. Angular momentum carried through R_{ib} by the infalling matter is assumed to change the initial angular momentum of the PNS. In models e8.8 and z9.6 late fallback associated with the reverse shock causes the main effect on J_{NS}, whereas in model s9.0 the total angular momentum rises most steeply at early times when some of the highly asymmetric ejecta fall back onto the PNS.

During the first fallback episode, i.e., during the first tens of seconds, all three models behave differently because of their different evolution during the neutrino-wind phase. In model e8.8 the forward shock is very fast and the slower neutrino-driven wind (adopted from a parametric 1D simulation; see Fig. 5.2) expands freely behind the shock without deceleration and without developing a reverse shock. After the termination of the neutrino-

driven wind at $\sim 2.5\,$s post bounce, fallback sets in but the mass accretion onto the PNS declines steeply, because the ejecta move rapidly outward, evacuating the surroundings of the compact object.

In model z9.6 a similar situation applies, but the faster and more long-lasting neutrino-driven wind (adopted from a self-consistently computed PNS cooling model; see Fig. 5.2) is stronger and evacuates the neighbourhood of the PNS even more extremely than in model e8.8. However, a reverse shock forms when the forward shock passes the CO/He interface and decelerates, while at the same time the neutrino-driven wind pushed from behind and compresses the postshock matter into a dense shell. This reverse shock moves inward within a few seconds and creates the short accretion spike at $\sim 8\,$s. The accretion peak decays within only a second when a reflected wave sweeps the medium surrounding the PNS outward again. Model z9.6 displays the lowest mass accretion of all three models. In contrast, model s9.0 has by far the highest mass accretion through the inner grid boundary since its neutrino-driven wind is very weak. Therefore the PNS is not surrounded by a large low-density wind bubble but instead accretion downflows and rising plumes of neutrino-heated matter continue to coexist in the vicinity the PNS for many seconds of postbounce evolution. The mass accretion rate during the early fallback phase exhibits a correspondingly high plateau between $\sim 3\,$s and $\sim 10\,$s.

Models e8.8 and z9.6 reach the asymptotic scaling $\dot{M} \propto t^{-5/3}$ (Chevalier and Klein, 1978; Zhang et al., 2008; Dexter and Kasen, 2013; Wong et al., 2014) already after about $10\,$s, and it persists until the late fallback associated with the reverse shocks sets in at about $1000\,$s in z9.6 and at about $9\,$h in e8.8. In contrast, model s9.0 displays clear deviations from the $-5/3$ power-law until roughly $1\,$h because of large-scale asymmetries in the fallback material. Late accretion due to the reverse shock from the He/H interface is triggered only after $\sim 16\,$h.

With an integral around $5 \times 10^{-3}\,\mathrm{M}_\odot$ model s9.0 has the highest total fallback mass (middle panel of Fig. 5.25), the other two models possess at least 10 times lower values. In all of the three cases the fallback mass is too low to have any significant impact on the PNS mass or kick (see Table 5.2).

However, the asymmetric fallback of matter also carries angular momentum through the inner grid boundary. Although very little mass is accreted, matter that falls back from large radii can carry appreciable amounts of angular momentum, accounting for the dominant contribution to the total PNS angular momentum in all of our simulations. In model s9.0 the angular momentum of the PNS increases by more than a factor of 10 to $10^{47}\,\mathrm{g\,cm^2 s^{-1}}$ within the first $10\,$s of fallback accretion. It further grows continuously by another factor 2.5 until the 3D simulation was stopped over $4\,$d later. The final angular

Table 5.2 Overview of final PNS properties of our 3D models at the time of shock breakout.

Model	t_{map} [s]	$J_{\mathrm{NS}}^{\mathrm{map}}/10^{45}$ [cm²g/s]	θ_{vJ} [°]	M_{map} [M⊙]	M_{g} [M⊙]	$P_{\mathrm{NS}}^{\mathrm{map}}$ [s]	t_{fin} 10^5 [s]	$J_{\mathrm{NS}}^{\mathrm{fin}}/10^{45}$ [cm²g/s]	$\theta_{vJ}^{\mathrm{fin}}$ [°]	M_{fb} [10^{-3} M⊙]	M_{fin} [M⊙]	$M_{\mathrm{g}}^{\mathrm{fin}}$ [M⊙]	$P_{\mathrm{NS}}^{\mathrm{fin}}$ [s]
e8.8	0.47	0.70	90.0	1.311	1.197	10.58	4.5	1.77	114.3	0.316	1.311	1.197	4.13
z9.6	1.44	2.55	45.4	1.340	1.221	2.93	5.0	40.2	163.6	0.065	1.340	1.221	0.19
s9.0	3.14	8.05	31.3	1.351	1.230	0.94	4.1	253.2	101.7	4.999	1.356	1.234	0.03

Notes: The left part of the table (columns 2–7) lists the properties of the PNS at t_{map} (see also Table 4.2). The right part of the table (columns 8–13) gives the corresponding final PNS properties at the end of our long-time simulations, t_{fin}. $J_{\mathrm{NS}}^{\mathrm{fin}}$ is the final angular momentum, $\theta_{vJ}^{\mathrm{fin}}$ the angle between spin and kick vectors, M_{fb} the total fallback mass, M_{fin} the final baryonic mass, $M_{\mathrm{g}}^{\mathrm{fin}}$ the gravitational mass and $P_{\mathrm{NS}}^{\mathrm{fin}}$ the spin period, assuming a PNS radius of 12 km.

momentum of the PNS is more than 30 times bigger than at 3 s after bounce. In models e8.8 and z9.6 the PNS angular momentum begins to change only when the late reverse shocks reach the center and anisotopic structures begin to be accreted. This amplifies the initial angular momentum of the PNS in z9.6 still by a factor of 15 (see bottom panel in Figure 5.25). In contrast, in model e8.8 the total effect is much more modest because of the low mass associated with the late fallback and the weak asymmetry of the explosion in this case.

Nevertheless, also in model e8.8 the spin period estimated for a PNS with 12 km radius decreases from $\sim$10 s at 0.5 s after bounce to a final value of nearly 4 s (Table 5.2). For z9.6 the spin period shrinks from 2.9 s at $t_{\mathrm{map}} = 1.44$ s to finally 0.19 s, and for s9.0 the final period is as low as 0.030 s, whereas it had been 1.07 s before the fallback. before the fallback.

The PNS spins seem to be randomly oriented relative to the PNS kick directions, i.e., the angles between PNS spin and total kick vectors, θ_{vJ}, do not show any preference for spin-kick alignment, neither at early times nor days later when the fallback was complete and the simulations were terminated. This is not unexpected and it is in line with previous findings (Wongwathanarat et al., 2013; Müller et al., 2019). To date there is no suggestion based on well accepted physics (i.e., without invoking uncertain ingredients or extreme physical assumptions) for a convincing mechanism that could provide spin-kick alignment. Even if such alignment were achieved during the first seconds of the explosion, when ejecta and PNS are still in contact through hydrodynamical and gravitational forces and the PNS is kicked by anisotropic neutrino radiation, it is very hard to imagine how this initial alignment could not be overruled by the stochastic effects of the later fallback and its dominant influence on the PNS spin. It might require very rapid progenitor rotation, possibly very strong magnetic fields, to impose a preferred direction for the explosion, correlating PNS recoil acceleration and later spin-up by angular momentum accretion of the PNS associated with fallback.

5.3.5 Effect of β-Decay

In order to estimate the dynamic effect by the heating due to the decay of radioactive ^{56}Ni, we recomputed the e8.8$_{10}^{\text{1D}}$ model without the contribution of ^{56}Ni-heating.

We show in Figure 5.26 the density versus radial velocity at 100 days post-bounce of our model with ^{56}Ni-heating in comparison to the model without the additional energy input. The central located ^{56}Ni heats the surrounding and thus accelerates the hydrogen envelope to slightly higher velocities. The effect, however, is not significant, which stems from the very small amount of ^{56}Ni produced in ECSN ($\approx 10^{-4}\,\mathrm{M_\odot}$). According to Nadyozhin (1994) the total energy available in the decay from ^{56}Ni to ^{56}Fe is given by

$$E_\beta = 1.885 \times 10^{50}\,\frac{M_{\text{Ni}}}{M_\odot}\,[\text{erg}]. \tag{5.15}$$

thus the available energy is of order $\approx 10^{48}\,\text{erg}$ and a few magnitudes smaller than the explosion energy.
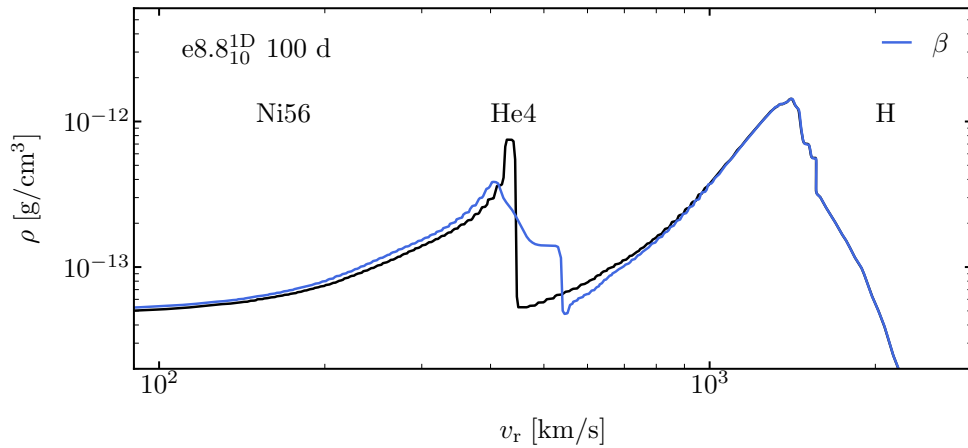

Fig. 5.26 Density versus velocity for the spherical-symmetric $e8.8_{10}$ at 100 days after bounce. Indicated are in blue a model with the calculation of the β-Decay and in black one without. Matter at the ^{56}Ni/H boundary is pushed to slightly higher velocities.

Since the amount of ^{56}Ni produced in model z9.6 (compare Table 4.3) is almost one magnitude smaller than in model e8.8$_{10}$ we do not expect a large contribution of radioactive heating to the late time dynamics of this progenitor. Also a similar mass of ^{56}Ni as found in model e8.8$_{10}$ is produced in model s9.0. Thus, the overall effect of the β-decay of ^{56}Ni and ^{56}Co will be of the same magnitude as found in model e8.8$_{10}$. However, heating within the large RT plume may lead to an expansion of the bubble at late times. This effect will be investigated in future studies.

Comparison to 2D Simulations

In the following we access the dependence of the ejecta morphology and episodes of mixing in our long-time simulations on the chosen symmetry.

As already shown in Section 4.2.3, the 2D simulation of model e8.8 behaves remarkably similar to the full 4π-simulation. Consequently, we find only small differences in the morphology of the ejecta and efficiency of mixing at the time of shock breakout in these simulations. Affirming this, we show in Figure 5.27 slices of the ^{56}Ni + Tr mass fraction, density, radial velocity and entropy for both simulations at the time of shock breakout.

In all shown quantities both simulations show striking similarities. The morphology of the neutrino-heated ejecta is characterized by its overall sphericity. The growth of hydrodynamical instabilities also seems to have proceeded basically independent of the chosen symmetry, as the plumes at the outer boundary of the bulk of ^{56}Ni + Tr-rich material have similar shapes and are similarly frequent.

Therefore, mixing in mass and velocity coordinate is also basically independent of the chosen symmetry as we show in Figure 5.28. While, in velocity space, we find tiny differences in the distributions, mixing in mass coordinate, however, is not affected by the chosen symmetry.

We therefore conclude that mixing due to hydrodynamic instabilities is evenly well captured in the axis-symmetric simulation of model e8.8.

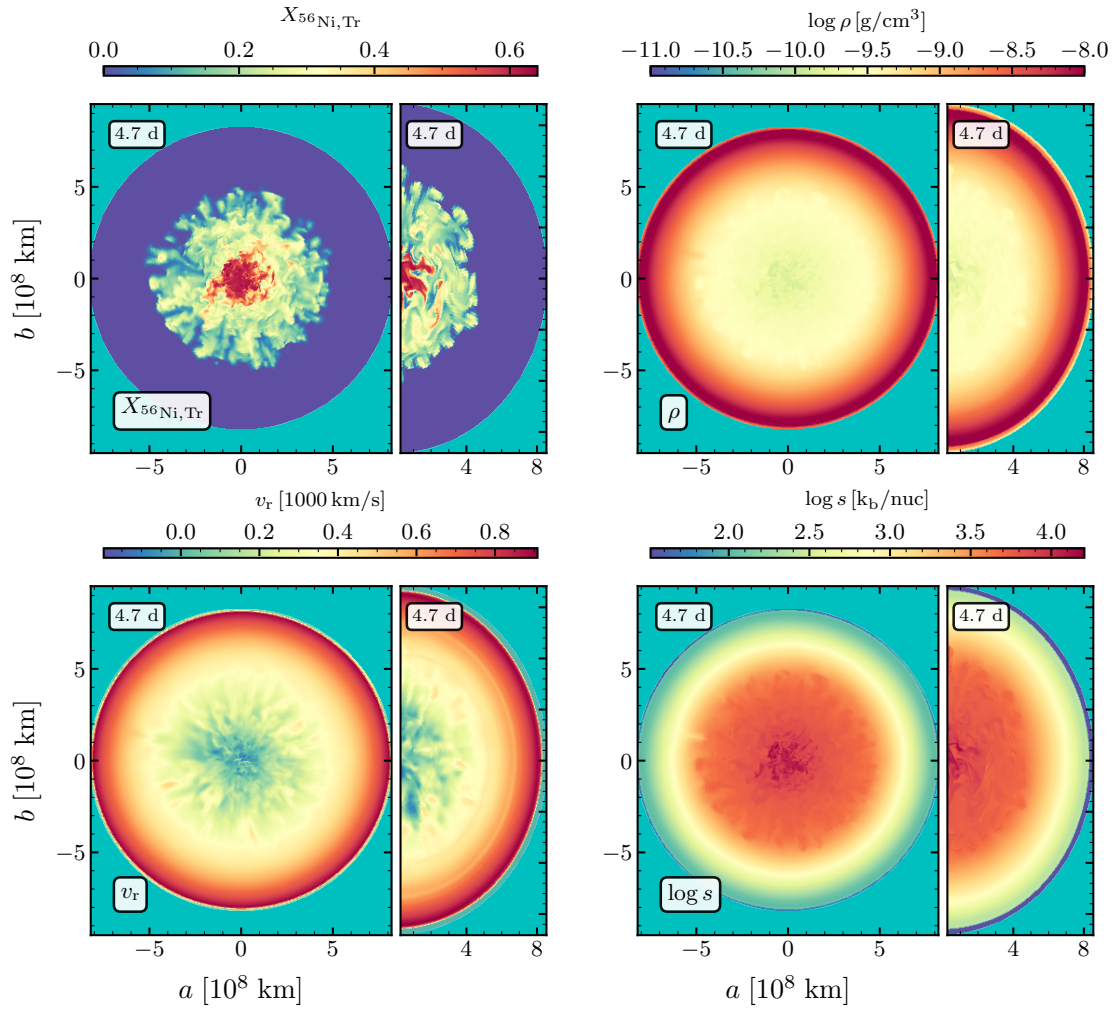Fig. 5.27 Slices of the 2D (right part of panels) and 3D (left part of panels) simulation of model e8.8 shortly before shock breakout showing the ^{56}Ni + Tr mass fraction (top left), density (top right), radial velocity (lower left) and entropy (lower right). The cyan region marks the surrounding in which the star is embedded. Both simulations show striking similarities at the time of shock breakout.
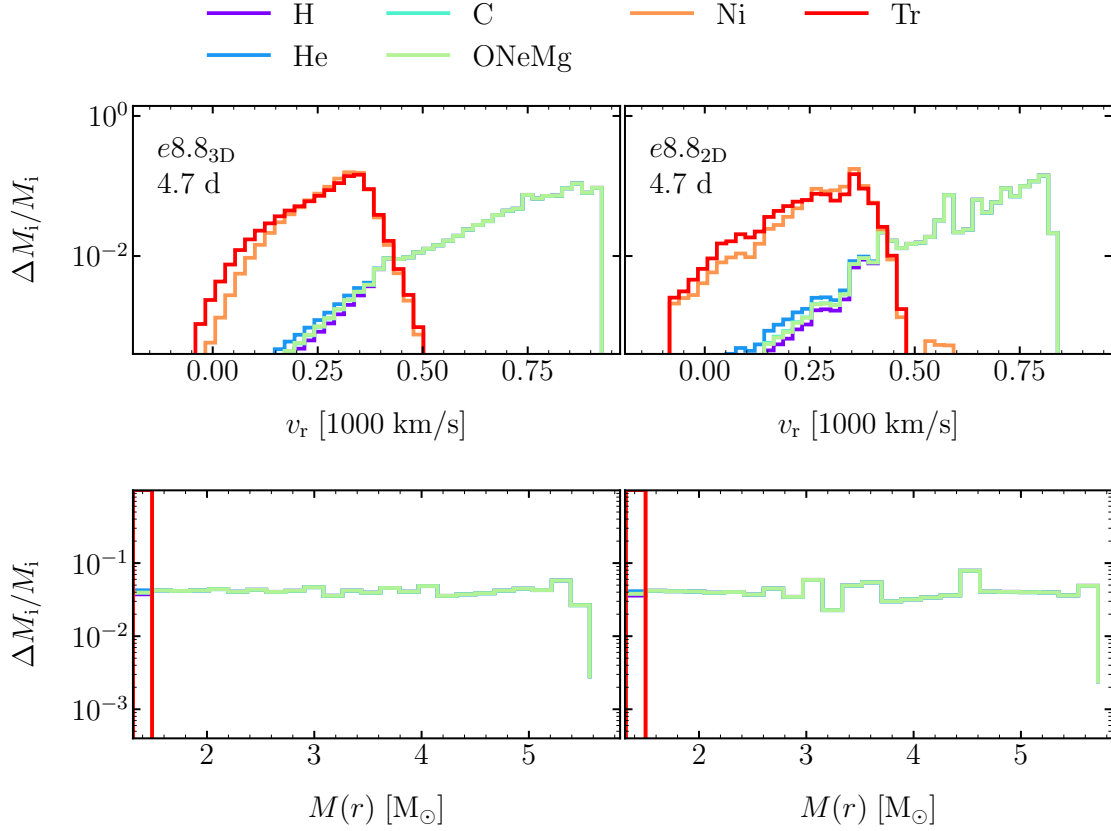
Fig. 5.28 Normalized mass distributions of the 2D (right panels) and 3D (left panels) simulation of model e8.8 shortly before shock breakout. In velocity space, the 2D simulations show only tiny differences to the 3D simulation. The distribution of the 3D model seems slightly smoother which may be attributed to a different radial resolution at that point in time. In mass coordinate, the results of both simulations are basically indistinguishable.

5.4 Dependence on the Explosion Energy

Inspecting Figure 5.29, we find that the bulk of ^{56}Ni resides at low velocities of $\sim 0.17 - 0.40 \times 10^3$ km/s, increasing with explosion energy roughly as $v_r \sim \sqrt{E_{\mathrm{exp}}}$. For larger explosion energies the downward mixing (to smaller velocities) of lighter elements also seem to be more efficient, but the effect is small and affects only $< 1\%$ of the respective elements. For lower explosion energy the mass of ^{56}Ni + Tr experiencing fallback ($v_r < 0$) grows.

The mixing in velocity space corresponds to a distribution of ^{56}Ni and Tr to a maximum mass coordinate of $1.37 - 1.436\,\mathrm{M}_\odot$ (see Figure 5.30) also increasing with explosion energy,

using $\Delta M/M = 4 \times 10^{-4}$ as a threshold value. Note that the 4.49 M$_\odot$ of the hydrogen envelope of the progenitor initially extended from 1.34 M$_\odot$ to 5.83 M$_\odot$, thus mixing only affects the innermost part of the envelope.
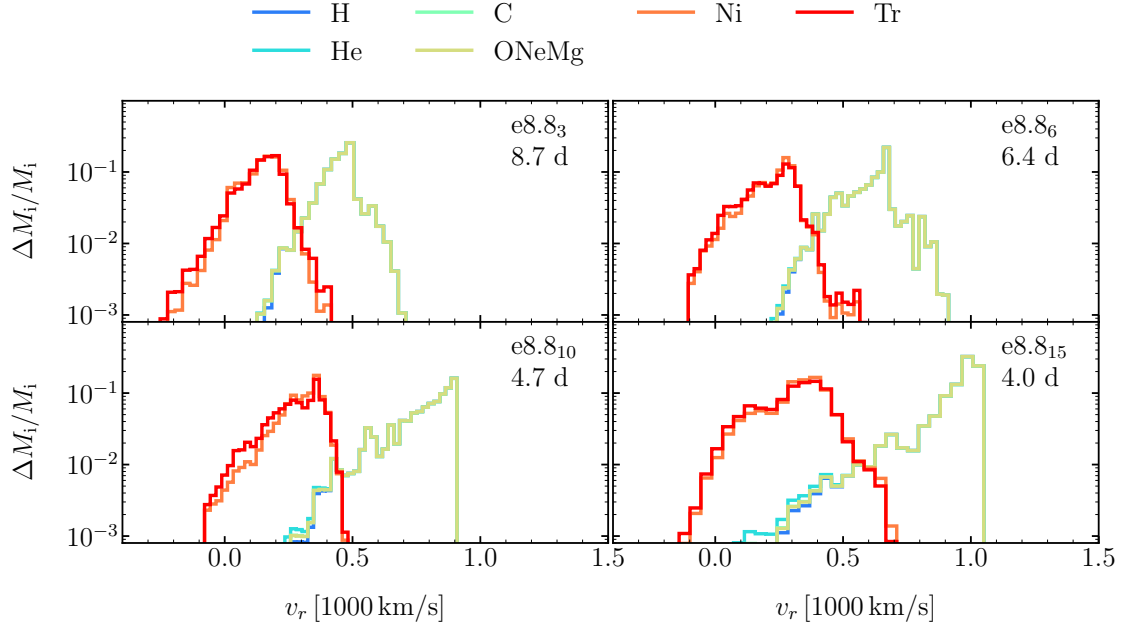

Fig. 5.29 Normalized mass distributions chemical elements of long-time 2D simulations of model e8.8 (based on the calibrations listed in Table 4.1) at the time of shock-breakout as a function of radial velocity. Maximum velocities, and thus also the velocities of the bulk of ^{56}Ni and Tr, scale roughly with $\sqrt{E_{\mathrm{exp}}}$ leading to slightly enhanced mixing for more energetic models (see also Figure 5.30).

The increased efficiency in mixing is mainly caused by two reasons. First, the deceleration of the forward shock at the core/envelope boundary is somewhat stronger for higher energetic models. Inversions of the pressure gradient in the post-shock regime are thus larger and lead to larger amplification factors at this interface (see 5.2). Second, the formation of the reverse shock is delayed in models with higher explosion energy. Later reverse shock formation increases the time the mixing processes act on the matter, and thus lead to more efficient mixing (see also Utrobin et al. 2019).

As the iron core progenitors are exploded self-consistently, their explosion energy is fixed within our framework. Drawing direct connections between the amount of mixing and the explosion energy can therefore not be done. Comparing the z9.6 model with the electron-capture model, which both have similar explosion energies, however, suggests that the influence is minor. Decisive for the amount of nickel mixing is the progenitor structure

and initial asymmetries after shock revival. This view is supported by the strong mixing apparent in model s9.0 that has comparable explosion energy as well. The initial velocity and density perturbations combined with the strong acceleration and deceleration of the forward shock in the envelope of the progenitor yield high growth rates of RT instability over a larger space in mass coordinate.
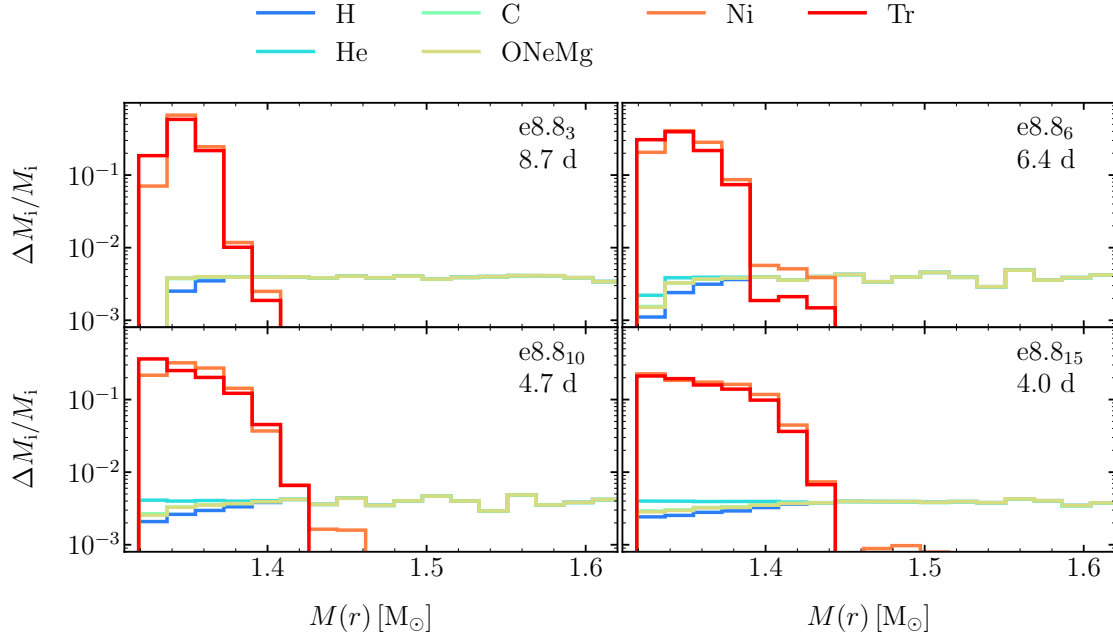

Fig. 5.30 Normalized mass distribution of the 2D simulations of model e8.8 (based on the calibrations listed in Table 4.1) at the time of shock-breakout as a function of enclosed mass. Models with larger $E_{\exp}$ show slightly more efficient mixing of iron-group material.

5.5   Comparison to Previous Studies

Previous studies also focused on the explosion properties of CCSNe of low-mass iron and ONeMg core progenitors. The study by Radice et al. (2017) simulated the onset of the explosion of model e8.8$_n$, z9.6 and s9.0 in 2D with varied microphysics. They found for model e8.8$_n$ an explosion with an energy of up to 1.8×10^{50} erg, which is about a factor of two higher than obtained for the same $8.8 \, \mathrm{M}_\odot$ star by Kitaura et al. (2006); Janka et al. (2008); Hüdepohl et al. (2010); Fischer et al. (2010) and von Groote (2014). Consistently, their 2D simulations yielded explosion energies for models z9.6 and s9.0 that were $\sim 50\%$ higher than in our simulations namely 1.2×10^{50} erg and 0.7×10^{50} erg, respectively, their 3D calculations of model s9.0 even 1.0×10^{50} erg (Burrows et al., 2019).

Müller et al. (2019) focused on the onset of the explosion in helium core progenitors from binary evolution and low-mass single stars also including model z9.6. They found a slightly higher explosion energy of model z9.6 of around 1.3×10^{50} erg at the end of their simulation. Moreover, their explosion energy still seems to grow fairly steeply when they stopped their simulation.

However, Müller et al. (2019) used an approximative neutrino transport treatment ("fast multi-group transport", FMT) with simplified neutrino interactions, and their explosion energies should therefore be taken with a grain of salt. The reason why Radice et al. (2017) and Burrows et al. (2019) obtained consistently more energetic explosions than in our VERTEX-PROMETHEUS simulations is unclear to us, in particular because their FORNAX code is claimed to possess neutrino physics that is compatible with that of VERTEX-PROMETHEUS.

We note that, due to the higher explosion energies found in the studies of other groups, the final PNS masses there are smaller than ours in general. A more energetic explosion drives a stronger wind from the PNS, which carries away mass from its surface or reduces further accretion. For example Müller et al. (2019) found the PNS mass of model z9.6 to be 1.35 $M_\odot$, close to ours, and Burrows et al. (2019) determined the PNS mass of model s9.0 to be 1.342 $M_\odot$, whereas we get 1.35 $M_\odot$. The explosion energies and PNS masses of Radice et al. (2017) and Burrows et al. (2019) are not only in conflict with ours but also with other previous studies as for example Kitaura et al. (2006); Janka et al. (2008); Hüdepohl et al. (2010); von Groote (2014) for model e8.8 and Glas et al. (2019) for model s9.0. These studies consistently attain lower explosion energies with around 10^{50} erg for model e8.8 and around 0.4×10^{50} erg for model s9.0, respectively.

Concerning the long-time evolution of the explosion of low-mass CCSNe progenitors, Müller et al. (2018) followed the expansion of the supernova shock from its initiation until shock breakout in an ultra-stripped helium star (he2.8) with a helium core mass of 1.49 $M_\odot$, which is structurally similar to model z9.6. The supernova runs (s2.8) of Müller et al. (2018) also explode with energies only slightly higher than our simulation of model z9.6, and comparing the maximum mass coordinate of the neutrino-heated ejecta they exhibit a similar extend of mixing. In their simulation a small fraction of the total iron-group material is mixed to the edge of the helium core, of the progenitor star, as it is the case also in our model z9.6, where we find a small fraction of the total neutrino-heated ejecta to be mixed out to $M(r) \sim 1.8 \, M_\odot$.

Other studies such as those of Kifonidis et al. (2006), Hammer et al. (2010), Wong-wathanarat et al. (2015) and Orlando et al. (2019) also performed simulations of the long-time evolution of CCSNe after shock-revival based on 2D/3D initial data. These

studies, however, focused on more massive RSG progenitors and BSG progenitors that stand as a proxy for Sanduleak -69 202, the progenitor of SN1987A. Kifonidis et al. (2006) and Hammer et al. (2010) used a 15 $M_\odot$ blue supergiant, while Wongwathanarat et al. (2015) explored various models from 15-20 $M_\odot$. Orlando et al. (2019) use two BSG models with 16.3 $M_\odot$ and 18.3 $M_\odot$, respectively. While the studies of Kifonidis et al. (2006); Hammer et al. (2010); Wongwathanarat et al. (2015) used initial data from explosion simulations, Orlando et al. (2019) initiated the explosion by injecting energy near the IG/Si interface and parametrized the deformation of the outgoing shockwave in order to mimic the nonradial instabilities at the onset of explosion and to reproduce the observed morphology SN1987A. Long-time 3D supernova simulations for studying mixing and explosion asymmetries by Ellinger et al. (2012) and Joggerst et al. (2009); Joggerst et al. (2010) started their runs of zero metallicity, low-metallicity and solar metallicity 15 $M_\odot$ and 25 $M_\odot$ progenitors from spherically symmetric explosions.

These more massive progenitors differ strongly in their ρr^3-profiles when compared to our ECSN-like models. Only model s9.0 exhibits similar structural features (e.g. a significant variation of the density gradient at the He/H interface) similar to the RSG models of Wongwathanarat et al. (2015). Consequently, all higher-mass models of the mentioned studies evolve considerably differently from the ECSN-like progenitors presented here. Larger amplification factors at the composition interfaces and a more extended region of instability lead to the growth of large RT plumes, which are absent in models e8.8 and z9.6. Model s9.0, however, behaves more similar despite the smaller ZAMS mass and considerably lower explosion energy. Although the previous studies are tuned to give around 10^{51} erg of explosion energy (e.g. to be compatible with observations of SN1978A), we find a similar efficiency of mixing at the end of our simulation, facilitated by the strongly asymmetric onset of the explosion and the growth of strong secondary RT instability at the composition interfaces triggered by the initial ejecta asymmetries.

Chapter 6

Summary and Discussion

In the following we summarize our results, discuss their implications for current knowledge about the long-time evolution of CCSNe and supernova remnants and give an outlook of future work. We remind the reader of the questions asked in the beginning and the aims this work tries to achieve, namely

- What are the differences in the initiation of the explosion of low-mass Fe-core end ONeMg-core progenitors?

- What is the influence of each progenitor structure on the long-time evolution of the explosion? In particular, what is the influence on the formation of reverse shocks and the efficiency of mixing of neutrino-heated material?

- Are low-mass progenitors of CCSNe able to produce highly mixed ejecta in a similar fashion as their more massive counterparts as found in previous studies?

- How do the properties of the compact remnant change on long time-scales due to fallback of matter? Are there significant changes to the remnant's mass, kick or angular momentum?

6.1   Onset of the Explosion

In this study we presented the results of two- and three-dimensional simulations of CCSNe connecting the seconds after bounce, shock revival and shock breakout. We used three low-mass progenitors, two RSGs that formed an iron-core at the end of their life (z9.6, s9.0) and a newly explored ECSN progenitor (e8.8).

The explosion of the e8.8 in one-, two- and three dimensions was initiated by imposing suitable values for neutrino luminosities and mean energies at the inner grid boundary

located at a finite, time-dependent radius. Neutrino transport and neutrino-matter inter-
actions were treated by the RbR gray neutrino transport scheme of Scheck et al. (2006),
including a improvement of the prescription for neutrino source terms.

The immediate post bounce evolution of the iron-core models was simulated with
Vertex employing a fully self-consistent neutrino transport scheme. A detailed analysis of
the first second of evolution of model z9.6 is given in Melson et al. (2015b), while simulation
of model s9.0 were first presented in Melson et al. (2019). We showed, for all models, the
evolution of the explosion energy, morphology of the ejecta, hydrodynamic and neutrino
induced neutron star kicks and evaluated the angular momentum transport onto the PNS.

Addressing the question if there are clear differences between the onset of the explosion
of a core-collapse SNe from iron core or ONeMg core progenitors, we find characteristic
and discerning evolution during the first $\sim 1\,\mathrm{s}$ after core bounce. We confirm the common
behavior of ECSNe already presented in e.g. Kitaura et al. (2006); Gessner and Janka
(2018). The early decline of the mass accretion rate leads to early explosions and fast shock
expansion at the edge of the ONeMg core even in one-dimension. Shock trajectories are
fairly independent of the chosen geometry, while the almost spherical expansion produces
only small neutron star kicks of the order of a few km/s. In consequence, convective
motions in the multi-dimensional simulations are also too weak and short-lasting to enable
efficient mixing of neutrino-heated matter early on.

We observe a similar behaviour in model z9.6 concerning the efficiency of mixing. Due
to the more accurate neutrino transport, however, we can investigate the neutrino induced
PNS kick which dominates the hydrodynamic kick in this model due to a strong and
persistent LESA. If LESA is a common phenomenon in CCSNe, it could, especially in
cases where the is minimal asymmetry in the ejecta, lead to a lower limit of PNS recoils at
birth of some 10-20 km/s if the hydrodynamic and neutrino induced kick directions align.
This value is still below the critical value of $\sim 50\,\mathrm{km/s}$ which is roughly the escape speed
of most globular clusters (Podsiadlowski et al., 2005). If neutron stars would have natal
kick velocities above this critical value, most clusters could not retain the observed number
of neutron stars in them. Note that we only consider single stars in this work.

Different from the ECSN-like progenitors, model s9.0 develops strong asymmetries
during the onset of the explosion. Thus, the hydrodynamic kick is of the same order as the
neutrino induced PNS kick and although the hydrodynamic kick is misaligned with the
anti-LESA direction, the total kick sums up to $\sim 41\,\mathrm{km/s}$, which is only a factor of ~ 4
smaller than the assumed velocity of the CRAB pulsar of $\sim 160\,\mathrm{km/s}$ (Hester, 2008).

The initial spin periods of the ECSN-like progenitors are high and of the order of seconds. Due to the longer and more asymmetric mass accretion onto the PNS in model s9.0 the initial spin period is 0.94 s and thus considerably faster than the other two models.

6.2   Long-time Evolution

When mass accretion subsides in all models and explosion energies and kick velocities begin to saturate we map the final state of our explosion simulations into Prometheus-HOTB. This is achieved by excising the inner almost spherically symmetric regions of the previous simulations and replacing them by a suitable point mass. By incorporating the neutrino-driven wind and setting the radius of the inner boundary below the sonic point we guarantee a seamless transition between the codes.

At the time when we continue the simulations of the explosions the forward shocks of all three dimensional models has traveled already beyond 10^4 km. In order to aid our understanding of the formation of reverse shocks and growth of RT instability in the multi-dimensional models we appealed to spherically symmetric simulations with the same setup starting from angle-averaged initial data of the 3D post-bounce simulations.

The extremely steep density gradient at the core/envelope boundary in model e8.8 leads to rapid expansion of the shock until it crosses the He/H interface. Thereafter, a featureless ρr^3-profile leads to an untroubled propagation of the shock which is continuously decelerated. The strong deceleration of the forward shock leads to the formation of a dense shell, below which a reverse shock forms already at $t_{\rm pb} \sim 1\,{\rm s}$. In model z9.6 we observe the formation of a reverse shock also fairly early at $t_{\rm pb} \sim 100\,{\rm s}$ after the shock crossed the CO/He interface. The successive expansion of the shock, however, is untroubled due to the monotonic ρr^3-profile. The shock propagation in model s9.0 is characterized by two phases of deceleration and acceleration at the CO/He and He/H interfaces. After the supernova shock crosses the He/H interface we observe the formation of a strong reverse shock.

Every time the shock decelerates it sends pressure waves back into the ejecta creating the necessary crossing signs of the pressure and density gradients to facilitate the growth of the RT instability. Using a linear stability analysis we estimate the amplification factors of some initial perturbations.

In the ECSNe-like models we find large amplification factors close to the CO/He interfaces where the density gradient within the progenitor is steepest. However, the RT unstable regions occupy only a small range in mass coordinate. In contrast, model s9.0 shows a more typical position and amplitude of the amplification factors when compared to other RSGs reported in the literature. We find the largest amplification factors around

the He/H interface and minor contributions at the CO/He interface. This is a first hint at the second question asked in the beginning, namely, if there is a characteristic feature that discerns the long-time evolution of ECSN-like from "normal" CCSNe.

In 3D we observe the complicated propagation of the neutrino-heated ejecta, their interaction with dense shells and reverse shocks and their fragmentation due to the growth of instabilities. In the case of the ECSN-like progenitors the dense shells form early during the evolution. In the extreme case of the e8.8 the extreme deceleration of the shock at the core/envelope boundary compresses the post shock material already at 170 ms. The resulting dense wall is almost impermeable for the neutrino heated ejecta. When they catch up with the dense shell they are strongly decelerated and only small fragments of ^{56}Ni- and Tr- rich material can penetrate the wall. The growing RT instability between the forward and reverse shock is able to mix some of this material to larger mass coordinates. However, the bulk of the neutrino-heated ejecta remain below the mass coordinate where the reverse shock formed and are even more compressed and decelerated as the reverse shock propagates to the center of the numerical grid.

In the z9.6 model the forward shock has not passed the He/H interface before a strong reverse shock forms. Although some metal rich ejecta can penetrate through the previously formed dense shell, most of the neutrino heated material remains within the radius of reverse shock formation as well.

The s9.0 model shows a different behavior caused by the different structure of the star. Similar to the RSGs presented in Wongwathanarat et al. (2015) reverse shock formation happens after passage of the He/H interface while the Rayleigh-Taylor instabilities have enough time to grow to considerable size. In particular, we observe the growth of one very large and two to three smaller metal rich clumps which correlate with the positions of largest initial shock deformation. Therefore, more neutrino-heated material can be transported from the core to larger mass coordinates. In this study we identify two distinct morphologies. The ECSNe-like progenitors show only small derivations from sphericity during their whole evolution after bounce.

The e8.8 model in particular does not produce large scale RT fingers that are able to mix neutrino-heated material into the envelope. This is due to the very small initial perturbations set by convective overturn during the first roughly 200 ms after bounce and the monotonic shock propagation in its hydrogen envelope.

The z9.6 model yields a very similar distribution of elements in mass and angular domain. Although mixing seems the be slightly more efficient in the explosion of this progenitor, the overall morphology of the neutrino-heated ejecta remains basically spherical.

The $9\,M_\odot$ model occupies a different regime in our results. A highly variable shock propagation and large initial asymmetries enable efficient mixing of neutrino-heated matter to large mass coordinates and velocities. The mass distribution of elements shows striking similarities with the results presented in e.g. Wongwathanarat et al. (2015). Most striking is the development of a single large plume, not previously observed in long-time simulations of CCSNe. Strong shock deceleration within the hydrogen envelope of the progenitor enables the fast nickel-rich ejecta, which are lifted to high mass coordinates by the RT instability, to catch up with the the forward shock thereby imprinting the asymmetry onto the shock surface. The deformation of the shock persists until it reaches the surface of the star leading to an aspherical shock breakout.

This clearly shows that strong mixing is possible in low-mass iron-core progenitors, answering the third question asked in the beginning. The large nickel clump present in model s9.0 (see Figure 5.16) will be visible in the signature of the γ-ray emission of the supernova (Alp et al., 2019) as zones with a high mass fraction of ^{56}Ni will absorb a significant number of γ's. Strong mixing will also lead to an earlier detection of high energy photons with an increased flux of photons along the viewing angle of ^{56}Ni clumps (Hungerford et al., 2005). Since the clump in the simulation of model s9.0 is clearly correlated with early time asymmetries on the ejecta, such an observation would give important insight into the onset of the explosion and shock propagation within the star.

This also raises the question if the results of Jerkstrand et al. (2018), who used a 1D simulation of model s9.0 to produce theoretical spectra of low-mass progenitors and compare them to observations of candidates of such explosions, may have to be revised with the new 3D data available.

During the long-time simulations we observe only little amount of fallback but a considerable change in the total angular momentum of the respective PNS. Consequently, the initially slow spinning neutron stars are spun up to around 30 ms in the most extreme case (s9.0). This also changes the angle between the angular momentum vector and the direction of the total (neutrino + hydrodynamic) PNS kick. We find a wide spread of angles (in our small set of simulations) and no indication of spin-kick alignment.

The results presented for model s9.0 have interesting implications for the CRAB nebula which originated from SN1054 and was thought to be a candidate for an explosion of an ONeMg core. Recent results by Gessner and Janka (2018) and this work has shown that an explosion of an ECSN is in contradiction with a large kick velocity of $\sim 160\,\mathrm{km/s}$ (Hester, 2008) and a spin period of $\sim 33\,\mathrm{ms}$ (Lyne et al., 2015) which is observed for the CRAB pulsar (PSR B0531+21). The properties of the explosion and of the compact remnant of model s9.0, however, are in line with what we know about the CRAB and its progenitor.

The explosion energy of model s9.0 with around 4×10^{49} erg is in agreement with estimates for SN1054 (Smith, 2013) although our ejecta mass of $\sim 7.4 \, M_\odot$ is higher than the reported 2-5 $M_\odot$ in the literature (Hester, 2008; Smith, 2013). However, mass loss rates during the evolution of the star are still an active and highly discussed topic in stellar evolution modelling (see e.g. Puls et al. 2008). Slightly different prescriptions could lead to larger mass loss and reduce to total explosive ejecta mass. Additionally, Sankrit and Hester (1997) have found that a freely expanding remnant, i.e. the supernova ejecta, around the Crab can have a mass of $> 5 \, M_\odot$ and a kinetic energy of $> 5 \times 10^{50}$ erg without violating the formal limit on Hα emission measure (Hester, 2008).

Additionally, the PNS kick velocity ($v_{NS} \sim 41 \, \mathrm{km/s}$) and final spin period ($\sim 30 \, \mathrm{ms}$) of the compact remnant of model s9.0 are in the order of the observed properties of the CRAB pulsar. Most interestingly, the fast spin period is achieved minutes to hours after the initiation of the explosion and does not rely on the spin-up by SASI or similar mechanisms. Another indication of a, at least, similar evolution of the explosion of the progenitor of SN1054 and model s9.0 is the North-South asymmetry found in the relative emission of He I $\lambda 5876$/Hα in a band running East-West around the nebula and a North-South aligned "stem" seen in [O III] and [N V] (Hester, 2008). This feature may be interpreted as a consequence of an initial dipolar asymmetry of the ejecta, which is clearly found in the simulation of model s9.0. Model z9.6 also shows a short final spin period of the PNS, however, a small kick velocity and almost spherical explosion seem to be in tension with structure of the CRAB nebula.

What remains unsolved is the alignment of the spin and total PNS kick which is observed in the CRAB and other pulsars (Noutsos et al., 2012). While at t_{map} the angle between the total kick and angular momentum θ_{vJ} is fairly small (31°) the angle increases until the end of our long-time simulation to 102°. Also note that we can only give an estimate on the angular momentum transport through our inner boundary and assume that all matter settles onto the PNS. Despite the discrepancy in the spin-kick angle and the weakness in our calculation of the angular momentum transport onto the PNS, the presented results for model s9.0 seem to indicate that SN1054 was not the result of the collapse of an ONeMg core but rather a collapse of an iron-core progenitor with a ZAMS mass of around $9 - 10 \, M_\odot$. With this we answered the last question asked in the beginning and have shown that the PNS properties are not finally set at the time the shock is revived but requires several minutes to hours to reach their ultimate values.

By comparing the results of our long-time simulations of the e8.8 with different parameters of the central engine, we showed that, at least for ECSN, the amount of mixing is only insignificantly influenced by the explosion energy. More important for sufficient mixing is

the compactness of the core, the density profile of the envelope which determines the place and time where a dense shell or reverse shock forms and the initial asymmetries set by neutrino-driven convection. Early formation of a dense shell confines the metal rich ejecta to low-mass coordinates as it is observed in the ECSN-like models. Late formation of the dense shell and the accompanying reverse shock, as it is the case in the s9.0, leaves enough time for the RT instability to grow. Therefore, less neutrino-heated material is affected (decelerated) by passage of the reverse shock. For models z9.6 and s9.0 one can correlate the largest RT plumes at the time of shock breakout with the largest plumes at the time of shock-revival. Due to the early deceleration of the ejecta in the e8.8 and the subsequent strong compression of the matter at the dense shell, we find no such correlation.

Although we could provide a deeper understanding of the possible origin of the CRAB nebula and mixing in low-mass progenitors, more detailed work is necessary in order to determine the observable signatures, e.g. lightcurves and nebular spectra, of such explosive events and to determine the long-time evolution of the compact remnant in more self-consistent simulations.

Appendices

Appendix A

Simplified Neutrino Treatment in Vertex-Prometheus

To continue our expensive full-transport simulations with VERTEX-PROMETHEUS beyond post-bounce times of $\sim 0.5\,\mathrm{s}$, we implemented a new simplified (light-bulb-like) scheme for neutrino emission and absorption. Within this framework, we do not solve the neutrino transport equations (i.e., we switch off the transport module VERTEX) but obtain local source terms from an analytical scaling procedure, which we feed directly into the hydrodynamics module PROMETHEUS. Doing so, we aim at capturing the most crucial neutrino effects in a computationally efficient way, while keeping numerical transients at a minimum and thus ensuring a seamless continuation of our simulations. In the following, we will elaborate on this new approximative neutrino treatment.

A.1   Source terms for energy and lepton number

In our new simplified approach, we apply the following expressions for the net neutrino cooling and heating rates per volume (i.e., energy source terms):

$$Q_{\mathrm{erg}}^{-}(\boldsymbol{r}) = Q_{\mathrm{erg}}^{0}(x) \cdot \left(\frac{\rho(\boldsymbol{r})}{\rho_0(\boldsymbol{r_0})}\right)^2 \left(\frac{T(\boldsymbol{r})}{T_0(\boldsymbol{r_0})}\right)^6 , \tag{A.1}$$

$$Q_{\mathrm{erg}}^{+}(\boldsymbol{r}) = Q_{\mathrm{erg}}^{0}(x) \cdot \left(\frac{\rho(\boldsymbol{r})}{\rho_0(\boldsymbol{r_0})}\right) \left(\frac{R_{\mathrm{gain}}(t_0)}{R_{\mathrm{gain}}(t)}\right)^2 \cdot f_L \, f_E , \tag{A.2}$$

where the quantities with superscript or subscript "0" are the angle-averaged net heating or cooling rate, Q_{erg}^0, the local density, ρ_0, and the local temperature, T_0, at time t_0

when we switch from the transport calculation with VERTEX at $t \leqslant t_0$ to our simplified neutrino treatment at $t > t_0$.[1] To account for the contraction of the gain radius (and thus of the radial heating/cooling profile), we define the variable $x \equiv r_0/R_{\mathrm{gain}}(t_0) = r(t)/R_{\mathrm{gain}}(t)$, which connects the spatial coordinates $\boldsymbol{r} = (r, \theta, \phi)$ and $\boldsymbol{r_0} = (r_0, \theta, \phi)$ via $r_0 = x \cdot R_{\mathrm{gain}}(t_0) = r \cdot R_{\mathrm{gain}}(t_0)/R_{\mathrm{gain}}(t)$. Equation (A.1) is employed in regions where $Q^0_{\mathrm{erg}}(x) < 0$ (i.e., PNS cooling), while Equation (A.2) applies where $Q^0_{\mathrm{erg}}(x) \geqslant 0$ (i.e., gain-layer heating).[2] The scaling of the heating and cooling rates is motivated by the rough scaling of the neutrino absorption rates with the density of a gas of free nucleons and the scaling of (nondegenerate) electron and positron capture rates on nucleons with the temperature (see, e.g., Janka (2001)).

This ansatz fulfills the requirement of a continuous and smooth transition of cooling and heating before and after t_0. f_L and f_E contain the dependence of the neutrino heating on the luminosity (for the energy transferred by neutrino absorption per unit of time) and mean squared neutrino energy (for the rough energy dependence of the absorption cross section). In the spirit of our approach explained above we use the functional scaling prescriptions:

$$f_L = \frac{L_{\nu_e}(t) + L_{\bar{\nu}_e}(t)}{L_{\nu_e}(t_0) + L_{\bar{\nu}_e}(t_0)}\,, \tag{A.3}$$

$$f_E = \left(\frac{E_{\nu_e}(t) + E_{\bar{\nu}_e}(t)}{E_{\nu_e}(t_0) + E_{\bar{\nu}_e}(t_0)}\right)^2 \left(\frac{M_{\mathrm{NS}}(t)}{M_{\mathrm{NS}}(t_0)}\right)^2. \tag{A.4}$$

Following the findings in Müller and Janka (2014), f_E is assumed to scale with the square of the neutron-star mass, M_{NS}. The rough time dependence of the ν_e- and $\bar{\nu}_e$-luminosities and corresponding mean energies is adopted from a 1D PNS-cooling simulation with VERTEX-PROMETHEUS of the z9.6 progenitor, which results in a neutron star of similar mass ($M_{\mathrm{b}} = 1.36\,M_\odot$, $M_{\mathrm{g}} = 1.26\,M_\odot$) compared to the outcome of our 3D simulations of the z9.6 and s9.0 models (see Table 4.2).

---

[1] To smooth the radial source-term profiles $Q^0_{\mathrm{erg}}(x)$, we additionally perform a time average over the last few ms of the full-transport calculation.

[2] We use the heating prescription only outside of the neutron star, i.e. at radii $r > R_{\mathrm{NS}}$ where the angle-averaged densities are below $10^{11}\,\mathrm{g/cm^3}$. For radii $r < R_{\mathrm{NS}}$, we set $Q^+_{\mathrm{erg}}(\boldsymbol{r}) = 0$ if $Q^0_{\mathrm{erg}}(x) > 0$.

In an analogous manner, we apply the following source terms for the rate of lepton-number (Y_e) changes (per volume) by neutrino emission and absorption:

$$Q_{\mathrm{lep}}^{-}(\boldsymbol{r}) = Q_{\mathrm{lep}}^{0}(x) \cdot \left(\frac{\rho(\boldsymbol{r})}{\rho_0(\boldsymbol{r_0})}\right)^2 \left(\frac{T(\boldsymbol{r})}{T_0(\boldsymbol{r_0})}\right)^5 \max\left\{0\,,\frac{Y_e(\boldsymbol{r}) - 0.01}{Y_e^0(\boldsymbol{r_0}) - 0.01}\right\}, \qquad (A.5)$$

$$Q_{\mathrm{lep}}^{+}(\boldsymbol{r}) = Q_{\mathrm{lep}}^{0}(x) \cdot \left(\frac{\rho(\boldsymbol{r})}{\rho_0(\boldsymbol{r_0})}\right) \left(\frac{R_{\mathrm{gain}}(t_0)}{R_{\mathrm{gain}}(t)}\right)^2 \cdot f_L\, f_E \cdot \mathrm{sign}\{v_r(\boldsymbol{r})\}, \qquad (A.6)$$

where Q_{lep}^{0} denotes the angle-averaged rate of lepton-number changes at the time t_0 when we switch from the full-transport calculation to our simplified scheme. Deleptonization, as per Equation (A.5), applies in regions where $Q_{\mathrm{lep}}^{0}(x) < 0$ and $Y_e > 0.01$, whereas for $Q_{\mathrm{lep}}^{0}(x) > 0$ (and outside of the neutron star; cf. footnote 2), the lepton number is raised according to Equation (A.6). As we cannot per se distinguish between down- and outflows in our approach based on angle-averaged source terms, we include the factor $\mathrm{sign}\{v_r\}$ in Equation (A.6), where v_r denotes the radial velocity. This (approximately) accounts for the fact that accretion downflows settling onto the proto-neutron star are getting deleptonized, in contrast to the leptonizing outflows.

Because we do not solve for the neutrino transport and thus cannot treat neutrino heating and cooling self-consistently in our simplified approach, we prescribe the time evolution of the gain radius, which is following the contraction of the neutron star, according to:

$$R_{\mathrm{gain}}(t) = \left[(C_0 - b)\,\frac{\dot{M}(t)}{\dot{M}(t_0)} + b\right] R_{\mathrm{NS}}(t)\,, \qquad (A.7)$$

where $C_0 = R_{\mathrm{gain}}(t_0)/R_{\mathrm{NS}}(t_0)$ and $b = \min\{1.01, C_0\}$ denote the ratio of the gain radius to the neutron-star radius at time t_0 and its assumed asymptotic value at late times, respectively, when the mass accretion rate $\dot{M}(t)$ has declined to an insignificant level. This prescription accounts for an inflated PNS mantel and therefore increased gain radius due to ongoing accretion, and ties in continuously with the evolution of R_{gain} at times before we switch our neutrino treatment. $\dot{M}$ is evaluated at a fixed radius of $100\,\mathrm{km}$ and for downflows ($v_r < 0$) only.

To compensate for a too weak PNS contraction (and thus underestimated heating of the surrounding layers; see Equation (A.2)) in our simulations with approximate neutrino

cooling at late times ($t \gtrsim 1\,\mathrm{s}$), we further scale Equations (A.2) and (A.6) with the factor

$$f_{\mathrm{NS}} = \max\left\{ 1\,, \left(\frac{R_{\mathrm{NS}}(t)}{R_{\mathrm{NS}}^{\mathrm{1D}}(t)}\right)^2 \right\}\,, \qquad (A.8)$$

where $R_{\mathrm{NS}}^{\mathrm{1D}}$ is taken from the same 1D PNS-cooling simulation which is also employed for the time evolution of the neutrino luminosities and mean energies in the definitions of the scaling factors f_L and f_E in Equations (A.3) and (A.4). Hence, the source terms Q_{erg}^+ and Q_{lep}^+ are getting enhanced once the neutron-star radius of the corresponding 1D simulation becomes smaller than the one of our 3D simulation with the simplified neutrino scheme.

A.2 Neutrino pressure correction

Switching off the neutrino transport also leads to a sudden loss of pressure support in the high-density regime. To avoid unphysical artifacts (such as PNS oscillations), we thus replace the neutrino-momentum source term by an adequate correction of the gas pressure. Assuming that neutrinos are in equilibrium with matter at sufficiently high densities, we can employ the following analytic expression:

$$p_\nu^{\mathrm{eq}} = \frac{4\pi(kT)^4}{3(hc)^3}\left[\frac{21\pi^4}{60} + \frac{1}{2}\eta_\nu^2\left(\pi^2 + \frac{1}{2}\eta_\nu^2\right)\right]\,, \qquad (A.9)$$

where T and $\eta_\nu = \mu_\nu/(kT)$ are the local temperature and degeneracy parameter, with μ_ν denoting the neutrino chemical potential.

As the assumption of equilibrium does not hold anymore for regions of lower matter densities (i.e. outside of the neutrinospheres), we describe the neutrino pressure over the entire computational domain according to

$$p_\nu = p_\nu^{\mathrm{eq}} \cdot f_p(\rho) \cdot \min\left\{1, \frac{\rho}{10^{13}\,\mathrm{g/cm^3}}\right\}\,, \qquad (A.10)$$

with the tabulated factor

$$f_p(\rho) = \frac{p_{\mathrm{VERTEX}}(\rho, t_0)}{p_\nu^{\mathrm{eq}}(\rho, t_0)}\,, \qquad (A.11)$$

which we compute from the numerical neutrino pressure, p_{VERTEX}, of the Vertex module and the analytical equilibrium-neutrino pressure according to Equation (A.9). Both the numerator and the denominator are evaluated at the time t_0 (when we switch our neutrino

treatment) and averaged over solid angle. The ratio is then tabulated as a function of the matter density, ρ.

With the same underlying assumptions we include the neutrino energy and pressure contributions to the general relativistic corrections in the effective gravitational potential (case A) of Marek et al. (2006).

References

B. P. Abbott, LIGO Scientific Collaboration, and Virgo Collaboration. GW170817: Observation of Gravitational Waves from a Binary Neutron Star Inspiral. *Phys. Rev. Lett.*, 119(16):161101, Oct 2017. doi: 10.1103/PhysRevLett.119.161101.

Dennis Alp, Josefin Larsson, Keiichi Maeda, Claes Fransson, Annop Wongwathanarat, Michael Gabler, Hans-Thomas Janka, Anders Jerkstrand, Alexander Heger, and Athira Menon. X-Ray and Gamma-Ray Emission from Core-collapse Supernovae: Comparison of Three-dimensional Neutrino-driven Explosions with SN 1987A. *Astrophys. J.*, 882(1): 22, Sep 2019. doi: 10.3847/1538-4357/ab3395.

A. Arcones, H. Th. Janka, and L. Scheck. Nucleosynthesis-relevant conditions in neutrino-driven supernova outflows. I. Spherically symmetric hydrodynamic simulations. *Astronomy & Astrophysics*, 467(3):1227–1248, Jun 2007. doi: 10.1051/0004-6361:20066983.

W. Baade and F. Zwicky. On super-novae. *Proceedings of the National Academy of Science*, 20:254–259, May 1934. doi: 10.1073/pnas.20.5.254. URL https://ui.adsabs.harvard.edu/abs/1934PNAS...20..254B.

R. Bandiera. Convective supernovae. 139:368–374, October 1984. URL https://ui.adsabs.harvard.edu/abs/1984A%26A...139..368B.

H. A. Bethe and J. R. Wilson. Revival of a stalled supernova shock by neutrino heating. *The Astrophysical Journal*, 295:14–23, Aug 1985. doi: 10.1086/163343.

John M. Blondin, Anthony Mezzacappa, and Christine DeMarino. Stability of Standing Accretion Shocks, with an Eye toward Core-Collapse Supernovae. *Astrophys. J.*, 584(2): 971–980, Feb 2003. doi: 10.1086/345812.

Adam Burrows. Colloquium: Perspectives on core-collapse supernova theory. *Rev. Mod. Phys.*, 85(1):245–261, Jan 2013. doi: 10.1103/RevModPhys.85.245.

Adam Burrows and John C. Hayes. Pulsar Recoil and Gravitational Radiation due to Asymetrical Stellar Collapse and Explosion. In *American Astronomical Society Meeting Abstracts*, volume 187, page 17.04, Dec 1995.

Adam Burrows, David Radice, and David Vartanyan. Three-dimensional supernova explosion simulations of 9-, 10-, 11-, 12-, and 13-$M_\odot$ stars. *Mon. Not. R. Astron. Soc.*, 485(3):3153–3168, May 2019. doi: 10.1093/mnras/stz543.

Adam Burrows, David Radice, David Vartanyan, Hiroki Nagakura, M. Aaron Skinner, and Joshua Dolence. The Overarching Framework of Core-Collapse Supernova Explosions as Revealed by 3D Fornax Simulations. *arXiv e-prints*, art. arXiv:1909.04152, Sep 2019.

S. Chandrasekhar. The maximum mass of ideal white dwarfs. *The Astrophysical Journal*, 74:81, Jul 1931. doi: 10.1086/143324.

S. Chandrasekhar. *Hydrodynamic and hydromagnetic stability*. 1961. doi: 10.1063/1.3058072. URL http://adsabs.harvard.edu/abs/1961hhs..book.....C.

S. Chatterjee, W. H. T. Vlemmings, W. F. Brisken, T. J. W. Lazio, J. M. Cordes, W. M. Goss, S. E. Thorsett, E. B. Fomalont, A. G. Lyne, and M. Kramer. Getting Its Kicks: A VLBA Parallax for the Hyperfast Pulsar B1508+55. *Astrophys. J. Lett.*, 630(1):L61–L64, Sep 2005. doi: 10.1086/491701.

R. A. Chevalier and R. I. Klein. On the Rayleigh-Taylor instability in stellar explosions. *The Astrophysical Journal*, 219:994–1007, Feb 1978. doi: 10.1086/155864.

Roger A. Chevalier. Neutron Star Accretion in a Supernova. *Astrophys. J.*, 346:847, Nov 1989. doi: 10.1086/168066.

P. Colella and H. M. Glaz. Efficient solution algorithms for the riemann problem for real gases. *J. Comput. Phys.*, 59:264–289, June 1985. doi: 10.1016/0021-9991(85)90146-9. URL http://adsabs.harvard.edu/abs/1985JCoPh..59..264C.

Stirling A. Colgate and Richard H. White. The hydrodynamic behavior of supernovae explosions. *The Astrophysical Journal*, 143:626, March 1966. doi: 10.1086/148549. URL http://adsabs.harvard.edu/abs/1966ApJ...143..626C.

Jason Dexter and Daniel Kasen. Supernova Light Curves Powered by Fallback Accretion. *Astrophys. J.*, 772(1):30, Jul 2013. doi: 10.1088/0004-637X/772/1/30.

Bernd Einfeldt. On godunov-type methods for gas dynamics. *SIAM J. Numer. Anal.*, 25 (2):294–318, 1988. doi: 10.1137/0725021.

Carola I. Ellinger, Patrick A. Young, Christopher L. Fryer, and Gabriel Rockefeller. A Case Study of Small-scale Structure Formation in Three-dimensional Supernova Simulations. *Astrophys. J.*, 755(2):160, Aug 2012. doi: 10.1088/0004-637X/755/2/160.

Thomas Ertl, Stan E. Woosley, Tuguldur Sukhbold, and H. Thomas Janka. The Explosion of Helium Stars Evolved With Mass Loss. *arXiv e-prints*, art. arXiv:1910.01641, Oct 2019.

T. Fischer, S. C. Whitehouse, A. Mezzacappa, F. K. Thielemann, and M. Liebendörfer. Protoneutron star evolution and the neutrino-driven wind in general relativistic neutrino radiation hydrodynamics simulations. *Astronomy & Astrophysics*, 517:A80, Jul 2010. doi: 10.1051/0004-6361/200913106.

T. Foglizzo, P. Galletti, L. Scheck, and H. Th. Janka. Instability of a stalled accretion shock: evidence for the advective-acoustic cycle. *The Astrophysical Journal*, 654(2): 1006–1021, Jan 2007. doi: 10.1086/509612.

Chris L. Fryer. Neutrinos from Fallback onto Newly Formed Neutron Stars. *Astrophys. J.*, 699(1):409–420, Jul 2009. doi: 10.1088/0004-637X/699/1/409.

Chris L. Fryer and Alexander Heger. Core-Collapse Simulations of Rotating Stars. *Astrophys. J.*, 541(2):1033–1050, Oct 2000. doi: 10.1086/309446.

Alexandra Gessner and Hans-Thomas Janka. Hydrodynamical neutron-star kicks in electron-capture supernovae and implications for the crab supernova. *The Astrophysical Journal*, 865(1):61, Sep 2018. doi: 10.3847/1538-4357/aadbae.

Robert Glas, Oliver Just, H.-Thomas Janka, and Martin Obergaulinger. Three-dimensional Core-collapse Supernova Simulations with Multidimensional Neutrino Transport Compared to the Ray-by-ray-plus Approximation. *The Astrophysical Journal*, 873(1):45, Mar 2019. doi: 10.3847/1538-4357/ab0423.

Brian W. Grefenstette, Chris L. Fryer, Fiona A. Harrison, Steven E. Boggs, Tracey DeLaney, J. Martin Laming, Stephen P. Reynolds, David M. Alexander, Didier Barret, and Finn E. Christensen. The Distribution of Radioactive ^{44}Ti in Cassiopeia A. *Astrophys. J.*, 834 (1):19, Jan 2017. doi: 10.3847/1538-4357/834/1/19.

F. G. Gustavson, W. Liniger, and R. Willoughby. Symbolic generation of an optimal crout algorithm for sparse systems of linear equations. *Journal of the ACM*, 17(1): 87–109, January 1970. ISSN 0004-5411. doi: 10.1145/321556.321565. URL http://doi.acm.org.eaccess.ub.tum.de/10.1145/321556.321565.

Goni Halevi and Philipp Mösta. r-process nucleosynthesis from three-dimensional jet-driven core-collapse supernovae with magnetic misalignments. *Mon. Not. R. Astron. Soc.*, 477 (2):2366–2375, June 2018. doi: 10.1093/mnras/sty797.

N. J. Hammer, H.-Th. Janka, and E. Müller. Three-dimensional Simulations of Mixing Instabilities in Supernova Explosions. *The Astrophysical Journal*, 714(2):1371–1385, May 2010. doi: 10.1088/0004-637X/714/2/1371.

Alexander Heger and S. E. Woosley. Nucleosynthesis and Evolution of Massive Metal-free Stars. *The Astrophysical Journal*, 724(1):341–373, Nov 2010. doi: 10.1088/0004-637X/724/1/341.

Marc Herant and S. E. Woosley. Postexplosion Hydrodynamics of Supernovae in Red Supergiants. *Astrophys. J.*, 425:814, Apr 1994. doi: 10.1086/174026.

Marc Herant, Willy Benz, W. Raphael Hix, Chris L. Fryer, and Stirling A. Colgate. Inside the Supernova: A Powerful Convective Engine. *The Astrophysical Journal*, 435:339, Nov 1994. doi: 10.1086/174817.

J. Hester. The Crab Nebula: An Astrophysical Chimera. *Annual Review of Astronomy and Astrophysics*, 46(1):127–155, 9 2008. ISSN 0066-4146. doi: 10.1146/annurev.astro.45.051806.110608. URL http://www.annualreviews.org/doi/10.1146/annurev.astro.45.051806.110608.

L. Hüdepohl, B. Müller, H. T. Janka, A. Marek, and G. G. Raffelt. Neutrino Signal of Electron-Capture Supernovae from Core Collapse to Cooling. *Phys. Rev. Lett.*, 104(25): 251101, Jun 2010. doi: 10.1103/PhysRevLett.104.251101.

Aimee L. Hungerford, Chris L. Fryer, and Gabriel Rockefeller. Gamma Rays from Single-Lobe Supernova Explosions. *Astrophys. J.*, 635(1):487–501, Dec 2005. doi: 10.1086/497323.

H. T. Janka. 1999.

H.-T. Janka and E. Müller. Neutrino heating, convection, and the mechanism of type-ii supernova explosions. 306:167, February 1996. URL http://adsabs.harvard.edu/abs/1996A%26A...306..167J.

H. Th. Janka. Conditions for shock revival by neutrino heating in core-collapse supernovae. *Astronomy & Astrophysics*, 368:527–560, Mar 2001. doi: 10.1051/0004-6361:20010012.

H.-Th. Janka, B. Müller, F. S. Kitaura, and R. Buras. Dynamics of shock propagation and nucleosynthesis conditions in O-Ne-Mg core supernovae. *Astronomy & Astrophysics*, 485(1):199–208, Jul 2008. doi: 10.1051/0004-6361:20079334.

Hans-Thomas Janka. Explosion Mechanisms of Core-Collapse Supernovae. *Annu. Rev. Nucl. Part. Sci.*, 62(1):407–451, Nov 2012. doi: 10.1146/annurev-nucl-102711-094901.

Hans-Thomas Janka. Neutron Star Kicks by the Gravitational Tug-boat Mechanism in Asymmetric Supernova Explosions: Progenitor and Explosion Dependence. *The Astrophysical Journal*, 837(1):84, Mar 2017. doi: 10.3847/1538-4357/aa618e.

Hans-Thomas Janka, Florian Hanke, Lorenz Hüdepohl, Andreas Marek, Bernhard Müller, and Martin Obergaulinger. Core-collapse supernovae: Reflections and directions. *Progress of Theoretical and Experimental Physics*, 2012(1):01A309, Dec 2012. doi: 10.1093/ptep/pts067.

A Jerkstrand, T Ertl, H-T Janka, E Müller, T Sukhbold, and S E Woosley. Emission line models for the lowest mass core-collapse supernovae - i. case study of a 9 $m_\odot$ one-dimensional neutrino-driven explosion. *Mon. Not. R. Astron. Soc.*, 475(1):277–305, March 2018. doi: 10.1093/mnras/stx2877. URL http://adsabs.harvard.edu/abs/2018MNRAS.475..277J.

Anders Jerkstrand. *Spectra of Supernovae in the Nebular Phase*, page 795. 2017. doi: 10.1007/978-3-319-21846-5_29.

C. C. Joggerst, S. E. Woosley, and Alexander Heger. Mixing in Zero- and Solar-Metallicity Supernovae. *Astrophys. J.*, 693(2):1780–1802, Mar 2009. doi: 10.1088/0004-637X/693/2/1780.

C. C. Joggerst, A. Almgren, and S. E. Woosley. Three-dimensional simulations of rayleigh-taylor mixing in core-collapse supernovae with castro. *The Astrophysical Journal*, 723(1):353–363, November 2010. doi: 10.1088/0004-637X/723/1/353. URL http://adsabs.harvard.edu/abs/2010ApJ...723..353J.

S. Jones, F. K. Röpke, R. Pakmor, I. R. Seitenzahl, S. T. Ohlmann, and P. V. F. Edelmann. Do electron-capture supernovae make neutron stars?. First multidimensional hydrodynamic simulations of the oxygen deflagration. *Astronomy & Astrophysics*, 593:A72, Sep 2016. doi: 10.1051/0004-6361/201628321.

Akira Kageyama and Tetsuya Sato. "Yin-Yang grid": An overset grid in spherical geometry. *Geochem. Geophys. Geosyst.*, 5(9):Q09005, Sep 2004. doi: 10.1029/2004GC000734.

K. Kifonidis, T. Plewa, H.-Th. Janka, and E. Müller. Non-spherical core collapse supernovae. I. Neutrino-driven convection, Rayleigh-Taylor instabilities, and the formation and propagation of metal clumps. *Astronomy & Astrophysics*, 408(2):621–649, Sep 2003. doi: 10.1051/0004-6361:20030863.

K. Kifonidis, T. Plewa, L. Scheck, H.-Th. Janka, and E. Müller. Non-spherical core collapse supernovae. II. The late-time evolution of globally anisotropic neutrino-driven explosions and their implications for SN 1987 A. *Astronomy & Astrophysics*, 453(2):661–678, Jul 2006. doi: 10.1051/0004-6361:20054512.

Rudolf Kippenhahn, Alfred Weigert, and Achim Weiss. *Stellar Structure and Evolution.* Springer Berlin Heidelberg, 2012. doi: 10.1007/978-3-642-30304-3.

O. S. Kirsebom, S. Jones, D. F. Strömberg, G. Martínez-Pinedo, K. Langanke, F. K. Roepke, B. A. Brown, T. Eronen, H. O. U. Fynbo, and M. Hukkanen. Discovery of exceptionally strong nuclear transition sheds new light on the fate of intermediate-mass stars. *arXiv e-prints*, art. arXiv:1905.09407, May 2019.

F. S. Kitaura, H.-Th. Janka, and W. Hillebrandt. Explosions of O-Ne-Mg cores, the Crab supernova, and subluminous type II-P supernovae. *Astronomy & Astrophysics*, 450(1): 345–350, Apr 2006. doi: 10.1051/0004-6361:20054703.

James M. Lattimer and Madappa Prakash. Nuclear matter and its role in supernovae, neutron stars and compact object binary mergers. *Phys. Rep.*, 333:121–146, Aug 2000. doi: 10.1016/S0370-1573(00)00019-3.

James M. Lattimer and Bernard F. Schutz. Constraining the Equation of State with Moment of Inertia Measurements. *The Astrophysical Journal, Volume 629, Issue 2, pp. 979-984.*, 629:979–984, 11 2004. ISSN 0004-637X. doi: 10.1086/431543. URL http://arxiv.org/abs/astro-ph/0411470http://dx.doi.org/10.1086/431543.

James M. Lattimer and F. Douglas Swesty. A generalized equation of state for hot, dense matter. *Nucl. Phys. A*, 535(2):331–376, 12 1991. ISSN 03759474. doi: 10.1016/0375-9474(91)90452-C. URL http://linkinghub.elsevier.com/retrieve/pii/037594749190452C.

Matthias Liebendorfer. A simple parameterization of the consequences of deleptonization for simulations of stellar core collapse. *The Astrophysical Journal*, 633(2):1042–1051, November 2005. doi: 10.1086/466517. URL http://adsabs.harvard.edu/abs/2005ApJ...633.1042L.

Laura A. Lopez, Daniel Castro, Patrick O. Slane, Enrico Ramirez-Ruiz, and Carles Badenes. Identification of a Jet-driven Supernova Remnant in the Small Magellanic Cloud: Possible Evidence for the Enhancement of Bipolar Explosions at Low Metallicity. *Astrophys. J.*, 788(1):5, Jun 2014. doi: 10.1088/0004-637X/788/1/5.

K. Lundmark. Suspected new stars recorded in old chronicles and among recent meridian observations. *Publ. Astron. Soc. Pac.*, 33:225, October 1921. doi: 10.1086/123101. URL https://ui.adsabs.harvard.edu/abs/1921PASP...33..225L.

A. G. Lyne, C. A. Jordan, F. Graham-Smith, C. M. Espinoza, B. W. Stappers, and P. Weltevrede. 45 years of rotation of the Crab pulsar. *Mon. Not. R. Astron. Soc.*, 446 (1):857–864, Jan 2015. doi: 10.1093/mnras/stu2118.

A. Marek, H. Dimmelmeier, H.-Th. Janka, E. Müller, and R. Buras. Exploring the relativistic regime with newtonian hydrodynamics: an improved effective gravitational potential for supernova simulations. *Astronomy & Astrophysics*, 445(1):273–289, Jan 2006. doi: 10.1051/0004-6361:20052840.

Christopher D. Matzner and Christopher F. McKee. The Expulsion of Stellar Envelopes in Core-Collapse Supernovae. *The Astrophysical Journal*, 510(1):379–403, Jan 1999. doi: 10.1086/306571.

Tobias Melson, Hans-Thomas Janka, Robert Bollig, Florian Hanke, Andreas Marek, and Bernhard Müller. Neutrino-driven Explosion of a 20 Solar-mass Star in Three Dimensions Enabled by Strange-quark Contributions to Neutrino-Nucleon Scattering. *The Astrophysical Journal*, 808(2):L42, Aug 2015a. doi: 10.1088/2041-8205/808/2/L42.

Tobias Melson, Hans-Thomas Janka, and Andreas Marek. Neutrino-driven Supernova of a Low-mass Iron-core Progenitor Boosted by Three-dimensional Turbulent Convection. *The Astrophysical Journal*, 801(2):L24, Mar 2015b. doi: 10.1088/2041-8205/801/2/L24.

Tobias Melson, Daniel Kresse, and H. Thomas Janka. Resolution Study for Three-dimensional Supernova Simulations with the Prometheus-Vertex Code. *arXiv e-prints*, art. arXiv:1904.01699, Apr 2019.

Tobias Fabian Melson. *Modeling neutrino-driven core-collapse supernova explosions in three dimensions*. Dissertation, Technische Universität München, München, 2016.

Charles Messier. Catalogue des nébuleuses & des amas d'Étoiles, que l'on découvre parmi les Étoiles fixes sur l'horizon de paris; observées à l'observatoire de la marine, avec differens instruments. *Mémoires de l'Académie Royale des Sciences*, 1774.

B. S. Meyer, G. J. Mathews, W. M. Howard, S. E. Woosley, and R. D. Hoffman. R-Process Nucleosynthesis in the High-Entropy Supernova Bubble. *Astrophys. J.*, 399:656, Nov 1992. doi: 10.1086/171957.

A. Mirizzi, I. Tamborra, H. Th. Janka, N. Saviano, K. Scholberg, R. Bollig, L. Hüdepohl, and S. Chakraborty. Supernova neutrinos: production, oscillations and detection. *Nuovo Cimento Rivista Serie*, 39(1-2):1–112, Jan 2016. doi: 10.1393/ncr/i2016-10120-8.

S. Miyaji, K. Nomoto, K. Yokoi, and D. Sugimoto. Supernova triggered by electron captures. 32:303–329, Jan 1980.

Philipp Mösta, Luke F. Roberts, Goni Halevi, Christian D. Ott, Jonas Lippuner, Roland Haas, and Erik Schnetter. r-process Nucleosynthesis from Three-dimensional Magnetorotational Core-collapse Supernovae. *The Astrophysical Journal*, 864(2):171, Sep 2018. doi: 10.3847/1538-4357/aad6ec.

Bernhard Müller and Hans-Thomas Janka. A New Multi-dimensional General Relativistic Neutrino Hydrodynamics Code for Core-collapse Supernovae. IV. The Neutrino Signal. *Astrophys. J.*, 788(1):82, Jun 2014. doi: 10.1088/0004-637X/788/1/82.

Bernhard Müller, Hans-Thomas Janka, and Andreas Marek. A New Multi-dimensional General Relativistic Neutrino Hydrodynamics Code of Core-collapse Supernovae. III. Gravitational Wave Signals from Supernova Explosion Models. *The Astrophysical Journal*, 766(1):43, Mar 2013. doi: 10.1088/0004-637X/766/1/43.

Bernhard Müller, Tobias Melson, Alexander Heger, and Hans-Thomas Janka. Supernova simulations from a 3d progenitor model – impact of perturbations and evolution of explosion properties. *Mon. Not. R. Astron. Soc.*, 472(1):491–513, Nov 2017. doi: 10.1093/mnras/stx1962.

Bernhard Müller, Daniel W Gay, Alexander Heger, Thomas M Tauris, and Stuart A Sim. Multidimensional simulations of ultrastripped supernovae to shock breakout. *Mon. Not. R. Astron. Soc.*, 479(3):3675–3689, Sep 2018. doi: 10.1093/mnras/sty1683.

Bernhard Müller, Thomas M. Tauris, Alexander Heger, Projjwal Banerjee, Yong-Zhong Qian, Jade Powell, Conrad Chan, Daniel W. Gay, and Norbert Langer. Three-dimensional simulations of neutrino-driven core-collapse supernovae from low-mass single and binary star progenitors. *Mon. Not. R. Astron. Soc.*, 484(3):3307–3324, Apr 2019. doi: 10.1093/mnras/stz216.

E. Müller, B. Fryxell, and D. Arnett. High Resolution Numerical Simulations of Instabilities, Mixing, and Clumping in Supernova 1987A. In *European Southern Observatory Conference and Workshop Proceedings*, volume 37, page 99, Jan 1991.

Ewald Müller and Matthias Steinmetz. Simulating self-gravitating hydrodynamic flows. *Comput. Phys. Commun.*, 89(1-3):45–58, Aug 1995. doi: 10.1016/0010-4655(94)00185-5.

D. K. Nadyozhin. The Properties of NI CO Fe Decay. *The Astrophysical Journal Supplement Series*, 92:527, Jun 1994. doi: 10.1086/192008.

K. Nomoto. Evolution of 8-10 solar mass stars toward electron capture supernovae. i - formation of electron-degenerate o+ne+mg cores. *The Astrophysical Journal*, 277:791–805, Feb 1984. doi: 10.1086/161749.

Ken'ichi Nomoto. Evolution of 8–10 $M_{\odot}$ Stars toward Electron Capture Supernovae. II. Collapse of an O + NE + MG Core. *Astrophys. J.*, 322:206, Nov 1987. doi: 10.1086/165716.

Ken'ichi Nomoto. Private Communication, 2008.

Ken'ichi Nomoto, Nozomu Tominaga, and Sergei I. Blinnikov. Electron-capture supernovae of super-asymptotic giant branch stars and the Crab supernova 1054. In Sunchan Jeong, Nobuaki Imai, Hiroari Miyatake, and Toshitaka Kajino, editors, *American Institute of Physics Conference Series*, volume 1594 of *American Institute of Physics Conference Series*, pages 258–265, May 2014. doi: 10.1063/1.4874079.

A. Noutsos, M. Kramer, P. Carr, and S. Johnston. Pulsar spin-velocity alignment: further results and discussion. *Mon. Not. R. Astron. Soc.*, 423(3):2736–2752, Jul 2012. doi: 10.1111/j.1365-2966.2012.21083.x.

Evan O'Connor and Christian D. Ott. Black Hole Formation in Failing Core-Collapse Supernovae. *The Astrophysical Journal*, 730(2):70, Apr 2011. doi: 10.1088/0004-637X/730/2/70.

S. Orlando, M. Ono, S. Nagataki, M. Miceli, H. Umeda, G. Ferrand, F. Bocchino, O. Petruk, G. Peres, K. Takahashi, and T. Yoshida. Hydrodynamic simulations unravel the progenitor-supernova-remnant connection in SN 1987A. *arXiv e-prints*, art. arXiv:1912.03070, Dec 2019.

T. Plewa and E. Müller. The consistent multi-fluid advection method. 342:179–191, February 1999. URL http://adsabs.harvard.edu/abs/1999A%26A...342..179P.

P. Podsiadlowski, E. Pfahl, and S. Rappaport. *Neutron-Star Birth Kicks*, volume 328 of *Astronomical Society of the Pacific Conference Series*, page 327. 2005.

Joachim Puls, Jorick S. Vink, and Francisco Najarro. Mass loss from hot massive stars. *Astronomy and Astrophysics Review*, 16(3-4):209–325, Dec 2008. doi: 10.1007/s00159-008-0015-8.

Y.-Z. Qian and S. E. Woosley. Nucleosynthesis in Neutrino-driven Winds. I. The Physical Conditions. *The Astrophysical Journal*, 471(1):331, Nov 1996. doi: 10.1086/177973.

David Radice, Adam Burrows, David Vartanyan, M. Aaron Skinner, and Joshua C. Dolence. Electron-capture and Low-mass Iron-core-collapse Supernovae: New Neutrino-radiation-hydrodynamics Simulations. *The Astrophysical Journal*, 850(1):43, Nov 2017. doi: 10.3847/1538-4357/aa92c5.

M. Rampp and H.-T. Janka. Radiation hydrodynamics with neutrinos. variable eddington factor method for core-collapse supernova simulations. *Astronomy & Astrophysics*, 396(1):361–392, December 2002. doi: 10.1051/0004-6361:20021398. URL http://adsabs.harvard.edu/abs/2002A%26A...396..361R.

Rayleigh. Investigation of the character of the equilibrium of an incompressible heavy fluid of variable density. *Proceedings of the London Mathematical Society*, s1-14(1):170–177, November 1882. doi: 10.1112/plms/s1-14.1.170. URL https://doi.org/10.1112/plms/s1-14.1.170.

Edwin E. Salpeter. The Luminosity Function and Stellar Evolution. *The Astrophysical Journal*, 121:161, Jan 1955. doi: 10.1086/145971.

Ravi Sankrit and J. Jeff Hester. The Shock and Extended Remnant around the Crab Nebula. *Astrophys. J.*, 491(2):796–807, Dec 1997. doi: 10.1086/304967.

L. Scheck, K. Kifonidis, H.-Th. Janka, and E. Müller. Multidimensional supernova simulations with approximative neutrino transport. *Astronomy & Astrophysics*, 457(3):963–986, Oct 2006. doi: 10.1051/0004-6361:20064855.

L. Scheck, H.-Th. Janka, T. Foglizzo, and K. Kifonidis. Multidimensional supernova simulations with approximative neutrino transport. *Astronomy & Astrophysics*, 477(3):931–952, Jan 2008. doi: 10.1051/0004-6361:20077701.

L. I. Sedov, M. Friedman, M. Holt, and J. D. Cole. Similarity and Dimensional Methods in Mechanics. *J. Appl. Mech.*, 28(1):159, Jan 1961. doi: 10.1115/1.3640458.

Nathan Smith. The crab nebula and the class of type IIn-p supernovae caused by sub-energetic electron-capture explosions. *Mon. Not. R. Astron. Soc.*, 434(1):102–113, Sep 2013. doi: 10.1093/mnras/stt1004.

Gilbert Strang. On the construction and comparison of difference schemes. *SIAM J. Numer. Anal.*, 5(3):506–517, 1968.

Tuguldur Sukhbold, T. Ertl, S. E. Woosley, Justin M. Brown, and H.-T. Janka. Core-collapse Supernovae from 9 to 120 Solar Masses Based on Neutrino-powered Explosions. *The Astrophysical Journal*, 821(1):38, Apr 2016. doi: 10.3847/0004-637X/821/1/38.

Alexander Summa, Florian Hanke, Hans-Thomas Janka, Tobias Melson, Andreas Marek, and Bernhard Müller. Progenitor-dependent Explosion Dynamics in Self-consistent, Axisymmetric Simulations of Neutrino-driven Core-collapse Supernovae. *The Astrophysical Journal*, 825(1):6, Jul 2016. doi: 10.3847/0004-637X/825/1/6.

Douglas A. Swartz, Peter G. Sutherland, and Robert P. Harkness. Gamma-Ray Transfer and Energy Deposition in Supernovae. *The Astrophysical Journal*, 446:766, Jun 1995. doi: 10.1086/175834.

Tomoya Takiwaki, Kei Kotake, and Yudai Suwa. Three-dimensional hydrodynamic core-collapse supernova simulations for an 11.2 m star with spectral neutrino transport. *The Astrophysical Journal*, 749(2):98, Apr 2012. doi: 10.1088/0004-637X/749/2/98.

Irene Tamborra, Florian Hanke, Hans-Thomas Janka, Bernhard Müller, Georg G. Raffelt, and Andreas Marek. Self-sustained Asymmetry of Lepton-number Emission: A New Phenomenon during the Supernova Shock-accretion Phase in Three Dimensions. *The Astrophysical Journal*, 792(2):96, Sep 2014. doi: 10.1088/0004-637X/792/2/96.

Irene Tamborra, Georg Raffelt, Florian Hanke, Hans-Thomas Janka, and Bernhard Müller. Neutrino emission characteristics and detection opportunities based on three-dimensional supernova simulations. *Phys. Rev. D*, 90(4):045032, Aug 2014. doi: 10.1103/PhysRevD.90.045032.

F. X. Timmes and Dave Arnett. The accuracy, consistency, and speed of five equations of state for stellar hydrodynamics. *The Astrophysical Journal Supplement Series*, 125(1):277–294, Nov 1999. doi: 10.1086/313271.

D. L. Tubbs. Conservative scattering, electron scattering, and neutrino thermalization. *The Astrophysical Journal*, 231:846–853, August 1979. doi: 10.1086/157249. URL http://adsabs.harvard.edu/abs/1979ApJ...231..846T.

Marcella Ugliano, Hans-Thomas Janka, Andreas Marek, and Almudena Arcones. Progenitor-explosion Connection and Remnant Birth Masses for Neutrino-driven Supernovae of Iron-core Progenitors. *The Astrophysical Journal*, 757(1):69, Sep 2012. doi: 10.1088/0004-637X/757/1/69.

V. P. Utrobin, A. Wongwathanarat, H. Th. Janka, and E. Müller. Supernova 1987A: neutrino-driven explosions in three dimensions and light curves. *Astronomy & Astrophysics*, 581:A40, Sep 2015. doi: 10.1051/0004-6361/201425513.

V. P. Utrobin, A. Wongwathanarat, H. Th. Janka, and E. Müller. Light-curve Analysis of Ordinary Type IIP Supernovae Based on Neutrino-driven Explosion Simulations in Three Dimensions. *Astrophys. J.*, 846(1):37, Sep 2017. doi: 10.3847/1538-4357/aa8594.

V. P. Utrobin, A. Wongwathanarat, H.-Th. Janka, E. Müller, T. Ertl, and S. E. Woosley. Three-dimensional mixing and light curves: constraints on the progenitor of supernova 1987a. *Astronomy & Astrophysics*, 624:A116, Apr 2019. doi: 10.1051/0004-6361/201834976.

David Vartanyan, Adam Burrows, David Radice, M Aaron Skinner, and Joshua Dolence. Revival of the fittest: exploding core-collapse supernovae from 12 to 25 m$\odot$. *Mon. Not. R. Astron. Soc.*, 477(3):3091–3108, Jul 2018. doi: 10.1093/mnras/sty809.

Janina Christine von Groote. *General Relativistic Multi Dimensional Simulations of Electron Capture Supernovae*. Dissertation, Technische Universität München, München, 2014.

Shinya Wanajo, Bernhard Müller, Hans-Thomas Janka, and Alexander Heger. Nucleosynthesis in the innermost ejecta of neutrino-driven supernova explosions in two dimensions. *The Astrophysical Journal*, 852(1):40, Jan 2018. doi: 10.3847/1538-4357/aa9d97.

Tsing-Wai Wong, Christopher L. Fryer, Carola I. Ellinger, Gabriel Rockefeller, and Vassiliki Kalogera. The Fallback Mechanisms in Core-Collapse Supernovae. *arXiv e-prints*, art. arXiv:1401.3032, Jan 2014.

A. Wongwathanarat, N. J. Hammer, and E. Müller. An axis-free overset grid in spherical polar coordinates for simulating 3d self-gravitating flows. *Astron. Astrophys.*, 514:A48, May 2010. doi: 10.1051/0004-6361/200913435.

A. Wongwathanarat, H. Th. Janka, and E. Müller. Three-dimensional neutrino-driven supernovae: Neutron star kicks, spins, and asymmetric ejection of nucleosynthesis products. *Astronomy & Astrophysics*, 552:A126, Apr 2013. doi: 10.1051/0004-6361/201220636.

A. Wongwathanarat, E. Müller, and H.-Th. Janka. Three-dimensional simulations of core-collapse supernovae: from shock revival to shock breakout. *Astronomy & Astrophysics*, 577:A48, May 2015. doi: 10.1051/0004-6361/201425025.

Annop Wongwathanarat, Hans-Thomas Janka, Ewald Müller, Else Pllumbi, and Shinya Wanajo. Production and distribution of 44ti and 56ni in a three-dimensional supernova model resembling cassiopeia a. *The Astrophysical Journal*, 842(1):13, Jun 2017. doi: 10.3847/1538-4357/aa72de.

S. E. Woosley. The great supernova of 1987. *Annals of the New York Academy of Sciences*, 571:397–413, Dec 1989. doi: 10.1111/j.1749-6632.1989.tb50526.x.

S. E. Woosley and Alexander Heger. The Remarkable Deaths of 9-11 Solar Mass Stars. *The Astrophysical Journal*, 810(1):34, Sep 2015. doi: 10.1088/0004-637X/810/1/34.

Weiqun Zhang, S. E. Woosley, and A. Heger. Fallback and Black Hole Production in Massive Stars. *Astrophys. J.*, 679(1):639–654, May 2008. doi: 10.1086/526404.